Atmospheric Gravity Waves on Giant Planets

Christopher Lloyd Watkins

Thesis submitted for the degree of
Doctor of Philosophy (PhD)
of the University of London

Queen Mary, University of London

July 2012

Abstract

Internal gravity waves are a common feature of stratified fluids. They facilitate transport of momentum and energy – thus influencing the evolution of the fluid. There is a large body of research addressing the behaviour of gravity waves in the terrestrial atmosphere. This thesis builds and extends the research to giant planets – in particular to close-in extrasolar giant planets and the solar system giant planet, Jupiter. Because the atmospheres of close-in giant planets are expected to be strongly stratified, knowledge of the behaviour of gravity waves in such atmospheres is especially important.

Close-in giant planets are thought to have their rotations and orbital period 1:1 synchronised, i.e., they are "tidally locked". Such planets do not exist in the Solar System. However, many are known from observations of extrasolar systems. Their synchronisation means that they have a permanent day-side and night-side leading to interesting atmospheric dynamics. Modelling these circulations with global circulation models (GCMs) and comparing these models with observations is an active research area. However, many GCMs filter some or all gravity waves removing their effects. This thesis addresses this by explicitly looking at the effects gravity waves can have on the circulation. It is shown that gravity waves provide a mechanism for accelerating, decelerating, and heating the flow. Further, horizontally propagating gravity waves are shown to provide a possible means for coupling the day- and night-sides of tidally locked planets.

As well as affecting the dynamics of the atmosphere, gravity wave behaviour is affected by the dynamics of the atmosphere. Therefore, gravity waves can be used to explore atmospheric properties. In this thesis gravity waves observed in Jupiter's atmosphere, by the Galileo probe, are used to identify features of Jupiter's atmosphere such as the altitude of the turbopause and the vertical profile of zonal winds at the probe entry site.

Declaration

This thesis describes work done at the Astronomy Unit of the School of Physics and Astronomy, at Queen Mary University of London, under the supervision of Dr. James Y-K. Cho.

Parts of Chapters 2 and 3 contain material that has been published in a peer reviewed journal in the following article:

- Watkins, C., and J. Y-K. Cho (2010), Gravity Waves on Hot Extrasolar Planets. I. Propagation and Interaction with the Background, Ap. J., 714, 904.

Part of Chapter 4 contains material that has been submitted for publication in a peer reviewed journal in the following article:

- Watkins, C., and J. Y-K. Cho (2012), The Vertical Structure of Jupiters Equatorial Zonal Wind, derived using Mesoscale Gravity Waves.

Parts of Chapters 3 and 4 contain material that is currently being prepared for submission for publication in peer reviewed journals in the following articles:

- Watkins, C., and J. Y-K. Cho (2012), Gravity Waves on Hot Extrasolar Planets. II. Dissipation in the Upper Atmosphere.
- Polichtchouk, I., J. Y-K. Cho, C. Watkins, H. Th. Thrastarson, O. M. Umurhan and M. de la Torre-Juarez (2012), Intercomparison of General Circulation Models for Hot Extrasolar Planets

I hereby declare that the work presented in this thesis is my own, unless otherwise stated.

Christopher Watkins

20 July 2012

Acknowledgements

My thanks goes to my supervisor, James Cho, for all his support and encouragement during my period as his student. I have benefited enormously from his knowledge, experience and guidance.

I also owe a debt of gratitude to the members of the Planetary Atmosphere Dynamics Group (otherwise known as the "PAD Group") for providing many hours of interesting and stimulating discussions: Inna Polichtchouk, Heidar Thrastarson, Orkan (Matt) Urmurhan, Tommi Koskinen, Ali Gülsen, Zoe Gumm and James Cho.

I thank members of the academic staff in the Astronomy Unit (AU) for all their advice and feedback over the years – especially Craig Agnor, Sergei Vorontsov, Reza Tavakol and Richard Nelson.

I also am grateful for the camaraderie of my fellow past and present students in the AU.

I acknowledge the support provided by the Science and Technology Funding Council.

Finally I thank my wife, Amanda, for supporting me in so many ways.

Contents

List of Figures

List of Tables

Chapter 1

Introduction

Until the last decade of the twentieth century the only known giant planets were those such as Jupiter in the Solar System. However, in 1995 the discovery of a giant planet orbiting the star 51 Pegasi confirmed the existence of giant planets beyond the Solar System (Mayor and Queloz, 1995). A few years earlier planets had been discovered orbiting a pulsar (Wolszczan and Frail, 1992). However, these planets were not giant planets, having masses of only about four times that of the Earth. Since these early discoveries, observations using improved techniques and dedicated telescopes and spacecraft, have led to a large increase in the number of planets known to exist beyond the Solar System. As of December 2012, the number of confirmed planets stands at over 850, of which more than 710 have masses greater than Uranus; hence, the majority of planets known thus far may be thought of as giant planets. The Kepler space mission has more than 2,000 additional "candidate" planets. It is clear that the number of known extrasolar planets will continue to grow for some time to come.

Even with this explosive growth in the number of known extrasolar planets, there are still goals to be achieved in the discovery of new planets. This includes the detection of an Earth-like planet in the so-called "Goldilocks-zone"; such a planet may be capable of supporting life. Research effort is now also being focussed on increasing our understanding of those bodies already known. For example, the proposed Exoplanet Characterisation Observatory (EChO) space mission will allow investigation of the atmospheres of extrasolar planets. Within the known extrasolar planets there are bodies that are very

different from those in the Solar System, such as the "hot-Jupiters". These are Jupiter-sized planets that orbit very close (within ~ 0.05 AU) to their respective central stars. Understanding the characteristics and formation of these new type of planets is currently an active research area. For example, there is a fast-growing literature and increasing number of meetings dedicated to the atmospheric dynamics of these planets.

1.1 Close-In Extrasolar Planets

The discovery of 51 Pegasi b introduced the new science of hot-Jupiter astrophysics. These planets, in orbits with very small semi-major axes (in comparison to the Solar System), proved to be a challenge to planetary formation models. Currently, they are thought to form at a distance from the central star, the "snow-line", beyond which volatiles such as water and methane condense. Through interactions with the proto-planetary disc, the formed planets then migrate inwards towards the star, leading to the small orbits at which we observe them today. The details of this process are still the focus of intensive research.

The majority of close-in giant planets also have orbits with low eccentricity. It is believed that giant planets in such orbits interact tidally with their stars, causing their orbits to circularize (i.e., eccentricity goes to zero) and synchronize their spin and orbit periods (Goldreich and Soter, 1966). Thus, such planets have permanent day and night sides.

1.1.1 Observations

The main observational technique for extrasolar planets is the radial velocity method; the Extrasolar Planets Encyclopaedia (http://exoplanet.eu/) lists 61% of extrasolar planets as discovered using it. Indeed, it was with this method that 51 Pegasi b was discovered. The method takes advantage of the fact that, in a planet-star system, both bodies orbit the barycentre of the system. Thus, the star periodically moves toward and away from an observer. This motion can be detected as a time-dependent doppler-shift in the spectrum of the star and the presence of the planet deduced.

Beyond the presence of the planet, the radial velocity technique provides the period of the planet – and, from the mass of the star and Kepler's third law, the mass of the planet. As the inclination i of the perpendicular to the orbital plane to the line of sight is unknown, the deduced mass is uncertain by a factor of $\sin i$. If the planet also passes across the line of sight of the observer (i.e., transits the star), the variation of the redshift during the transit gives information about the relative alignment of the planetary orbit axis and the stellar spin axis: this is the Rossiter-McLaughlin effect (McLaughlin, 1924; Rossiter, 1924).

The light curves of stars with transiting planets exhibit a regular, slight dimming of the star, as the planet passes between the star on the observer. The observer is in the plane of the planet's orbit giving $\sin i \approx 1$. Therefore, when combined with radial velocity observations, the planet's mass can be obtained. The shape of the curve can also reveal the size of the planet, which combined with the mass gives the density of the planet – hence some insight into the composition of the planet. Variations in the timing and duration of the transit can indicate the presence of other bodies, such as moons and additional planets.

From their bulk density, the atmospheres of extrasolar giant planets (EGPs) are thought to consist primarily of hydrogen with helium as the next most abundant constituent, like Jupiter. Spectra obtained during a transit, compared to spectra at other times, allow the composition of the atmosphere to be deduced. This is accomplished by assuming that differences in the spectra are due to the atmosphere. Indeed, it was spectroscopy that was used to first show that atmospheres on extrasolar planets existed (Charbonneau et al., 2002). The detailed composition of such atmospheres has become clearer with the discovery of many species – such as atomic hydrogen (Vidal-Madjar et al., 2003), water (Tinetti et al., 2007) and methane (Swain et al., 2010) – through spectroscopy. As well as composition spectroscopy can give insight into other properties, such as temperature. There has even been a claim to observe a doppler shift in the transmission spectrum of HD 209458 b, which has been taken to be evidence of winds of approximately 2 km s^{-1} (Snellen et al., 2010).

The light curve of stars with transiting (and near transiting) planets contains information on the variation of light radiated by the planet toward the observer as it orbits the star. This shows the temperature distribution on the

"surface" of such planets. It may be arguable that on a tidally locked planet that the hottest part would be the sub-stellar point, the point where the star is permanently directly overhead. However, light-curves have shown that the "hot-spot" can be displaced by a significant amount (Knutson et al., 2007) from the sub-stellar point on the planet. The largest displacement so far deduced from observation is 80°; this places the "hot-spot" nearly at the terminator, the boundary between the day-side and night-side (Crossfield et al., 2010).

As well as transiting the star such exoplanets are eclipsed by (i.e., pass behind) the star. This gives access to the emission spectrum of the planet. In general, the shape of spectra depends on the temperature of the atmosphere. Hence, the dependence provides a means to diagnose a temperature profile, via mathematical inversion. Some studies using this technique have identified "temperature inversions" in extrasolar planet atmospheres – that is, the existence of a stratosphere (e.g., Knutson et al., 2008, 2009).

The transit method is well suited for large-scale surveys designed to detect large numbers of extrasolar planets. The large number allows investigation of the statistical properties of the planets. One such survey is the Kepler mission, a space-based telescope launched in 2009. The space telescope acquires photometry of over 145,000 stars. The length of the mission allows planets with longer orbital periods to be detected. As of December 2012 the mission has announced 105 planets, with more than 2320 candidate planets.

Microlensing events, in which the brightness of background stars are temporarily brightened by the gravitational effect of foreground planets, have also been used to detect extrasolar planets (e.g. Bond et al., 2004). Additionally, direct images of some exoplanets have now been obtained – for example, the HR 8799 planetary system (Marois et al., 2008). For a more complete review of the available observational techniques, including and assessment of prospects for improvement, see, for example, part II of Seager (2010).

1.1.2 Atmospheric Dynamics Modelling

There have been a number of studies modelling the atmospheric dynamics of hot-Jupiters using a range of mathematical models (equations and numerical algorithms) and physical assumptions. The models include those based on

one-layer equivalent barotropic equations, using the pseudospectral method (e.g., Cho et al., 2003); hydrostatic primitive equations, using the finite volume method (e.g., Showman et al., 2008, 2009) and pseudospectral method (e.g., Heng and Vogt, 2011; Rauscher and Menou, 2010; Thrastarson and Cho, 2010, 2011); and, the full Navier-Stokes equations, using the finite difference method (e.g., Dobbs-Dixon, Cumming, and Lin, 2010; Koskinen et al., 2007). These studies also take a varied approach to representing the forcing, including relaxation schemes and one dimensional radiative transfer.

In general, the studies predict that general circulations of hot-Jupiters contain a small number of jets. Many of the studies obtain a broad eastward equatorial jet which, in some cases, is of a considerable speed (i.e., supersonic), flanked by weaker westward jets (e.g., Showman et al., 2008). Moreover, hot-spots which are displaced east from the substellar point and "stratospheres" have also been produced by simulations (e.g., Showman et al., 2009). However, much work remains to be carried out to investigate the robustness of these findings: features such as zonally-symmetric eastward equatorial jets and multiple hot-spots, whose locations change with time, have also been produced in simulations (e.g., Thrastarson and Cho, 2010).

Studies have been performed to understand how "dynamical cores" of GCMs that are designed to model Earth's atmospheric circulation behave in conditions like extrasolar giant planet (EGP) atmospheres. The effects of the initial conditions and the dissipation used have been investigated (Thrastarson and Cho, 2010, 2011), and rigorous tests for the inter-comparison of "extrasolar planet GCMs" have been performed (Heng, Menou, and Phillipps, 2011; Polichtchouk et al., 2012). To augment the GCMs and improve the solutions that they produce, it is also important that parametrisation of key physical processes that impact the circulation (e.g., modification of radiative forcing by clouds and of drag by atmospheric gravity waves and tides) are either plausibly adapted from existing treatments or created anew.

1.2 Jupiter

Jupiter was known to the ancients as it is an object that can be seen in the night-sky with the naked eye. However, it was not until the invention of the

telescope that exploration of the Jovian system truly began. This started when Galileo described Jupiter's four major moons in 1610 in his book, *Sidereus Nuncius*. Twenty years later, the banded structure of Jupiter was reported by Niccol Zucchi (Rogers, 1995). Over the following four centuries the atmosphere of Jupiter has been of constant interest to both professional and amateur astronomers.

The drive to understand transience in Jupiter's atmosphere (e.g., the recent disappearance and subsequent reappearance of the South Equatorial Belt), alongside long-lived features (e.g., the Great Red Spot) has led to a substantial literature dedicated to Jupiter's atmosphere. Myriad images of the planet have been obtained during fly-bys by space missions. The Galileo mission, which orbited Jupiter for nearly eight years, was dedicated to the study of the planet and included an atmospheric probe. Currently, the Juno spacecraft is travelling to Jupiter and is due to enter orbit in 2016. This mission, among other objectives, will investigate the convective interior of Jupiter and its links to the planet's atmospheric circulation.

1.2.1 Jupiter's Atmosphere

Jupiter's atmosphere is primarily composed of hydrogen ($\sim 90\%$ by volume), with helium as the other major component ($\sim 10\%$ by volume). There are small amounts of other species, such as methane and ammonia. The latter forms the clouds that define the "surface" of the planet. Below this a layer of water clouds is thought to exist.

Jupiter's atmosphere has a troposphere below a roughly isothermal stratosphere. There is a thermosphere above the stratosphere. Unlike the Earth, Jupiter does not have a mesosphere. The ammonia clouds form around the level of the tropopause, where the troposphere and stratosphere meet. Within the clouds a number of zonal bands (known as belts and zones) can be clearly seen. The bands are correlated with prograde and retrograde jets. While the horizontal extent of these jets can be easily seen from their effect on the clouds, the vertical range they cover is unknown. The jets may be shallow in nature; it has been shown that jets can emerge from turbulent flow in a shallow rotating sphere (e.g., Cho and Polvani, 1996a,b). Such models, while successful in many ways, did not produce strong prograde equatorial jets, as is observed

on Jupiter. More recent work has shown models that include uniform thermal dissipation remedies this, leading to prograde equatorial jets (Scott and Polvani, 2008). Others argue that cloud features are surface manifestations of rotating cylinders, formed deep in Jupiter in accordance with the Taylor-Proudman theorem (Busse, 1976; Heimpel, Aurnou, and Wicht, 2005). These models do produce strong prograde equatorial jets, but they also produce jets with significant peak velocities in the high latitudes – in contradiction to the observed meridional structure of the jets.

1.3 Thesis Outline

This thesis describes the behaviour of atmospheric gravity waves on giant planets, both extrasolar and Solar. Chapter 2 reviews the theory of linear gravity waves and extends their governing equation to the pseudo-incompressible case (Durran, 1989). The technique used to solve the equation is described, along with parametrisations used to model non-linear processes such as wave-breaking. Chapter 3 investigates how gravity waves behave on a typical EGP. Both vertical and horizontal propagation are considered, along with saturation and encounters with critical layers. Propagation of gravity waves in a dissipative atmosphere is also considered. The effects such waves have in regions where viscosity and thermal diffusivity dominate are described. The implications of these finding for general circulation models (GCMs) are discussed. Chapter 4 considers gravity waves on and in Jupiter. Using a mathematical inversion of the governing equation of gravity waves, the atmospheric properties that can be deduced from observations of mesoscale gravity waves in the region from the upper troposphere to the lower thermosphere are investigated. The role gravitational atmospheric tides may play in Jupiter's circulation is also briefly considered. Finally, in Chapter 5, a summary of the thesis is given and avenues of future work stemming from the thesis work are outlined.

Chapter 2

Theory of Atmospheric Gravity Waves

A stably stratified atmosphere can support internal gravity or buoyancy waves, also known as g-modes (e.g., Thompson, 2006). They are oscillations that arise from the buoyancy of the fluid. They are readily excited by many processes, such as flow over physical and thermal topography, convective overshoot, instabilities and flow adjustment processes (see, e.g., Fritts and Alexander, 2003, for a review of generation mechanisms). They propagate through atmospheres, both horizontally and vertically. These waves are much studied in the terrestrial atmosphere and oceans (e.g., Gill, 1982; Gossard and Hooke, 1975; Lindzen, 1990; Nappo, 2002). They have been observed in the atmospheres of solar system bodies including Jupiter (e.g. Flasar and Gierasch, 1986; Reuter et al., 2007; Young et al., 1997).

Gravity waves play an important role in the dynamics of atmospheres. They can propagate vast distances through many layers of the atmosphere. Thus, they provide a mechanism via which surface phenomena (such as topography) may have significant effects far up in the atmosphere. Turbulence generated by breaking gravity waves helps to keep the lower atmosphere well mixed. Above this layer, gravity waves play a significant role in the dynamics of the middle atmosphere (Andrews, Holton, and Leovy, 1987).

In this chapter the theory required to understand the behaviour of linear gravity waves is derived. Although the waves are described in a linear treatment,

parameterisations for handling the key non-linear processes of interactions with critical layers (regions where the wave is not supported) and wave breaking are given. This allows the role that the waves play in heating and accelerating the atmosphere to be practically studied.

2.1 Basic Concepts

2.1.1 Potential Temperature

Stratified atmospheres have a positive vertical entropy gradient. In this thesis this is represented by a positive gradient in the related concept of potential temperature θ. This is defined as the temperature a parcel of air would attain if it were moved adiabatically to a reference pressure p_{ref} (usually taken to be 1 bar). For an adiabatic process, according to the first law of thermodynamics,

$$\mathrm{d}Q = c_p \mathrm{d}T - \alpha \mathrm{d}p = 0\,. \tag{2.1}$$

Here $\mathrm{d}Q$ is the heating, which is zero for an adiabatic process; $\mathrm{d}T$ is the change in temperature; $\mathrm{d}p$ is the change in pressure; α is the specific volume, the reciprocal of the density ρ; and, c_p is the specific heat at constant pressure, taken to be a constant. Assuming that the atmosphere can be well modelled as an ideal gas, the equation of state is,

$$p = \rho R T\,, \tag{2.2}$$

where R is the gas constant. Substituting for α and integrating between p_{ref} and p gives the potential temperature as

$$\theta = T \left(\frac{p_{ref}}{p} \right)^{\kappa}\,, \tag{2.3}$$

where $\kappa = R/c_p$.

2.1.2 Hydrostatic Equilibrium

Hydrostatic equilibrium is the assumption that the weight of the atmosphere is balanced by the pressure force pushing the atmosphere outward to space:

$$\frac{\partial p}{\partial z} = -\rho g \,, \tag{2.4}$$

where g is the acceleration due to gravity. This is an approximation, but an extremely good one. For example, if the balance were not met, a gravity dominated atmosphere would collapse or, if pressure dominated, the atmosphere would escape to space. The latter does happen to some extent, but it is nowhere large enough to invalidate the use of the approximation in our context. Indeed, in most cases it can be assumed that the atmosphere as a whole, the background state, is hydrostatic with impunity.

2.1.3 Adiabatic Lapse Rate

Using Equation (2.4), to substitute for $\mathrm{d}p$ in Equation (2.1), gives the adiabatic lapse rate,

$$\Gamma = -\frac{\mathrm{d}T}{\mathrm{d}z} = \frac{g}{c_p} \,. \tag{2.5}$$

This is the rate at which an atmospheric parcel cools as it moves adiabatically upward through the atmosphere.

2.1.4 The *Brunt–Väisälä* Frequency

The behaviour of an air parcel with mass m_p which is adiabatically displaced vertically by a small displacement δz can now be investigated. Using Newton's second law and Equation (2.2), the acceleration of the parcel is given by,

$$\frac{\mathrm{d}^2\left(\delta z\right)}{\mathrm{d}t^2} = -g\,\frac{m_p - m_a}{m_p} = -g\,\frac{T_a - T_p}{T_a} \,, \tag{2.6}$$

where m_a is the mass of the atmosphere displaced by the parcel and T_a and T_p are the atmospheric and parcel temperatures, respectively. Expanding T_a and T_p to first order about an equilibrium temperature T_0, and noting that $\mathrm{d}T_p/\mathrm{d}z$

is the adiabatic lapse rate, gives

$$\frac{\mathrm{d}^2(\delta z)}{\mathrm{d}t^2} = -\frac{g}{T_a}\left(\frac{\partial T_a}{\partial z} + \frac{g}{c_p}\right)\delta z\,. \tag{2.7}$$

Taking the logarithmic derivative of Equation (2.3) with respect to z and using Equations (2.4) and (2.2) to eliminate the pressure and density gives

$$\frac{1}{\theta}\frac{\partial \theta}{\partial z} = \frac{1}{T_a}\left(\frac{\partial T_a}{\partial z} + \frac{g}{c_p}\right)\,. \tag{2.8}$$

Substituting this into Equation (2.7) gives

$$\frac{\mathrm{d}^2(\delta z)}{\mathrm{d}t^2} = -\frac{g}{\theta}\frac{\partial \theta}{\partial z}\delta z = -N^2\delta z\,. \tag{2.9}$$

This describes a simple harmonic oscillator with frequency,

$$N = \sqrt{\frac{g}{\theta}\frac{\partial \theta}{\partial z}}\,, \tag{2.10}$$

the *Brunt–Väisälä* frequency. The solution to Equation (2.7) is

$$\delta z(t) = Ae^{iNt} + Be^{-iNt}\,. \tag{2.11}$$

From this solution we can see that when N is imaginary (i.e., $\partial\theta/\partial z < 0$), the displacement grows exponentially. This is convective instability. On the other hand, if N is real (that is, $\partial\theta/\partial z > 0$), the atmosphere is stably stratified and the parcel oscillates about its equilibrium position with the *Brunt–Väisälä* frequency.

2.1.5 Scale Heights

Using the ideal gas equation of state, Equation (2.2), to eliminate density from Equation (2.4) and integrating gives the following expression for the pressure:

$$p(z) = p_s \exp\left\{-\int_{z_s}^{z} \frac{g}{RT(\zeta)}\,\mathrm{d}\zeta\right\}\,, \tag{2.12}$$

where p_s is the pressure at z_s. For an isothermal atmosphere (i.e., when $T(\zeta)$ is constant), and assuming g and R to be constant, taking $z_s = 0$ gives,

$$p(z) = p_s \exp\left\{-\frac{z}{H_p}\right\} . \tag{2.13}$$

Here H_p is the pressure scale height, the distance over which the pressure falls by a factor of e, defined by

$$\frac{1}{H_p} = \frac{g}{RT} = -\frac{1}{p}\frac{\partial p}{\partial z} = \frac{\gamma g}{c_s^2} , \tag{2.14}$$

where $\gamma = c_p/c_v$, c_v is the specific heat at constant volume and $c_s = \sqrt{\gamma RT}$ is the speed of sound (Holton, 2004). Analogous e-folding distances can be defined for the density and potential temperature, H_θ and H_ρ, respectively:

$$\frac{1}{H_\rho} = -\frac{1}{\rho}\frac{\partial \rho}{\partial z} \tag{2.15}$$

$$\frac{1}{H_\theta} = \frac{1}{\theta}\frac{\partial \theta}{\partial z} . \tag{2.16}$$

The three scale heights are related by

$$\frac{1}{H_\theta} = \frac{1}{H_\rho} - \frac{1}{\gamma H_p} . \tag{2.17}$$

An incompressible flow is equivalent to one where the sound speeds becomes very large, tending to infinity. In such a flow Equation (2.14) shows that $1/H_p$ becomes small, and then from Equation (2.17) it can be seen that the density and potential temperature scale heights can be taken as equivalent.

2.2 The Fluid Equations

2.2.1 Rotation

The dynamics of linear gravity waves is described by the Taylor-Goldstein Equation (T.G.E.). This equation is derived (see Section 2.3.1) from the full, three-dimensional hydrodynamics equations (Batchelor, 1967). The rotation of the planet is neglected. This is a valid approximation when the accelerations

due to the Coriolis forces are dominated by the advection of momentum:

$$u\frac{\partial u}{\partial x} > fv\,, \tag{2.18}$$

where u is the zonal flow and v the meridional flow; $f = 2\Omega\sin\varphi$ is the Coriolis parameter, where Ω is the planet's rate of rotation; and, φ the latitude. Taking $\mathcal{U}$ as a typical flow speed for u, ∂u and v and taking Ω as a representative value for f, as long as the scale of the motion is less than $\mathcal{L}$ such that

$$\mathcal{L} < \frac{\mathcal{U}}{\Omega}\,, \tag{2.19}$$

we can neglect rotation. However, for the larger scale motions associated with the tides, discussed in Section 5.1.1, rotation cannot be neglected.

2.2.2 The Basic Equations

Only motions in an inviscid fluid in two dimensions, the horizontal and the vertical, are considered in this derivation of the TGE. Given this set-up, the relevant 2-D hydrodynamical equations are (see, for example, Vallis, 2006), the momentum equation, the continuity equation and the energy equation:

$$\frac{\mathrm{D}\mathbf{u}}{\mathrm{D}t} = -\frac{1}{\rho}\nabla p + \mathbf{g}\,, \tag{2.20a}$$

$$\frac{\mathrm{D}\rho}{\mathrm{D}t} = -\rho\nabla\cdot\mathbf{u}\,, \tag{2.20b}$$

$$\frac{\mathrm{D}\theta}{\mathrm{D}t} = 0\,, \tag{2.20c}$$

where $\mathbf{u} \equiv (u, w)$ is the flow in (x, z) and $\mathbf{g} \equiv (0, -g)$ is the acceleration due to gravity. The operators are the material derivative, $\mathrm{D}/\mathrm{D}t \equiv (\partial/\partial t + \mathbf{u}\cdot\nabla)$, and the two-dimensional gradient, $\nabla \equiv (\partial/\partial x, \partial/\partial z)$. These equations are augmented with the ideal gas equation of state, Equation (2.2), and the definition of potential temperature, Equation (2.3), which close the system.

The thermodynamic properties of the atmosphere are assumed to have a mean background state, indicated by a subscript 0, that varies only with altitude. Perturbations in space and time, indicated by a subscript 1, are superimposed

on the background:

$$\rho\left(x,z,t\right)=\rho_0\left(z\right)+\rho_1\left(x,z,t\right)\,, \tag{2.21a}$$

$$p\left(x,z,t\right)=p_0\left(z\right)+p_1\left(x,z,t\right)\,, \tag{2.21b}$$

$$\theta\left(x,z,t\right)=\theta_0\left(z\right)+\theta_1\left(x,z,t\right)\,. \tag{2.21c}$$

The background is taken to be in hydrostatic balance, which gives

$$\frac{\mathrm{d}p_0}{\mathrm{d}z}=-g\rho_0\,. \tag{2.22}$$

The perturbation quantities are small compared to the background quantities. This allows the approximation,

$$\left(\xi_0+\xi_1\right)^{\upsilon}\approx\xi_0^{\upsilon}\left(1+\upsilon\frac{\xi_1}{\xi_0}\right)\,, \tag{2.23}$$

to be used. The velocity fields are also decomposed into a background profile with superimposed perturbations. Here there is no requirement for the perturbation to be small compared to the background. Indeed, all vertical flows are treated as perturbations from a still background by taking $w_0=0$. This is reasonable as the background is assumed to be in hydrostatic balance. This gives,

$$u\left(x,z,t\right)=u_0\left(z\right)+u_1\left(x,z,t\right)\,, \tag{2.24a}$$

$$w\left(x,z,t\right)=w_1\left(x,z,t\right)\,. \tag{2.24b}$$

Finally, it is assumed that terms which are products of perturbation quantities (i.e., second order or higher perturbations) can be neglected.

2.2.3 Treatment of the Continuity Equation

The removal of sound waves from the possible solution set of the fluid equations is beneficial. The effects of sound waves are, in general, physically unimportant in atmospheric studies and their removal allows theoretical studies to concentrate on the physically relevant phenomena. Further, removing sound waves allows numerical studies to use larger time steps whilst retaining numerical stability (Durran, 1998).

There are several ways to filter sound-wave solutions. For example, requiring the atmosphere to be hydrostatic filters all sound waves, except for horizontally-propagating Lamb waves. This is the usual situation in GCMs that use traditional primitive equations (Holton, 2004). However, in the TGE sound waves are filtered by approximating the continuity equation and the variation of the thermodynamic variables. There several variations to the way the continuity equation is treated. The effect of some of them on Equation (2.20) are discussed below.

The Constant Density Approximation

The simplest approach is to assume that the density and potential temperature profiles can be represented by some mean value. That is, in effect, to assume that the fluid has constant density and potential temperature. The fluid is therefore incompressible and the continuity equation can be reduced to

$$\nabla \cdot \mathbf{u} = 0. \tag{2.25}$$

The perturbations in the thermodynamic properties of the fluid must be small compared to the mean values. Thus the inertia of the flow, related to the product of density and velocity, is assumed to be little affected by density perturbations. However, gravity is strong, thus it cannot be assumed that the buoyancy, related to the product of gravity and density, is unaffected by density perturbations. This allows terms that include the density perturbation to be neglected as small except where involving gravity. As shown by Spiegel and Veronis (1960) to be a valid approximation this requires the depth of the fluid to be much less than the fluid's scale height. The studies here presented consider waves moving in atmospheres that are 10 or more scale heights in depth so the constant density approximation is not appropriate for this work.

The Boussinesq Approximation

The Boussinesq flow is similar to a constant density flow giving the same equation set but one where the thermodynamic variables are allowed to vary significantly with height. Changes in density are ignored except when multiplied by gravity. In this approximation the flow is again treated as incompressible and

so Equation (2.25) is used to approximate the continuity equation. As shown in Batchelor (1967) to be valid this requires the Mach number of the flow to be much less than 1 and the vertical scale of the motion to be small compared to the fluid scale height. The former is generally valid in the Solar System; for example the maximum observed flows on Jupiter are far below the speed of sound (Ingersoll, 1990). However, this may not be the case on hot-Jupiter planets where some modelling and observational studies have claimed to find supersonic or near supersonic winds (Cooper and Showman, 2005). On the Earth this regime may be appropriate for studying many aspects of gravity wave theory (e.g. Nappo, 2002), however in Chapters 3 and 4 gravity waves with wavelengths of the order of a scale height ($\sim$ 27 km for Jupiter and $\sim$ 480 km for HD 209458 b) are considered. Therefore the TGE derived using the Boussinesq approximation is not used in later chapters.

The Anelastic Approximation

There are several versions of the anelastic approximation. In all cases the continuity equation is approximated as

$$\nabla \cdot (\rho_0 \mathbf{u}) = 0\,, \tag{2.26}$$

and the vertical scale of the motion is allowed to be of the order of a scale height. However, the wave speed must be much less than that of sound. This is the case for the gravity waves studies in the following chapters. The equation set proposed by Ogura and Phillips (1962) assumes a constant background mean potential temperature from which there are small deviations. This set of equations was extended in Wilhelmson and Ogura (1972) by allowing the background potential temperature to vary with height, however, this results in an equation set that does not conserve energy. The equations in Lipps and Hemler (1982) assumes a slowly varying background potential temperature and allows energy to be conserved. Interestingly, although there are differences between the two equation sets in Ogura and Phillips (1962) and Lipps and Hemler (1982) they both lead to the the same form of the TGE. However, in the Ogura and Phillips (1962) version the *Brunt–Väisälä* frequency is constant. The anelastic version of the TGE is used in this thesis.

The Pseudo-Incompressible Approximation

Durran (1989) proposed the pseudo-incompressible approximation. Here the continuity equation is approximated by

$$\nabla \cdot (\rho_0 \theta_0 \mathbf{u}) = 0\,, \tag{2.27}$$

and energy is conserved. It is assumed that the effect that the pressure perturbation has on the density perturbation is negligible. In common with the other approximations it requires that the speed of the motion is much smaller than the sound speed, however it only requires that pressure perturbations are small. This is a useful property but is not essential for this study as when perturbations in θ become large non-linear phenomena become important for gravity waves and they saturate, see Section 2.5.2 for details. A pseudo-incompressible version of the TGE is, to my knowledge, derived for the first time in Section 2.3.1.

2.3 The Taylor-Goldstein Equation

2.3.1 Derivation of the TGE

Combining the equation of state Equation (2.2) with Equation (2.3) and linearising gives,

$$\frac{\theta_1}{\theta_0} = -\frac{\rho_1}{\rho_0} + \frac{1}{\gamma}\frac{p_1}{p_0}\,. \tag{2.28}$$

Applying the linearisation described above in Equations (2.21) and (2.24) along with the various treatments of the continuity equation to Equation (2.20) then

Equation set	σ_1	σ_2	σ_3
Constant Density	0	0	0
Boussinesq	1	0	0
Anelastic	0	1	0
Pseudo-incompressible	0	1	1

Table 2.1 – Approximations of the fluid equations

using Equation (2.28) gives the following set of switched equations

$$\frac{\mathrm{D}u_1}{\mathrm{D}t} + u_0' w_1 + \frac{\partial \Phi_1}{\partial x} = 0\,, \tag{2.29a}$$

$$\sigma_{nh}\frac{\mathrm{D}w_1}{\mathrm{D}t} + \frac{\partial \Phi_1}{\partial z} - \sigma_1 \frac{\Phi_1}{H_\theta} - g\Theta_1 = 0\,, \tag{2.29b}$$

$$\frac{\partial u_1}{\partial x} + \frac{\partial w_1}{\partial z} - \sigma_2 \frac{w_1}{H_\rho} + \sigma_3 \frac{w_1}{H_\theta} = 0\,, \tag{2.29c}$$

$$\frac{\mathrm{D}\Theta_1}{\mathrm{D}t} + \frac{N^2}{g} w_1 = 0\,, \tag{2.29d}$$

where the new variables $\Phi_1 = p_1/\rho_0$ and $\Theta_1 = \theta_1/\theta_0$, have been introduced. Also note that here the operator $\mathrm{D}/\mathrm{D}t \equiv (\partial/\partial t + u_0 \partial/\partial x)$ and a prime indicates differentiation w.r.t. z. The switches indicate which terms are used to derive each of the versions of the TGE using the various approximations of the continuity equation discussed above and shown in Table 2.1. Note that switch σ_{nh} when equal to 1 produces a non-hydrostatic version of the equation and a hydrostatic version when equal to 0.

Now, it is assumed that the solutions in the perturbations are wavelike in the horizontal and in time, so, new variables are introduced as follows:

$$u_1(x,z,t) = \tilde{w}(z) e^{ik(x-ct)}\,, \tag{2.30a}$$

$$w_1(x,z,t) = \tilde{u}(z) e^{ik(x-ct)}\,, \tag{2.30b}$$

$$\Theta_1(x,z,t) = \tilde{\Theta}(z) e^{ik(x-ct)}\,, \tag{2.30c}$$

$$\Phi_1(x,z,t) = \tilde{\Phi}(z) e^{ik(x-ct)}\,, \tag{2.30d}$$

where k is the horizontal wavenumber, c is the horizontal phase speed and it

is understood that the real part is to be taken. Thus, the substitutions,

$$\frac{\partial}{\partial x} \mapsto ik\,, \tag{2.31a}$$

$$\frac{\mathrm{D}}{\mathrm{D}t} \mapsto -ik(c-u_0)\,, \tag{2.31b}$$

can be made to Equation (2.29) to give

$$-ik\,(c-u_0)\,\tilde{u} + u_0'\tilde{w} + ik\tilde{\Phi} = 0\,, \tag{2.32a}$$

$$-\sigma_{nh}ik\,(c-u_0)\,\tilde{w} + \tilde{\Phi}' - \frac{\sigma_1}{H_\theta}\tilde{\Phi} - g\tilde{\Theta} = 0\,, \tag{2.32b}$$

$$ik\tilde{u} + \tilde{w}' - \left(\frac{\sigma_2}{H_\rho} - \frac{\sigma_3}{H_\theta}\right)\tilde{w} = 0\,, \tag{2.32c}$$

$$-ik\,(c-u_0)\,\tilde{\Theta} + \frac{N^2}{g}\tilde{w} = 0\,. \tag{2.32d}$$

The quantity $(c-u_0)$ is known as the intrinsic phase speed. It is the phase speed of the wave in the reference frame of the flow. It has an important role in the behaviour of linear waves, especially in the breakdown of the linear theory at critical layers, where it becomes zero and the TGE becomes singular, see Section 2.5.2 for details. Eliminating $\tilde{u}$, $\tilde{\Theta}$ and $\tilde{\Phi}$ in Equation (2.32) gives a second order differential equation in $\tilde{w}$,

$$\tilde{w}'' - \upsilon\,(z)\,\tilde{w}' + \psi\,(z)\,\tilde{w} = 0\,, \tag{2.33}$$

where

$$\upsilon = \frac{\sigma_2}{H_\rho} + \frac{\sigma_1 - \sigma_3}{H_\theta}\,, \tag{2.34a}$$

$$\psi = \frac{N^2}{(c-u_0)^2} + \frac{u_0''}{(c-u_0)} + \left(\frac{\sigma_2}{H_\rho} - \frac{\sigma_1+\sigma_3}{H_\theta}\right)\frac{u_0'}{(c-u_0)} + \frac{\sigma_2 H_\rho'}{H_\rho^2} - \frac{\sigma_3 H_\theta'}{H_\theta^2} - \sigma_{nh}k^2\,. \tag{2.34b}$$

Finally, a new variable is introduced,

$$\hat{w} = \tilde{w}\exp(-\chi(z))\,, \tag{2.35}$$

where

$$\chi(z) = \frac{1}{2}\int_{z_s}^{z} \upsilon(\zeta)\mathrm{d}\zeta\,. \tag{2.36}$$

Substituting Equation (2.35) into Equation (2.33) gives the canonical form of the TGE,

$$\hat{w}'' + m^2(z)\hat{w} = 0\,, \tag{2.37}$$

where m is known as the index of refraction. The equation can be thought of as a harmonic oscillator with m being the local vertical wavenumber given by,

$$\begin{aligned} m = \Bigg[& \frac{N^2}{(c-u_0)^2} + \frac{u_0''}{(c-u_0)} + \left(\frac{\sigma_2}{H_\rho} - \frac{\sigma_1+\sigma_3}{H_\theta}\right)\frac{u_0'}{(c-u_0)} \\ & - \left\{\sigma_2\left(\frac{1-2H_\rho'}{4H_\rho^2}\right) + (\sigma_1+\sigma_3)\left(\frac{1+2H_\theta'}{4H_\theta^2}\right) - \frac{\sigma_3}{2H_\rho H_\theta}\right\} - \sigma_{nh}k^2\Bigg]^{1/2}. \end{aligned} \tag{2.38}$$

The index of refraction consists of five terms: the buoyancy term, curvature term, shear term, scale height term and non-hydrostatic term. Note in cases where the wave is *a priori* to be considered as hydrostatic—e.g., when $N^2 \gg \omega^2$ where ω is the wave frequency (Lindzen, 1990)—that the non-hydrostatic switch should be set to zero, $\sigma_{nh} = 0$, and the hydrostatic term does not appear. However, in general, the key contributors to m are the buoyancy and non-hydrostatic terms. The other three terms contribute to the detailed behaviour of the wave, but it is generally the buoyancy and non-hydrostatic terms that control whether the wave propagates. This is because, in practice, the shear and curvature of the flow is small and the scale height large. For waves with large horizontal wavelengths, the non-hydrostatic term is small and the waves can be taken to be hydrostatic; then, the buoyancy term dominates. In these cases, as long as the atmosphere is stratified (i.e., $N^2 > 0$) and $c \neq u_0$, the wave will propagate vertically. However, for shorter, non-hydrostatic waves, it is possible that $k^2 > [N/(c-u_0)]^2$. In these cases, m is imaginary and the wave does not propagate vertically, even in a stratified atmosphere. This situation is discussed in the context of extrasolar planets in Chapter 3.

For the constant density case the TGE takes the form,

$$\hat{w}'' + \left[\frac{N^2}{(c-u_0)^2} + \frac{u_0''}{(c-u_0)} - \sigma_n k^2\right]\hat{w} = 0\,. \tag{2.39}$$

Note that in this case, since $\upsilon(z) = 0$, then $\tilde{w} = \hat{w}$. This version with a stationary atmosphere ($u_0 = u_0'' = 0$) is discussed in Lindzen (1990).

In the Boussinesq case the flow is incompressible so that $H_\theta = H_\rho$, as discussed in Section 2.1.5. This gives the TGE as,

$$\hat{w}'' + \left[\frac{N^2}{(c-u_0)^2} + \frac{u_0''}{(c-u_0)} - \frac{u_0'}{H_\rho (c-u_0)} - \frac{1+2H_\rho'}{4H_\rho^2} - \sigma_n k^2 \right] \hat{w} = 0\,. \quad (2.40)$$

The Boussinesq approximation is used in the derivation of the TGE in the original papers by Taylor (1931) and Goldstein (1931). It has been used by Umurhan and Heifetz (2007) in their exploration of Holmboe waves, and it is the form used by Nappo (2002) – albeit with H_ρ taken as constant; thus, $H_\rho' = 0$.

The anelastic TGE takes the form,

$$\hat{w}'' + \left[\frac{N^2}{(c-u_0)^2} + \frac{u_0''}{(c-u_0)} + \frac{u_0'}{H_\rho (c-u_0)} - \frac{1-2H_\rho'}{4H_\rho^2} - \sigma_n k^2 \right] \hat{w} = 0\,. \quad (2.41)$$

Note the sign changes from Equation (2.40). This version has been used to study the stability of protoplanetary discs (Garaud and Lin, 2004) and, with the assumption that H_ρ is constant, in the review of gravity waves by Fritts (1984). The anelastic form of the TGE is used in the remainder of this thesis, due to the large vertical wavelengths of the waves considered.

The pseudo-incompressible version, after using Equation (2.17), takes the form,

$$\hat{w}'' + \left[\frac{N^2}{(c-u_0)^2} + \frac{u_0''}{(c-u_0)} + \frac{u_0'}{\gamma H_p (c-u_0)} - \frac{1-2\gamma H_p'}{4\gamma^2 H_p^2} - \sigma_n k^2 \right] \hat{w} = 0\,. \quad (2.42)$$

This is, to my knowledge, the first time that a pseudo-incompressible version of the TGE has been obtained.

2.3.2 Solution of the TGE

The full equation set, Equations (2.2), (2.3) and (2.20), can be solved using various numerical techniques such as the finite difference method and the pseudo-spectral method (see e.g. Durran, 1989). However, such a solution

admits waves, such as sound waves, which are not important for this study. Further, as the gravity waves studied here are meso-scale phenomena the level of resolution required for the solution would be computationally expensive. Therefore, the gravity waves are studied by solving the TGE.

Constant Density Case

As already alluded to, the TGE is a harmonic oscillator and when m is real and constant the solution $\hat{w}$ is a simple sinusoid. The transformation described in Equation (2.35) compensates for the fall in density with height. Thus, the vertical velocity perturbation $\tilde{w}$ grows exponentially with height. Therefore, in the constant density case the solution amplitude does not grow with altitude.

The Wentzel–Kramers–Brillouin (WKB) Solution

When the temperature and zonal flow varies with height, m is a function of z and the solution of the TGE is less straightforward than when m is a constant. If m varies slowly (that is, the change in m over a scale height is small compared to m), the WKB approximation (Bender and Orszag, 1999) can be used to obtain,

$$\tilde{w}(z) = \frac{Ae^{z/2H_\rho}}{m^{1/2}} \exp\{\pm i \int_{zb}^{z} m\,(\zeta)\,\mathrm{d}\zeta\}\,. \tag{2.43}$$

Here, $A = \tilde{w}(z_b)\,[m(z_b)]^{1/2}$. As in the constant m case, the vertical perturbation velocity is wave-like with upwardly and downwardly propagating components; the amplitude of the upward component grows with height and the downward decays with depth. However, when the variation of m is not small then the solution must be obtained numerically, as described below.

Boundary Conditions

In order to select the exact solution the boundary conditions of the problem need to be applied. This study uses a radiation condition, selecting the upwardly propagating solution at the top boundary z_t and the downwardly propagating solution at the lower boundary z_b. This is achieved using the

condition,

$$\hat{w}' + \left(ism + \frac{m'}{2m} \right) \hat{w} = 0 \,. \tag{2.44}$$

Here, $s = \pm 1$ depends on the signs of the horizontal phase speed and intrinsic phase speed as well as whether the condition is being applied at the top of bottom boundary. Note that this condition depends on the WKB approximation solution, Equation (2.43), and so requires the WKB solution to be valid at the boundaries. For example, the boundaries cannot be critical layers (see Section 2.5.2) since in such regions $(c - u_0) \to 0$. Thus, $m \to \infty$ and the WKB approximation ceases to be valid.

Numerical Solution

Generally, in this thesis the TGE is solved numerically. The domain over which the equation is to be solved is divided into n levels. Then the TGE, for example Equation (2.41), can then be written in matrix form as

$$(\mathbf{D} + \mathbf{M})\, \mathbf{w} = \mathbf{F} \,, \tag{2.45}$$

where $\mathbf{w}$ is a n-entry column vector of $\hat{w}$ at each level, $\mathbf{D}$ is an $n \times n$ matrix representing the second order finite difference form of the second derivative with the top and bottom rows modified to reflect the boundary conditions; $\mathbf{M}$ is an $n \times n$ diagonal matrix with the value of m^2 at each level and $\mathbf{F}$ is the forcing at each level. Note that the representation of forcing is discussed below. The solution $\mathbf{w}$ can be obtained by inverting Equation (2.45),

$$\mathbf{w} = (\mathbf{D} + \mathbf{M})^{-1}\, \mathbf{F} \,. \tag{2.46}$$

The inversion can be achieved by several methods (e.g., Lindzen and Kuo, 1969). This study uses the "mldivide" routine in the proprietary Matlab package. The number of levels used affects the accuracy of the calculation. It was found that using 3000 levels provided an excellent level of accuracy and there was little improvement in using 10000 levels. An example solution in an isothermal atmosphere showing the exponential growth of $\tilde{w}$ is shown in Figure 2.1.

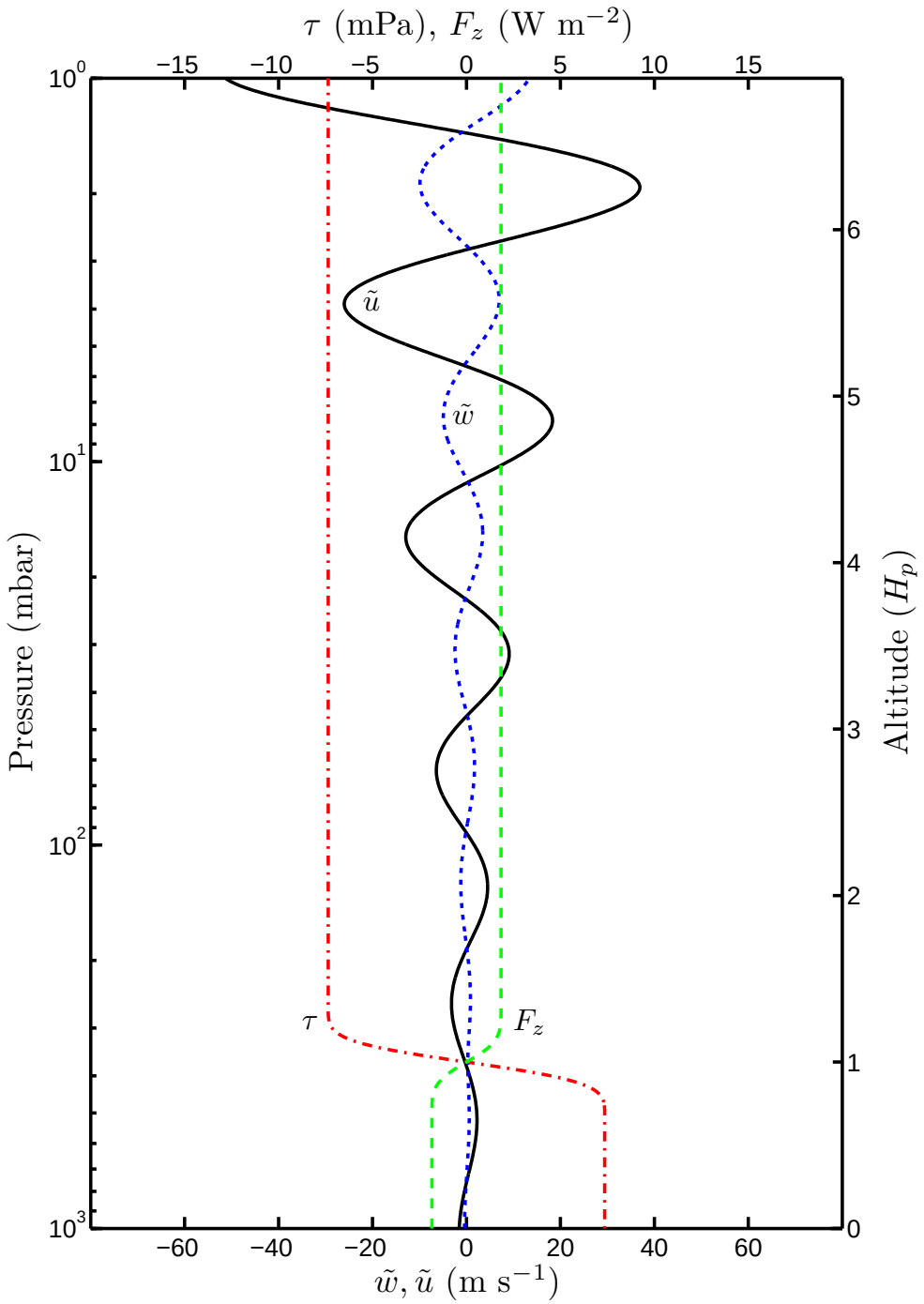

Figure 2.1 – A gravity wave propagating in an isothermal (T_0 = 1350 K) atmosphere with constant background flow (u_0 = 350 m s^{-1}). The horizontal phase speed of the wave c is 100 m s^{-1} and the horizontal wavelength $2\pi/k$ is 2500 km. The vertical perturbation velocity $\tilde{w}$ (···), horizontal perturbation velocity $\tilde{u}$ (—), vertical energy flux F_z (- - -) and wave stress τ (-·-) are shown. The latter is the vertical transport of horizontal momentum. Wave amplitudes, $\tilde{u}$ and $\tilde{w}$, grow exponentially with height, but the wave stress is constant with height, since there is no dissipation. The jump in τ and F_z at $z/H_p = 1$ is caused by the forcing.

Forcing

Perhaps the most familiar gravity wave is that which forms in the lee of mountains when winds blow over them. These are modelled by introducing the mountain through the lower boundary condition (e.g. Nappo, 2002). On giant planets mountain ranges do not exist, though convective plumes that well up from the interior and overshoot into the atmosphere may have similar effects. The forcing used here is thermal forcing, such as that from the release of latent heat during cloud formation. The net diabatic heating rate, $\dot{Q}$, is included in the energy equation (2.20c) to give,

$$\frac{\mathrm{D}\theta}{\mathrm{D}t} = \frac{\theta}{c_p T}\dot{Q}\,. \tag{2.47}$$

This leads to the forced TGE,

$$\hat{w}'' + m^2(z)\hat{w} = \frac{\kappa\dot{Q}}{H_p\left(c-u_0\right)^2}e^{-\chi}\,, \tag{2.48}$$

the right-hand side of which is used to produce $\mathbf{F}$ in Equation (2.45). The vertical structure of $\dot{Q}$ is taken to be a modified Gaussian,

$$\dot{Q} = \begin{cases} \dot{Q}_{peak}\left[\exp\left(-\dfrac{z-z_f}{z_w}\right)^2 - \exp\left(-4\right)\right], & \text{if } |z-z_f| < 2z_w\,, \\ 0, & \text{otherwise }, \end{cases} \tag{2.49}$$

where $\dot{Q}_{peak}$ is the amplitude of the forcing, z_f is the centre of the forcing and z_w is the half-width. The vertical extent of the forcing compared to the horizontal wavelength has an important influence on the amplitude of the emitted wave. The amplitude of the emitted wave and its wave stress (see Section 2.4.2) grows as the extent of the forcing grows until the half-width of the forcing reaches roughly 1/4 of the vertical wavelength. Forcing of this nature is characterised as "thin" forcing. This is illustrated by Figure 2.1, where z_w is roughly 1/8 of the vertical wavelength, and Figure 2.2, where z_w is roughly 1/4 of the vertical wavelength. In the latter the wave stress is larger. However, further increases in the extent of the forcing lead to a fall in the size of the emitted wave, this is known as "broad" forcing (Lindzen, 1990). This is illustrated in Figure 2.3, where z_w is rougly 1/2 of the vertical wavelength and the wave stress has fallen

in magnitude.

2.4 Polarisation Relations and Fluxes

2.4.1 Polarisation Relations

As shown above, the solution to the TGE is a wave in the vertical velocity perturbation, $\tilde{w}$. This can be related to perturbations in the other key variable by the polarisation equations (Hines, 1960). This is useful, as $\tilde{w}$ is not always known: observations are often in other variables such as pressure or temperature. The polarisation relations allow these observations to be tied into the theory, an application of this is shown in Chapter 4. Further, understanding these is essential for parametrising the saturation process that occurs in the full non-linear situation, discussed below. The polarisation equations for the anelastic TGE, derived from Equation (2.32), are:

$$\tilde{u} = \frac{i}{k}\left[\tilde{w}' - \frac{\tilde{w}}{H_\rho}\right], \tag{2.50a}$$

$$\tilde{\Phi} = \frac{i}{k}\left[(c-u_0)\left(\tilde{w}' - \frac{\tilde{w}}{H_\rho}\right) + u_0'\tilde{w}\right], \tag{2.50b}$$

$$\tilde{\theta} = -\frac{i}{k}\left[\frac{\theta_0 N^2}{g\,(c-u_0)}\right]\tilde{w}\,, \tag{2.50c}$$

$$\tilde{T} = \frac{T_0}{\theta_0}\,\tilde{\theta} + \frac{\tilde{\Phi}}{c_p}\,. \tag{2.50d}$$

The relationship between the vertical and horizontal perturbation velocities Equation (2.50a) shows that the amplitude of $\tilde{u}$ is generally greater than the amplitude of $\tilde{w}$, as it is scaled by $1/kH_\rho$ with the horizontal wavelength being greater than a scale height. Further, $\tilde{\Phi}$ varies with the background flow via a dependence on the the intrinsic phase speed as evidenced by Equation (2.50b). The potential temperature perturbations are $\pi/2$ out of phase with $\tilde{w}$, whereas the phase differences of $\tilde{u}$ and $\tilde{\Phi}$ vary locally.

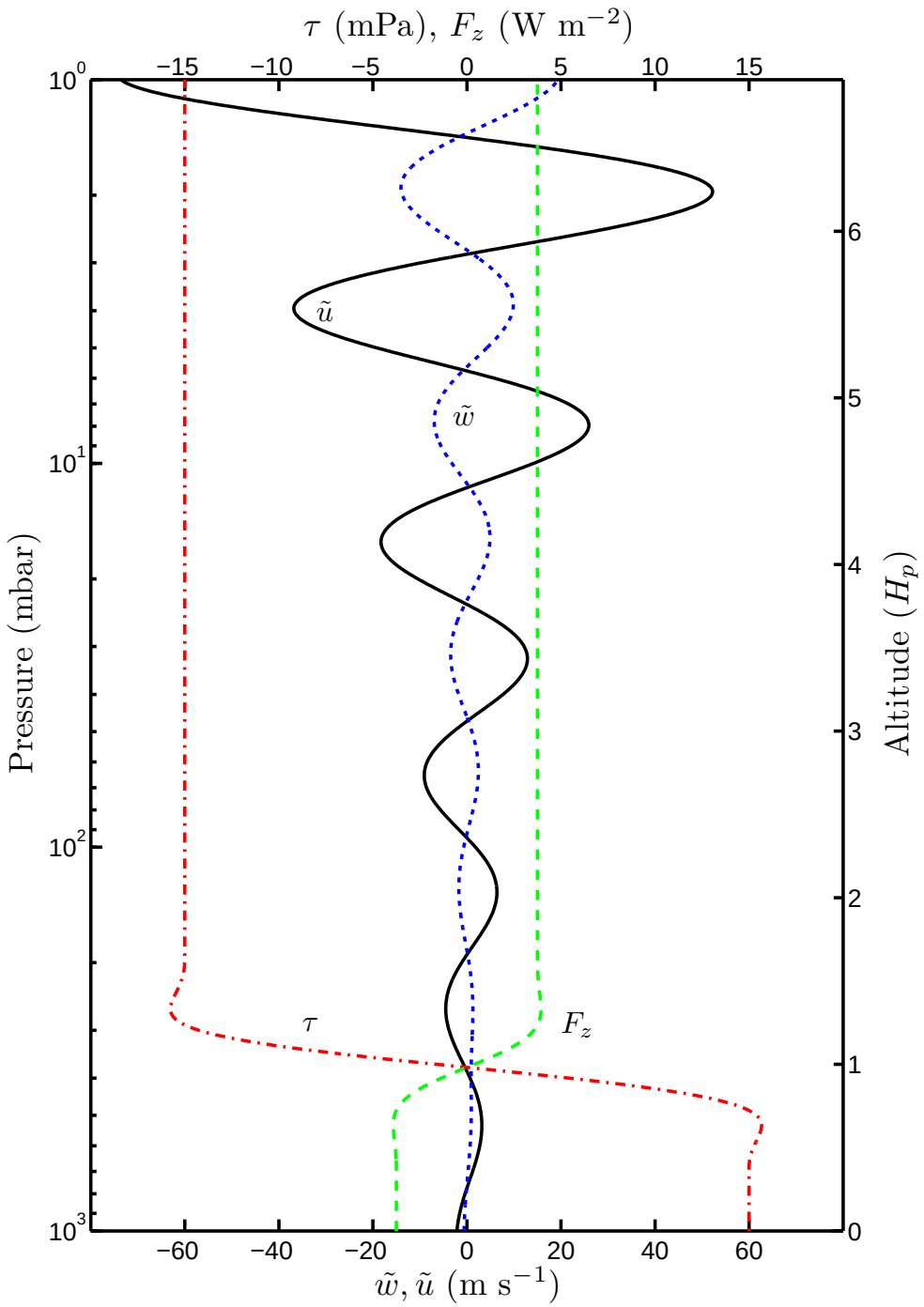

Figure 2.2 – As with Figure 2.1 except that the width of forcing is twice as large, with $z_w = 150$ km. This is approximately 1/4 of the vertical wavelength, approximately the optimal size for maximising the size of the emitted wave. The vertical perturbation velocity $\tilde{w}$ (···), horizontal perturbation velocity $\tilde{u}$ (—), vertical energy flux F_z (- - -) and wave stress τ (-·-) are shown. Note that the magnitudes of these quantities, especially τ, are larger than in Figure 2.1.

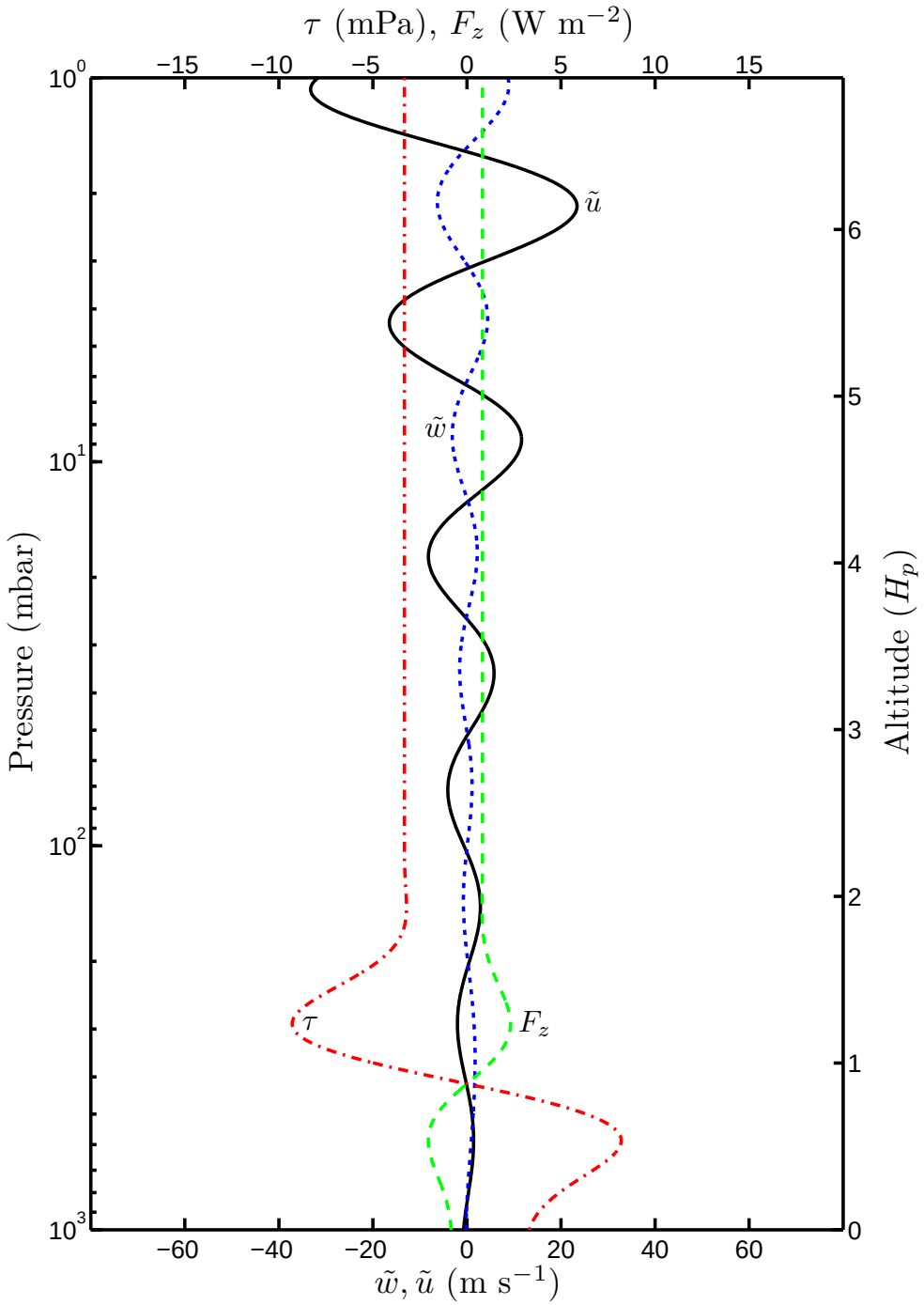

Figure 2.3 – As with Figure 2.1 except that the width of forcing is four times that used in Figure 2.1, i.e. $z_w = 300$ km. The vertical perturbation velocity $\tilde{w}$ (···), horizontal perturbation velocity $\tilde{u}$ (—), vertical energy flux F_z (- - -) and wave stress τ (-·-) are shown. Note that the magnitudes of these quantities, especially τ, are smaller than than in both Figure 2.1 and Figure 2.2. This is because z w is now greater than 1/4 of the vertical wavelength and the forcing is now broad.

2.4.2 Wave Fluxes

Gravity waves are an efficient means of transporting both momentum and energy. The (perturbation) momentum and energy fluxes are simply obtained from the polarisation relations Equation (2.50):

$$\tau = \rho_0 \overline{\tilde{u}\tilde{w}}\,, \tag{2.51a}$$

$$F_x = \rho_0 \overline{\tilde{\Phi}\tilde{u}}\,, \tag{2.51b}$$

$$F_z = \rho_0 \overline{\tilde{\Phi}\tilde{w}}\,. \tag{2.51c}$$

Here, τ is the vertical flux of horizontal momentum (or, the wave stress); F_x and F_z are, respectively, the horizontal and vertical fluxes of energy; and the overbar indicates an average over a wavelength (or zonal average),

$$\overline{\alpha\beta} = \frac{1}{2}\Re\left(\alpha\beta^*\right)\,, \tag{2.52}$$

where α and β are arbitrary complex functions and the asterisk denotes the complex conjugate. Note that the energy fluxes depend on the background flow through $\tilde{\Phi}$. However, as can be seen in Figure 2.4, the wave stress remains constant (i.e. $\tau' = 0$) away from the forcing and damping regions—e.g. critical layers and regions where the wave saturates. This is in accordance with the second Eliassen-Palm theorem (Eliassen and Palm, 1960), which expresses non-interaction of the disturbance in the absence of dissipation and forcing.

Upwardly propagating waves are defined as waves that have upwardly propagating energy – i.e., $F_z > 0$. These are the waves considered in this thesis. However, it must be remembered that downward propagating waves are also generated; see, for example, the bottom of Figure 2.4, where $F_z < 0$. On a giant planet without a solid surface, those waves may not be reflected or absorbed. They can continue to penetrate downward until they encounter a critical level or a convective region. Or, they are dissipated since the amplitudes of the downwardly propagating waves decrease exponentially. Downwardly propagating planetary scale gravity waves (i.e., thermally excited tides) are considered by Gu and Ogilvie (2009).

The energy and momentum fluxes are linked by the first Eliassen-Palm theorem

(Eliassen and Palm, 1960),

$$F_z = (c - u_0)\,\tau\,, \tag{2.53}$$

which can be derived from Equation (2.50) and Equation (2.51). This shows that F_z is not a good measure of the size of a wave as its magnitude depends on the background. This is illustrated in Figure 2.4, where in an atmosphere with wind shear τ is constant but F_z decreases with height.

2.5 Saturation and Critical Layers

2.5.1 Saturation

The theory so far presented describes inviscid, linear, monochromatic waves. Such waves are infinite in extent and, in principle, can grow without limit when they propagate upward. This is obviously not physical. In reality, such waves become unstable and saturate. The saturation process can be treated by introducing a correction to the solution in regions where the wave is identified as saturating based on the convective instability. As discussed in Section 2.1.4, an atmosphere is convectively unstable where the potential temperature gradient is negative. Although a wave propagates in a stable atmosphere, the wave itself produces perturbations in the potential temperature field, as shown by Equation (2.50c). As the wave propagates upwards these perturbations grow in size. Eventually these perturbations become large enough that, locally, the potential temperature gradient becomes negative; the atmosphere becomes locally convective. The wave is then unstable and breaks. The breaking balances the amplitude growth so that the potential temperature gradient remains at zero. This is analogous to ocean waves breaking as they run up a beach where just the top of wave breaks (Nappo, 2002). Thus, a wave with a large enough amplitude will induce the atmosphere to become locally unstable when

$$\frac{\partial}{\partial z}\left(\theta_0 + \tilde{\theta}\right) < 0\,. \tag{2.54}$$

This criterion is used to identify regions where the wave is saturating. In these regions $\tilde{\theta}$ is adjusted so that the neutral stability is maintained. Then, via

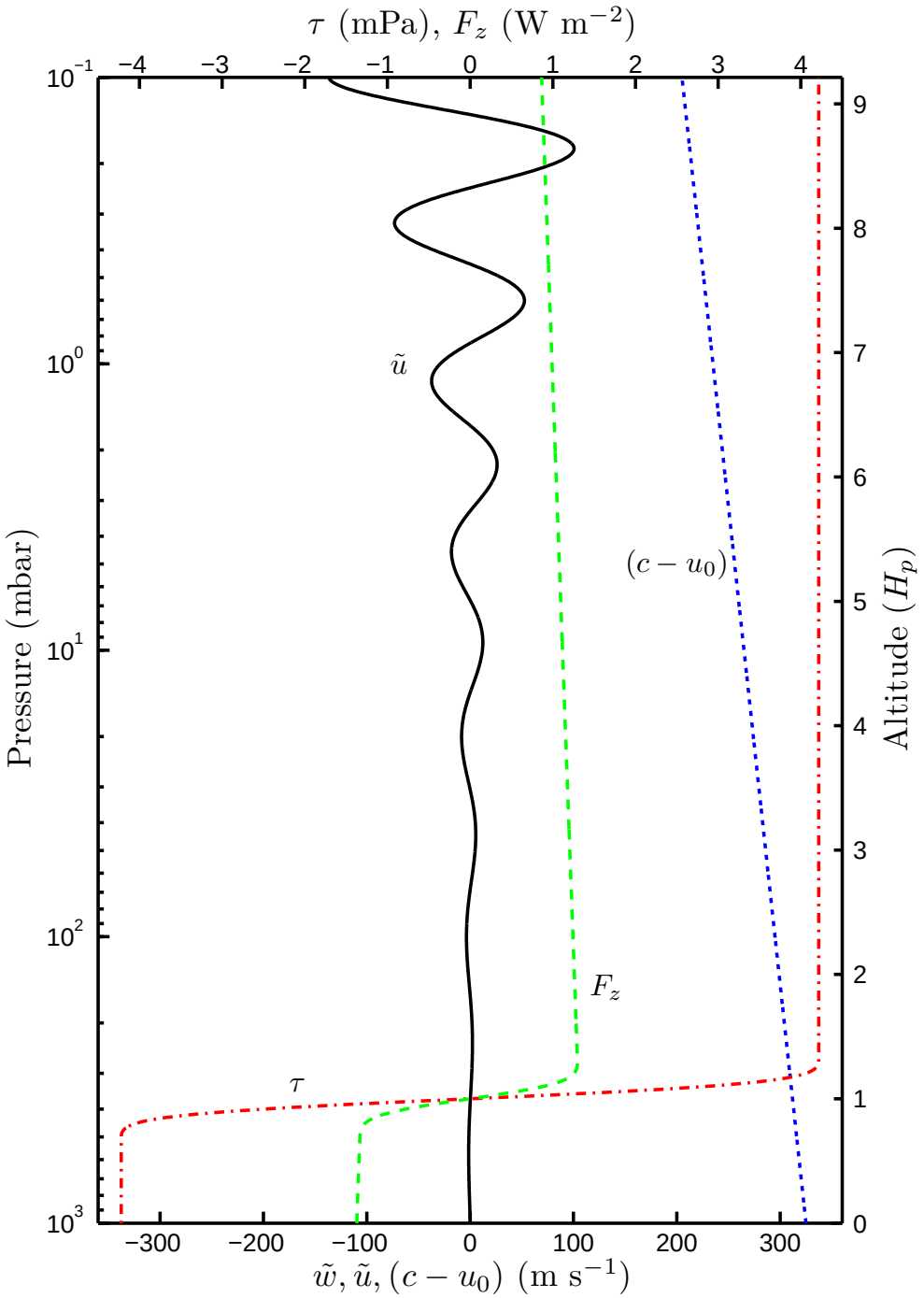

Figure 2.4 – A wave with $c = 500$ m s^{-1} and $k = 2\pi/250$ km^{-1} propagating in a sheared isothermal atmosphere. The horizontal perturbation velocity $\tilde{u}$ (—), vertical energy flux F_z (- - -), wave stress τ (-·-) and the intrinsic phase speed $(c - u_0)$ (···) are shown. Note that the magnitude of F_z falls with altitude due to the wind shear (in accordance with the first Eliassen-Palm theorem) and τ remains steady away from the forcing (in accordance with the second Eliassen-Palm theorem).

the polarisation Equations (2.50) the values for the other fields are obtained. Where the WKB approximation is valid, this process for handling saturation condition acquires the simple form of putting

$$|\tilde{u}| = |c - u_0| \tag{2.55}$$

in the regions where the wave is saturating (Fritts, 1984).

2.5.2 Critical Layer

If the background flow contains shear, it is possible for the wave to encounter a critical layer, where $c = u_0$, at some height. In the region below the critical layer the magnitude of the intrinsic phase speed falls to zero as z increases to the altitude of the critical layer, see Figure 2.5 for an example. However, the amplitude of the zonal velocity perturbations grow as the wave propagates upward. So, at some point in the region, Equation (2.55) is satisfied and the wave saturates. The wave dissipates as it propagates toward the critical layer, as the intrinsic phase speed falls to zero, so that the atmosphere does not become convective. The wave breaks turbulently and becomes attenuated, see, for example, Sutherland (2010) for output from a laboratory experiment that illustrates this process.

At a critical layer the TGE becomes singular. However, the equation can be solved using the method of Frobenius (Bender and Orszag, 1999), from which it is seen that the wave is, in general, drastically attenuated by the critical layer (Booker and Bretherton, 1967). The amount of attenuation depends on the Richardson number Ri of the flow,

$$Ri = \frac{N^2}{\left(u_0'\right)^2}\,. \tag{2.56}$$

Figure 2.5 illustrates a wave encountering a critical layer. If the wave stress has magnitude τ below the critical layer, then the magnitude after the encounter with the critical layer is $\tau \exp\{-2\pi \left[Ri - (1/4)\right]^{1/2}\}$ (Booker and Bretherton, 1967). This can be a substantial level of attenuation even for modest values of Ri, as shown in Table 2.2. For example, in the model atmosphere used in Figure 2.5, $Ri \gtrsim 900$; hence, the wave is essentially completely dissipated

Richardson Number	0.5	1	5	10
Attenuation	6.8×10^{-1}	2.9×10^{-2}	2.7×10^{-62}	4.0×10^{-260}

Table 2.2 – Amount of attenuation at a critical layer for various values of Richardson Number

at the critical layer, with the wave stress falling to practically zero and the momentum deposited in the mean flow (as discussed in Section 2.5.3). Note that, during its approach to the critical layer, a wave saturates over a finite layer. However, as discussed above, the presence of a critical layer is not required for saturation.

Critical layers are handled in the numerical scheme by lifting the phase speed from the real axis by adding a small imaginary component: $c = c_r + ic_i$ where $|c_i/c_r| < 10^{-3}$. This introduces a small amount of linear damping and ensures that the neglected non-linear terms do not dominate in the regions where waves become steep and eventually break. Of course, adding damping causes the wave stress to decrease with height and the second Eliassen-Palm theorem to be invalid. However, this effect is small, as can be seen in Figure 2.5: the wave stress falls negligibly between $z/H_\rho \approx 1$, where the forcing is placed, and $z/H_\rho \approx 6$, where saturation begins.

2.5.3 Interaction with Mean Flow

In Figure 2.5, it is important to note that, where the waves stress is changing, the wave is interacting with the background flow. This should be contrasted with the behaviour illustrated in Figure 2.1, where the wave stress is not changing. Changes in the wave stress cause accelerations to the mean flow. Correspondingly, changes in the energy fluxes cause the temperature of the region to change. The rates of these changes are given by

$$\frac{\partial u_0}{\partial t} = -\frac{1}{\rho_0}\frac{\partial \tau}{\partial z}\,, \tag{2.57a}$$

$$\frac{\partial T_0}{\partial t} = -\frac{1}{\rho_0 c_p}\frac{\partial F_z}{\partial z}\,. \tag{2.57b}$$

For upwardly propagating waves the momentum deposited causes the flow to change its velocity to be nearer the phase speed of the wave. Therefore,

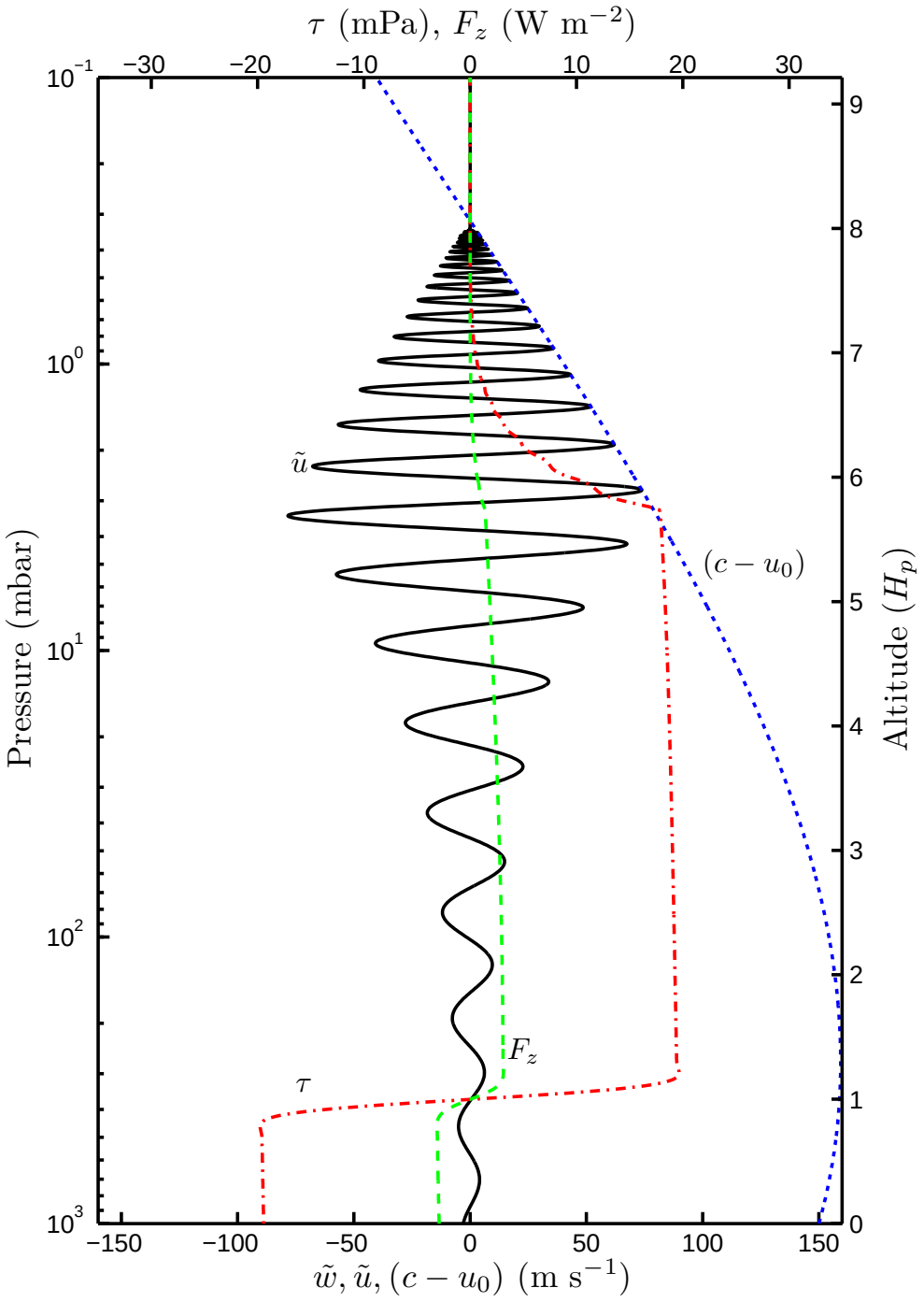

Figure 2.5 – Same as in Figure 2.4 but with stronger wind shear so that a critical layer, where $c = u_0$, exists at about $z/H_p = 8$. The horizontal perturbation velocity $\tilde{u}$ (—), vertical energy flux F_z (- - -), wave stress τ (-·-) and the intrinsic phase speed $(c - u_0)$ (···) are shown. Note that the magnitude of F_z and τ fall rapidly once the wave begins to saturate below the critical layer.

in Figure 2.5, in the saturation region below the critical layer, the flow is accelerated.

Chapter 3

Gravity Waves on Hot Extrasolar Planets: Propagation, Dissipation and Interaction with the Background

In this chapter the theory of gravity waves presented in chapter 2 is used to demonstrate several properties of internal atmospheric gravity waves likely to be important on a hot EGP. It is found that gravity waves can exhibit a wide range of behaviours, even for a single atmospheric profile. The waves can significantly accelerate and decelerate the background mean flow, depending on the difference between the wave phase and mean flow speeds. In addition, the waves can provide significant heating (~ 50 to $\sim 10^3$ K per planetary rotation), especially to the region of the atmosphere above about 10 scale heights from the excitation region. Furthermore, by propagating horizontally, gravity waves provide a mechanism for transporting momentum and heat from the day-side of a tidally locked planet to its night-side. Also discussed is the work that needs to be undertaken to incorporate these effects in current atmosphere models of extrasolar planets.

In the terrestrial atmosphere, a typical gravity wave has an energy flux of approximately 10^{-3} to 10^{-1} W m^{-2} (Gossard, 1962; Hines, 1960). This is small

Parameter	Symbol	Value
Specific gas constant	R	3523 J kg^{-1} K^{-1}
Specific heat at constant pressure	c_p	12300 J kg^{-1} K^{-1}
Acceleration due to gravity	g	10 m s^{-1}
Rotation rate	Ω	2.08×10^{-5} s^{-1}
Radius	R_p	94,400 km

Table 3.1 – Parameters for HD 209458 b

compared to the total amount of absorbed solar flux, ~ 237 W m^{-2} (based on a solar constant of ~ 1366 W m^{-2} and an albedo of ~ 0.3). However, gravity waves are responsible for significantly modifying – even dictating – large-scale flow and temperature structures. Several well-known examples of this are the quasi-biennial oscillation (QBO) (Baldwin et al., 2001), reversal of mean meridional temperature gradient in the upper middle atmosphere (Holton, 1982), and generation of turbulence (e.g. Andrews, Holton, and Leovy, 1987). We expect similar effects to be present in the atmospheres of solar and extrasolar giant planets. Moreover, due to the greater irradiation and scale heights on hot extrasolar planets, the acceleration and heating effects of gravity waves can be much stronger on them.

The planet HD 209458 b is chosen as an exemplar of this class of planets, as it is expected to be generic with respect to the properties discussed here. The physical parameters that characterize the planet's atmosphere are given in Table 3.1. Note that g, R and c_p are taken to be constant. In reality these quantities will vary, but this restriction is not unrealistic and does not mitigate the application of the theory presented in Chapter 2 to EGPs or its implications described in this chapter.

3.1 Background Structure and Forcing

As discussed in Section 2.3, the governing equation for internal gravity waves is the TGE. This chapter considers waves that have vertical wavelengths of similar size to the scale height. Hence, the anelastic TGE, Equation (2.41), is used to describe the wave dynamics. As can be seen from the index of refraction, the wave's horizontal phase speed as well as the structure of the

background and of the forcing play a crucial role in determining the detailed structure of the wave. Here we discuss profiles of the latter two appropriate to hot EGPs such as HD 209458 b.

3.1.1 Background Structure

Figure 3.1 shows the mean flow and temperature profiles used to obtain much of the results presented in this chapter. The lower part of both profiles—approximately the 6 scale heights above the 1 bar level—is taken from global circulation simulations of HD 209458 b by Thrastarson and Cho (2010), using the NCAR Community Atmosphere Model (Collins et al., 2004). The profile is from a location near the equator but away from the substellar point, (70° E, 10° N), see Figure 3.2. It was chosen as it is within the the equatorial jet. The Coriolis parameter $f = 2\Omega \sin \varphi$ is not large, so rotation is not included in the analysis. As discussed in Chapter 2, if the analysis is restricted to waves with a horizontal scale $L \lesssim U/\Omega$ where U is the characteristic mean flow speed and Ω is the planetary rotation rate (from Table 3.1) the effects of rotation can be neglected. Such a scale is adequate for all gravity waves considered here, but not for large-scale phenomena such as atmospheric tides (which have been considered by Gu and Ogilvie (2009)). For HD 209458 b, $L \sim 10^7$ m based on U in the hot extrasolar planet atmosphere simulations of Thrastarson and Cho (2010). All the waves considered in this chapter have horizontal wavelengths less than this, thus generalisations of the results presented in this chapter are applicable at other locations.

The temperature profile generally increases with height over the lowest four scale heights and then becomes isothermal. This provides a loose validation of the model in that the temperature profile is similar in structure to the temperature profile observed by the Galileo probe on Jupiter through the same pressure levels at a similar latitude (Seiff et al., 1998). The profile is extended by keeping the atmosphere isothermal through the planet's stratosphere and beginning the thermosphere at between 13 and 14 scale heights at $p_0 \approx 4 \times 10^{-6}$ bar. This profile, along with the mean flow profile described below, gives a Richardson number, Equation (2.56), of at least 3.4 throughout the domain. This value gives an attenuation of 1.4×10^{-5}. Hence, any critical layer can be considered to fully dissipate the wave.

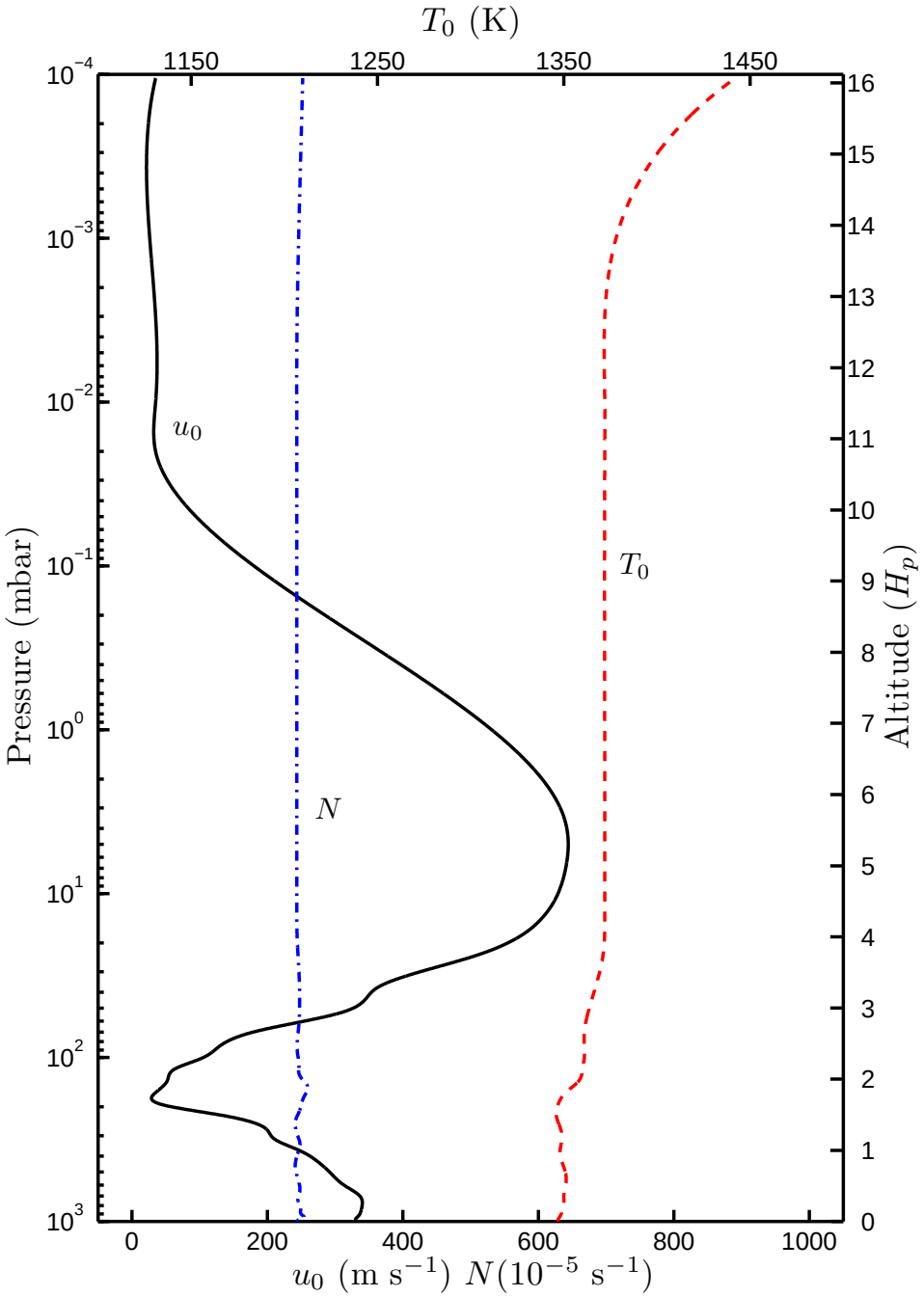

Figure 3.1 – The model flow and temperature profiles for HD 209458 b. Sample atmospheric mean flow u_0 (—), temperature T_0 (- - -) and Brunt–Väisälä frequency N (-·-) profiles of a typical hot extrasolar planet, HD 209458 b, used in this chapter. The profile is representative of a region at approximately 70°E, 10°N, see Figure 3.2. The profiles are obtained from a 3D global circulation model up to the ∼1 mbar level. Above that the profiles are simply extended. The temperature is loosely based on the observed structure of Jupiter (Seiff et al., 1998). The flow is smoothly brought back to a small value.

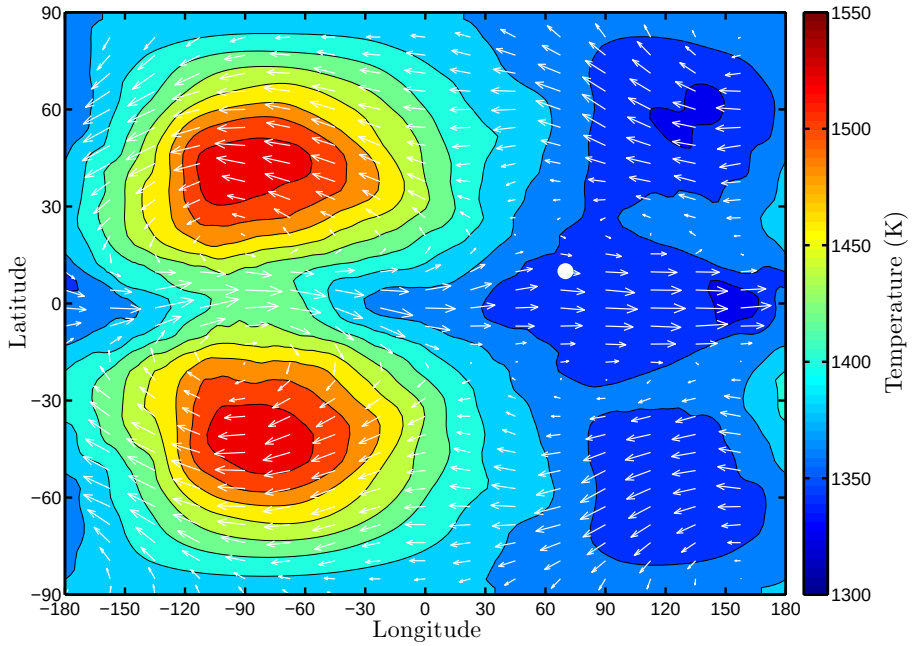

Figure 3.2 – Temperature map of HD 209458 b at 360 mbar. The modelled flow and temperature on HD 209458 b at about 1 scale height above the 1 bar level. The longest zonal flow vectors are 533 m s^{-1}. The sub-stellar point is at the centre (0°E,0°N). The site of the study, within the equatorial eastward jet, is indicated by the white dot.

The flow profile, also taken from Thrastarson and Cho (2010), has a minimum at $z/H_p \approx 2$ – i.e., $p \approx 200$ mbar. This is similar to the flow profile of Jupiter; see Chapter 4. It also has two local flow velocity maxima. The upper maximum is extended into a jet with a peak at $z/H_p \approx 6$ – i.e., $p \approx 1$ mbar. Although a peak has been observed in Jupiter's flow at this pressure level (Flasar et al., 2004) the jet in this profile is far deeper. Deep equatorial jets, covering over 3 decades of pressure, have been a feature of some simulations of EGPs (Showman et al., 2008, 2009). Above this jet the profile is extended to the top of the domain without shear. Note, this is the same assumption used for the lower boundary of the EGP thermospheric circulation model described in Koskinen et al. (2007). The structure of this flow profile is somewhat different to those of Showman et al. (2008, 2009), where there is just one jet with the peak flow located at $p \approx 10^2$ mbar level. The peak flow is also far greater in those studies at 4 or 5 km s^{-1}. It is important to note, however, that these differences do not change qualitatively the basic points made in this chapter.

The Brunt–Väisälä frequency profile $N(z)$ is also shown in figure 3.1. As can

be seen from Equation (2.8), we can write

$$N(z) = \left[\frac{g}{T}\left(\frac{\mathrm{d}T}{\mathrm{d}z} + \frac{g}{c_p}\right)\right]^{1/2} . \tag{3.1}$$

Since g and c_p are taken as (and are in actuality very close to) constants in the modelled height range, N depends only on the temperature profile $T(z)$. For isothermal regions, N is a constant. In general, the fractional change of T with height is small compared to $g/(Tc_p)$ throughout the modelled region. Hence, N is nearly constant in the entire domain with a value that is roughly 2.4×10^{-3} s^{-1}. The maximum value is just 1.2 times the minimum value. Therefore, N does not contribute much to the variation of the index of refraction m. The main contributor to the variation of m is the variation of the intrinsic phase, which is derived from the variation of flow speed. This should be compared to the analogous terrestrial situation, where the range of flow speeds is much lower. This allows N to have a larger effect on the variation of m on the Earth.

3.1.2 Forcing

As mentioned in Chapter 2, gravity waves can propagate in stratified atmospheres. EGPs are expected to have a stratified (radiative) layer in their atmospheres. Many mechanisms will readily generate gravity waves in such atmospheres. Mechanisms such as absorption of stellar radiation, convective release of latent heat, storms, flows over topography, coherent localized heat "islands" and convective overshoot, also impacts of asteroids and comets. Here we consider small- and meso-scale thermally-excited waves, the horizontal wavelengths of these waves are 2500 km or less. This is a reasonable range, since it is well within the observed range of gravity waves on Jupiter (Hickey, Walterscheid, and Schubert, 2000; Young et al., 1997). Although not unimportant we do not dwell on the precise nature of the source of the excitations. The main focus of these investigations is the propagation and deposition of momentum and energy.

The forcing used is simply represented as a Gaussian, modified so that it is zero beyond two half-widths above and below the centre, see Equation (2.49). The centre is located at $z/H_p = 1$ above the bottom of the domain. The

half-width is taken to be 75 km, or $\sim$0.15 H_p. The forcing location and width are chosen so that the vertical scale of the forcing is less than the vertical wavelength of the waves we present here. The effects of varying the location, width and strength of forcing has been explored. This case is presented to illustrate several important and general points. Not surprisingly, the dynamics do depend on the chosen parameter values, but the dependence is broadly predictable. For example, if the forcing scale is much larger than the vertical wavelength, the forcing is broad (see Section 2.3.2) and only a very small amplitude wave is emitted from the forcing region.

The peak heating rate, $\dot{Q}/c_p$, is set to 10^{-3} K s^{-1}. This is a modest value, corresponding to roughly 300 K per rotation of the planet. This is compared to $\sim$ 100 K per rotation at the chosen location in the circulation model of Thrastarson and Cho (2010). A forcing of $\sim$ 1000 K per rotation for a similar latitude, longitude and altitude location on the planet is used in Showman et al. (2008). The latter value implies that, in the absence of motion, that location on the planet will cool completely in one rotation of the planet. It is important to note that locally – i.e., at scales far below the grid scale of the current set of GCMs used to model hot EGP atmospheres – the forcing could actually be much stronger. The true value is, of course, presently uncertain and likely to be spatially and temporally variable over the planet. To provide a context, for the Earth the heating rate is $\sim$ 2 K per day (1 day = 0.29 rotations of HD 209458 b) over large areas; but, locally at the tops of low clouds on the Earth the rate can be up to $\sim$ 50 K per day (Wallace and Hobbs, 2006).

3.2 Wave-Background Interaction

In order to explore a range of wave-background interactions, the behaviour of gravity waves with a variety of horizontal phase speeds is considered.

3.2.1 Critical Layer Encounter

Figure 3.3 shows a gravity wave encountering a critical level in the upper jet of the model flow. The wave has a horizontal wavelength, $2\pi/k$, of 2500 km and $c = 600$ m s^{-1}. Here, since $c > u_0$ and the wave approaches the critical layer

from below, the momentum deposited in the mean flow causes the mean flow to accelerate. This acceleration peaks at over 250 m s^{-1} per rotation. This is large enough to double the flow speed at this layer in roughly two rotations – a significant effect. The effect is large enough to require its inclusion in any simulation of the atmospheric circulation (Cho, 2008).

The waves encountering critical levels are dissipated. Therefore, a flow with a range of flow speeds dissipates all gravity waves with phase speeds within this range. That is, a spectrum of gravity waves is prevented from propagating high into the atmosphere. There are other, secondary effects at the critical layer that may also effect the mean flow. However, they are not modelled here. For example, the deposition of energy into the flow at the critical layer may well lead to the generation of new gravity waves, which then may propagate further, partly mitigating the filtering effect.

3.2.2 Saturation

In general, it is possible that a wave may not encounter a critical level as it propagates upward. However, such a wave, as described in Section 2.5.2, will grow large and eventually break or suffer dissipation at higher altitudes. Although both momentum and energy are deposited in this case the focus here is on the effect on the temperature field. Figure 3.4 shows an example of a gravity wave saturating in the atmosphere of Figure 3.1.

The wave launched in Figure 3.4 has $c = -25$ m s^{-1} (i.e. westward). The horizontal wavelength remains at 2500 km, as in the critical layer example of Figure 3.3. The vertical velocity perturbation grows with height. Therefore, so does the zonal velocity perturbation $\tilde{u}$ and the potential temperature perturbation $\tilde{\theta}$, as expected from the polarisation relations, Equation (2.50). In this case the wave saturates near the top of the jet at the point where condition (2.54) is exactly satisfied. Condition (2.55) is satisfied since the magnitude of the zonal perturbation velocity and the intrinsic phase speed ($c_x - u_0$) are both approximately 122 m s^{-1}. The saturation deposits energy causing the atmosphere there to heat up. The heating is significant, peaking at $\sim$75 K per rotation—a 5% change in one orbit. In the absence of other effects, the ambient temperature can be doubled in about 20 planetary rotations.

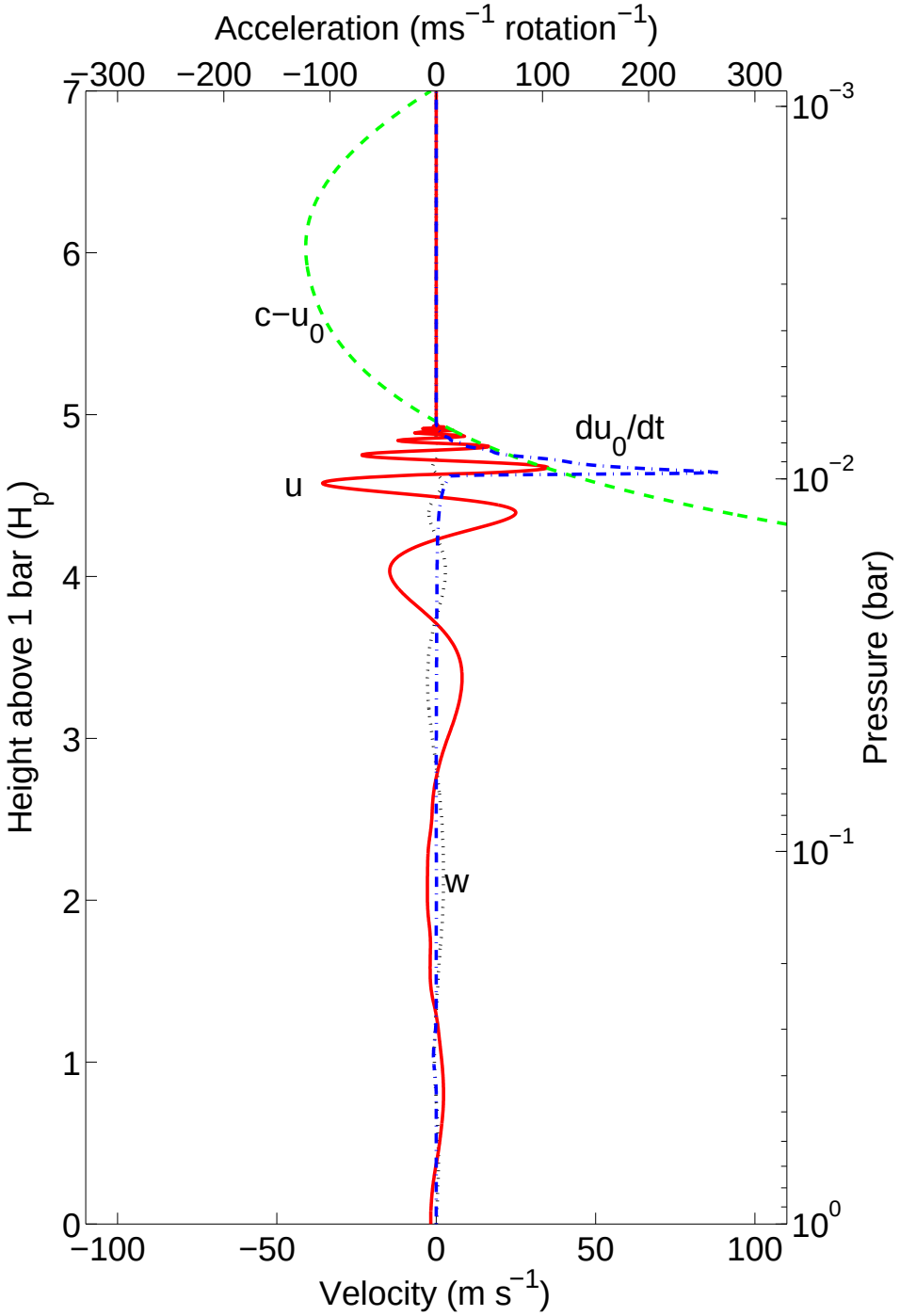

Figure 3.3 – A critical layer encounter. A gravity wave, with $c = 600$ m s^{-1}, propagating in an atmosphere with profiles shown in Figure 3.1. The horizontal perturbation velocity u (—), the vertical perturbation velocity w ($\cdots$), intrinsic phase speed $c-u_0$ (- - -), and the mean flow accelerations $\mathrm{d}u_0/\mathrm{d}t$ (-·-) are shown. The intrinsic phase speed becomes zero at $z/H_p \approx 5$ and the wave encounters a critical layer. In the layers just below the critical layer, the wave saturates and sheds momentum into the mean flow, causing it to accelerate, peaking at a rate of over 250 m s^{-1} rotation^{-1}.

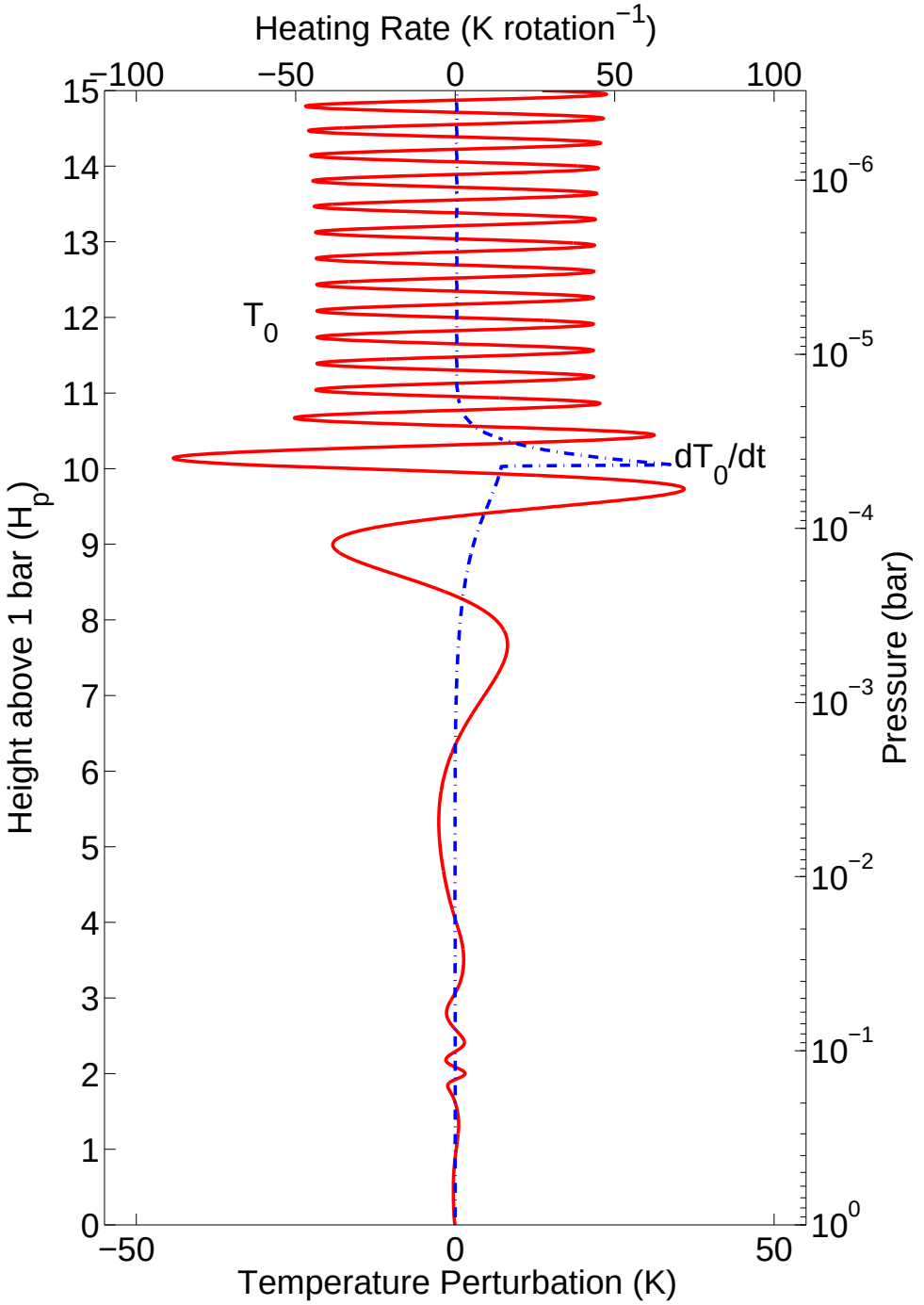

Figure 3.4 – Saturating Gravity Wave. A gravity wave, with $c = -30$ m s^{-1}, propagating in an atmosphere described by the profiles in Figure 3.1. The perturbation to the temperature field T (—) and the heating rate $\mathrm{d}T_0/\mathrm{d}t$ (-·-) are shown. The wave saturates at just above $z/H_p = 10$, where the heating peaks at about 70 K rotation^{-1}. The peak energy flux for this wave is approximately 1 W m^{-2}.

A wave that has a phase speed greater than the maximum flow speed will not encounter a critical layer. Those with phase speeds close to, but still above, the maximum flow speed will, in general, saturate in the region just below the maximum flow. This is because the intrinsic flow speed will be small in that region. Similarly, waves with phase speeds just less than the minimum flow will saturate as well. In this way the filtering effect discussed above is extended beyond those waves with phase speeds equal to flow speeds. The main effect of these filtered waves on the flow will be lower in the atmosphere. In the profile given in Figure 3.1, where the waves emanate from the $z/H_p = 1$ level, this means that the upper layers of the lower jet will be slowed by gravity waves whereas the lower levels of the upper jet will be accelerated.

Those waves that do not dissipate will be able to propagate into the upper atmosphere, causing momentum and heat to be deposited into the flow there when they dissipate. This can lead to very large changes to the flow. For example, the wave shown in Figure 3.4 causes a deceleration of up to 5 km s^{-1} per rotation as it saturates. This is clearly significant for the flow at this level.

A basic model of the structure of giant planets is that of a radiative (i.e., stably stratified) atmosphere overlaying a convective interior (Hubbard, Burrows, and Lunine, 2002). On Jupiter the boundary between these two layers lies just below the cloud layer, though regions of static stability have been found down to 20 bars in the data returned by the Galileo probe (Magalhães, Seiff, and Young, 2002). However, for hot EGPs, models predict that the boundary between the radiative and convective zones exists at much higher pressure levels, up to 1000 bar (Burrows, Budaj, and Hubeny, 2008). Thus gravity waves may be able to propagate from much deeper and denser regions on EGPs. Moving the location of the wave origin lower in the atmosphere does not change the basic behaviour in the qualitative sense. However, the amplitudes are much larger, compared with the case when the wave originates higher up in altitude. Thus, the possibility exists for stronger effects due to gravity wave interaction with the background.

This is illustrated in Figures 3.5 and 3.6, which should be compared with Figures 3.1 and 3.4. Here, the profiles have been extended downward. The wave is still launched at $z/H_\rho = 1$, but this is now deeper in the atmosphere. The wave has a phase speed of -40 m s^{-1}, and the horizontal wavelength remains at 2500 km. This wave also saturates near the top of the upper jet, where the

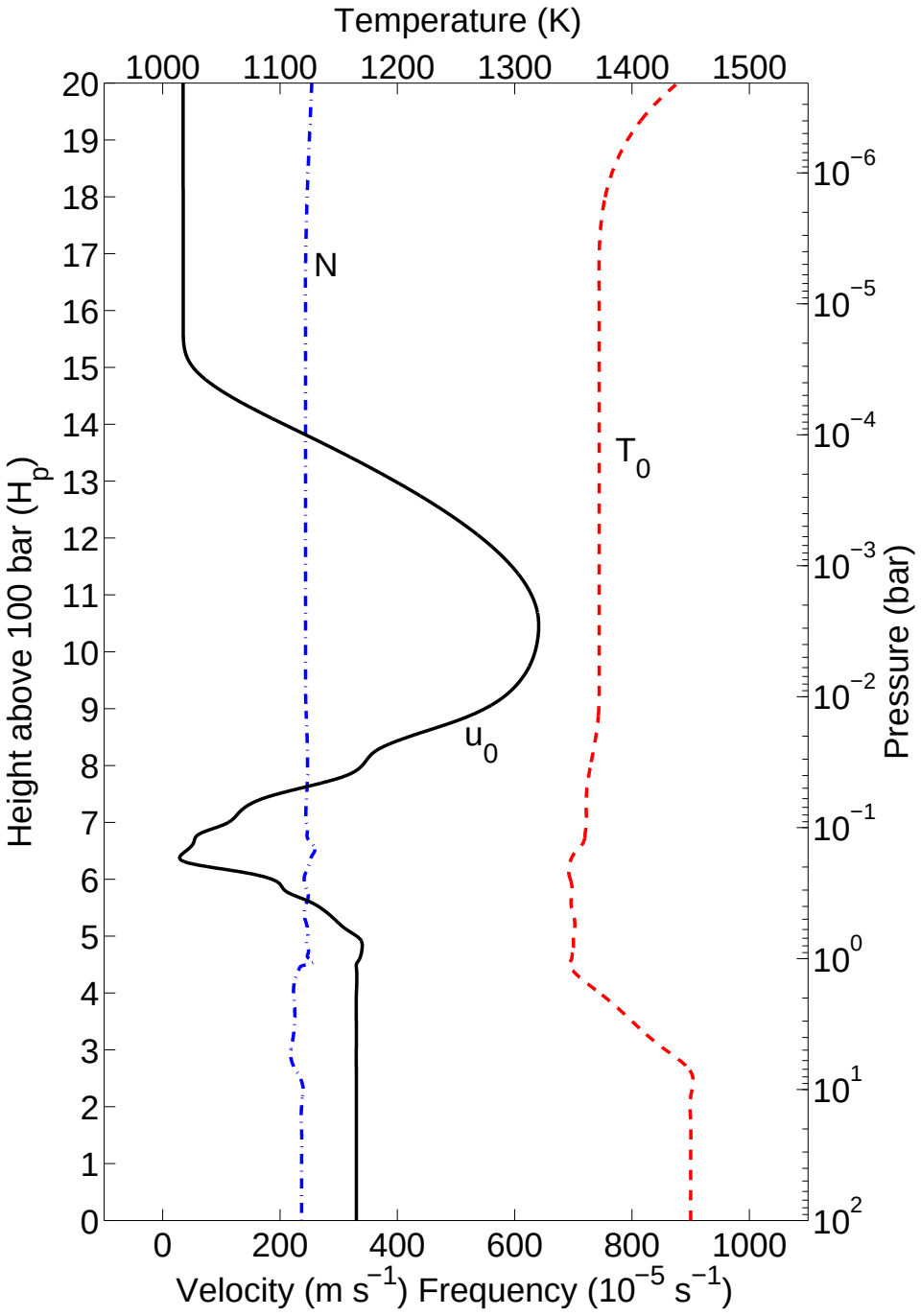

Figure 3.5 – Deeper model flow and temperature profiles for HD 209458 b. The same as in figure 3.1, but with the bottom of the domain extended down to 100 bars. Here u_0 (—) is extended downward barotropically (no height dependence) from the 1 bar level; the temperature T_0 (- - -) is extended downward so that the profile is similar to that of Figure 18 in Showman et al. (2009). The Brunt–Väisälä frequency N (-·-) is also shown.

energy deposition into the mean flow causes the atmosphere there to heat up. Note, in Figure 3.6 that the region of heating is lower than when the wave originates higher up. The heating is significant, peaking at ~ 3000 K per rotation. The ambient temperature can be doubled in approximately half a planetary rotation. In a more realistic scenario, dissipation – which is not included in the model – will likely reduce the heating rate somewhat. Nonetheless, it can be seen that gravity waves originating from deep within EGP atmospheres are capable of significant heating.

3.2.3 Refraction

So far this chapter has focussed on the vertical transport of momentum and energy by gravity waves. However, the waves can also transport momentum and energy horizontally. Substituting $c = \omega/k$ into the expression for the index of refraction, taken from Equation (2.41), and rearranging gives the dispersion relation for anelastic gravity waves. This is shown at Equation (3.7). Here, the case where $u_0 = 0$ is considered. Cases where $u_0 \neq 0$ are examined in the sections following this one.

When there is no background mean flow, the dispersion relation simplifies to

$$\omega = \pm \frac{Nk}{\left[k^2 + m^2 + \left(1 - 2H_\rho'\right) / \left(4H_\rho^2\right)\right]^{1/2}} \,. \tag{3.2}$$

Then using the definitions

$$u_g = \frac{\partial \omega}{\partial k} \tag{3.3a}$$

$$w_g = \frac{\partial \omega}{\partial m} \tag{3.3b}$$

to obtain the group velocities gives

$$u_g = \pm \frac{N\left[m^2 + \left(1 - 2H_\rho'\right) / \left(4H_\rho^2\right)\right]}{\left[k^2 + m^2 + \left(1 - 2H_\rho'\right) / \left(4H_\rho^2\right)\right]^{3/2}} \tag{3.4a}$$

$$w_g = \pm \frac{Nkm}{\left[k^2 + m^2 + \left(1 - 2H_\rho'\right) / \left(4H_\rho^2\right)\right]^{3/2}} \tag{3.4b}$$

Thus, for propagating waves (i.e., waves for which m is real – recall that

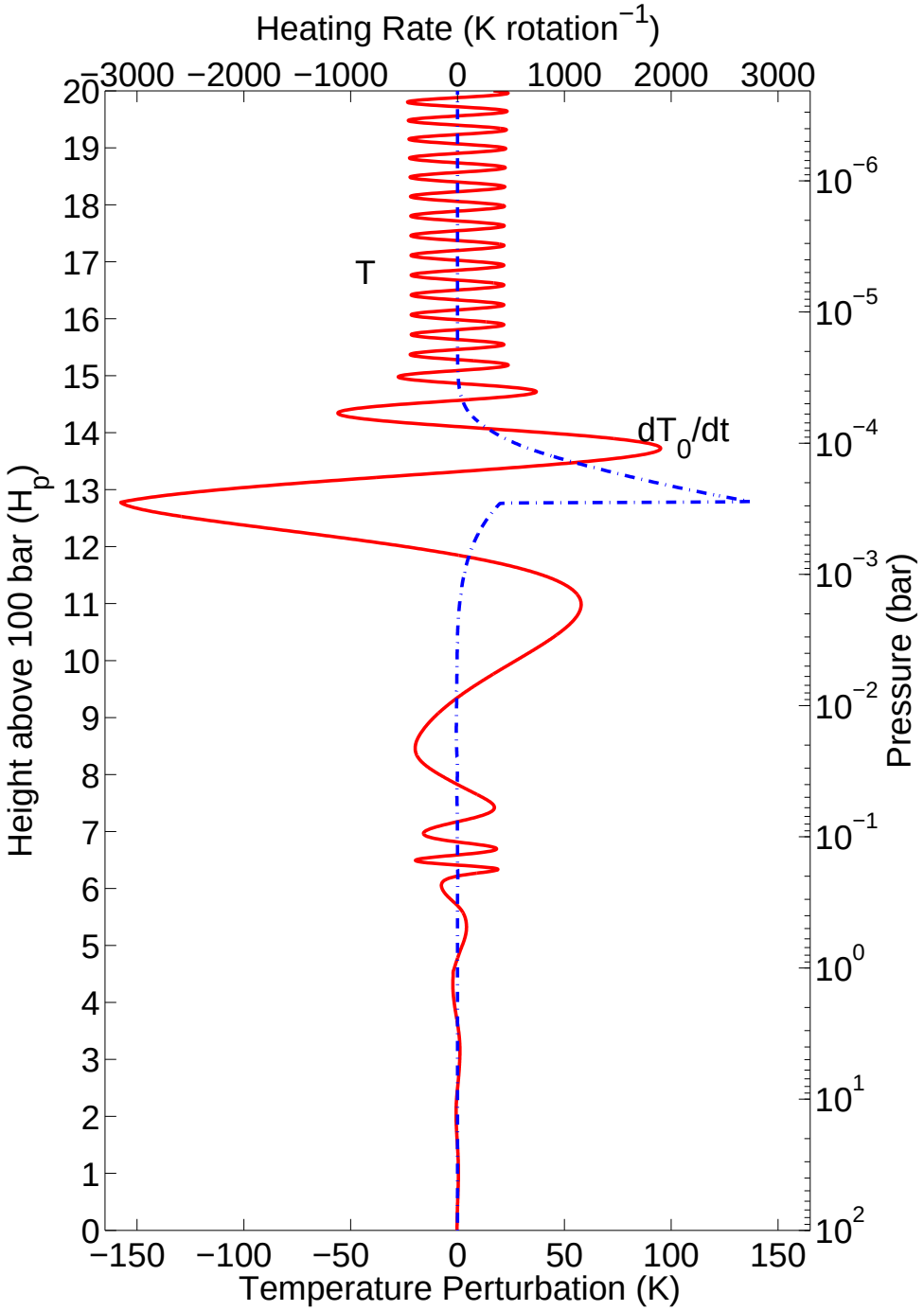

Figure 3.6 – A gravity wave, with $c = -30$ m s^{-1}, propagating in an atmosphere described by the profiles in Figure 3.5. The perturbation to the temperature field T (—) and the heating rate $\mathrm{d}T_0/\mathrm{d}t$ (-·-) are shown. the wave saturates at just above $z/H_p = 13$, where the heating rate peaks at about 2700 K per rotation. In terms of the pressure level, this location is actually lower than in the case shown in Figure 3.4, and the magnitude of the peak is nearly 50 times greater. The peak energy flux for this wave is nearly 200 W m^{-2}. Thus, it can be seen that having a source deeper in the planet can have a much greater effect.

when m is imaginary the TGE has evanescent solutions) $u_g \neq 0$. Therefore, gravity waves always propagate obliquely in the atmosphere considered here and cannot propagate purely vertically when there is no background flow.

From equation (3.4) we see that β, the angle of energy propagation with respect to the horizontal, is given by

$$\tan\beta = \frac{km}{m^2 + \left(1 - 2H_\rho'\right) / \left(4H_\rho^2\right)} \,. \tag{3.5}$$

Since H_ρ is, in general, large (in the profile we are considering it is just under 500 km) and nearly constant $\tan\beta$ varies with $1/m$. Thus, variation in m gives rise to changes in the direction of propagation (i.e., refraction), and explains why m is called the index of refraction. As a wave propagates into a region of higher m the energy propagates more horizontally. Note that, as we are here considering a region with no flow, increasing m is essentially equivalent to increasing N. In general N increases in the lower thermosphere of giant (and other) planets as is indicated in Figure 3.1 so the direction of energy propagation in this region will bend toward the horizontal even though the flow is small. Thus, waves that are not filtered, as described above, and reach the thermosphere may well propagate horizontally far from their point of origin. Any effects caused by such waves when they eventually dissipate would impact the atmosphere away from the point of origin of the wave.

3.2.4 Trapped Waves

From Equation (2.43) we can see that in regions where m is imaginary the wave is evanescent: its amplitude decays toward zero in the vertical and therefore it does not propagate vertically. As discussed in Chapter 2, this can occur when $N^2 < 0$ (i.e., when the atmosphere is convectively unstable). However, as can be seen in Figures 3.1 and 3.5 in this study we have $N^2 > 0$ throughout the domain. But, for non-hydrostatic waves the non-hydrostatic term can dominate the buoyancy, shear and curvature terms leading to a region where the wave is evanescent even though the atmosphere is stably stratified.

In addition, when the index of refraction changes between layers, the wave is reflected at the boundary. The amount of reflection is given by the magnitude

of the coefficient of reflection $|r|$, where

$$r = \frac{m_1 - m_2}{m_1 + m_2}\,. \tag{3.6}$$

Here, m_1 and m_2 are the indices of refraction in the two adjacent layers. When m_2 is imaginary, total reflection occurs and the wave is evanescent in that region; its amplitude decays to zero. However, a region of propagation can exist between two regions of evanescence. This readily occurs for jets, where the intrinsic phase speed varies enough to allow the hydrostatic term to dominate in some regions and not in others. Such a region can also occur through variations of the Brunt–Väisälä frequency, though that is not the case in the atmosphere considered in this chapter. In Figure 3.7, we see a wave that is trapped in the relatively quiescent region between $z/H_\rho \approx 1$ and $z/H_\rho \approx 4$. Outside this region, the value of $\Re(m)$ is small or zero. Trapped in this region the wave is able to interact with itself and, under appropriate conditions, resonate.

This is another mechanism via which waves may be filtered out by the flow, and so not reach higher altitudes at which saturation can occur. However, in this case, a trapped wave does not directly interact with a low altitude flow that changes its characteristics. Indeed, between two reflection layers the wave can propagate horizontally – even in the absence of any flow – using the refractive mechanism described above. As long as the layers do not allow much leakage, it is possible for a trapped wave to cover large horizontal distances – transporting momentum and heat zonally.

3.2.5 Ducting

As well as being trapped in relatively quiescent regions, it is possible for waves to be trapped in a jet. As alluded to above, it is possible for such a wave to travel within the region of trapping which is known as a duct or waveguide. In Figure 3.8 a non-hydrostatic wave is trapped within the jet (located at the ~ 5 mbar level) in the model atmosphere (Figure 3.1). Note the small values of $\Re(m)$ outside the jet.

In this case, the flows are significant. Therefore, we use the full dispersion

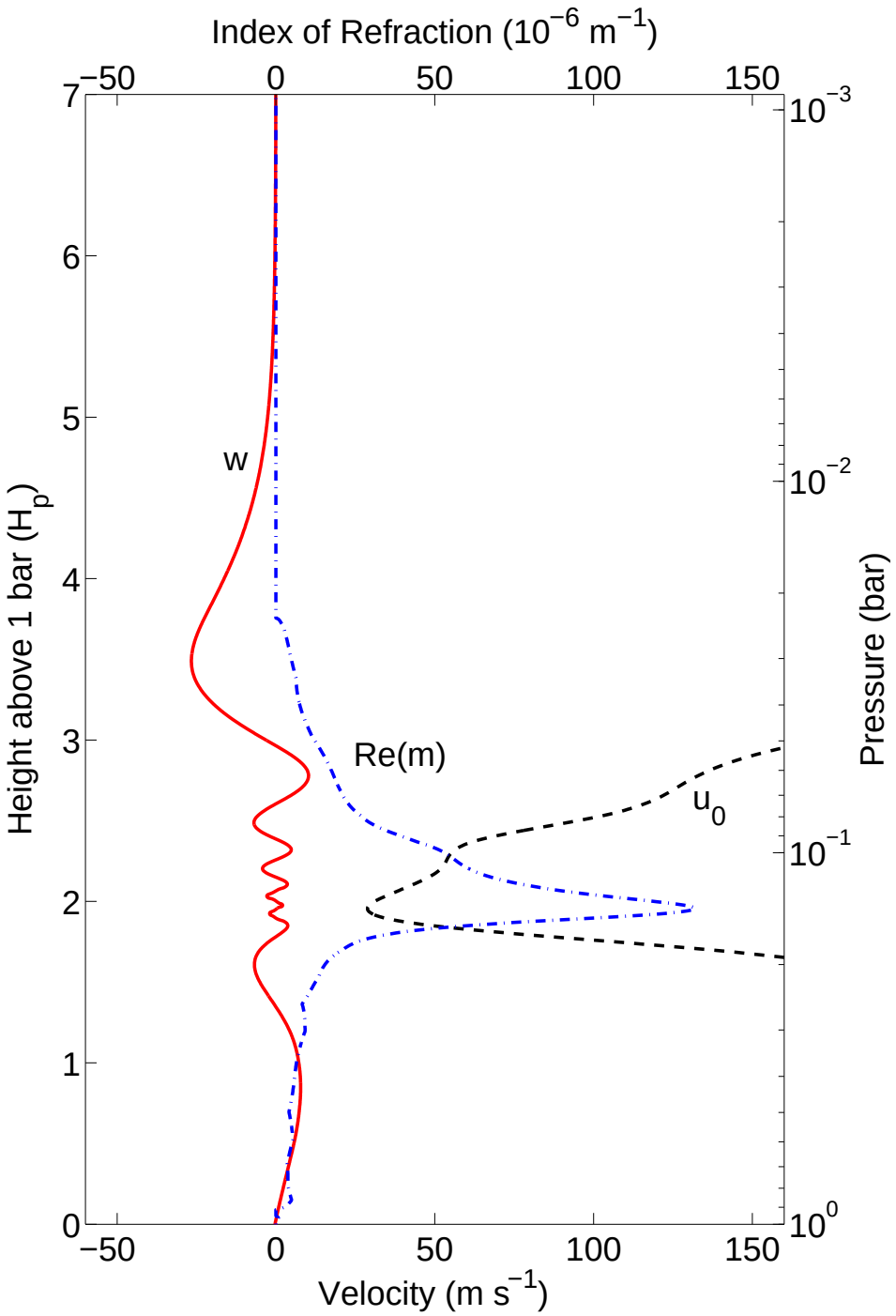

Figure 3.7 – A trapped gravity wave, with $c = 10$ m s^{-1} and horizontal wavelength $2\pi/k = 955$ km, trapped in an atmosphere with the structure presented in Figure 3.1. The vertical velocity perturbation w (—), mean flow u_0 (- - -), and the real part of the index of refraction m (- · -) are shown. The wave is trapped in the relatively quiescent region between $z/H_p \approx 1.5$ and $z/H_p \approx 3.5$ and does not propagate vertically. The region of trapping corresponds to the region where m is real. The wave is reflected at the boundaries of this region, providing a possibility for resonance

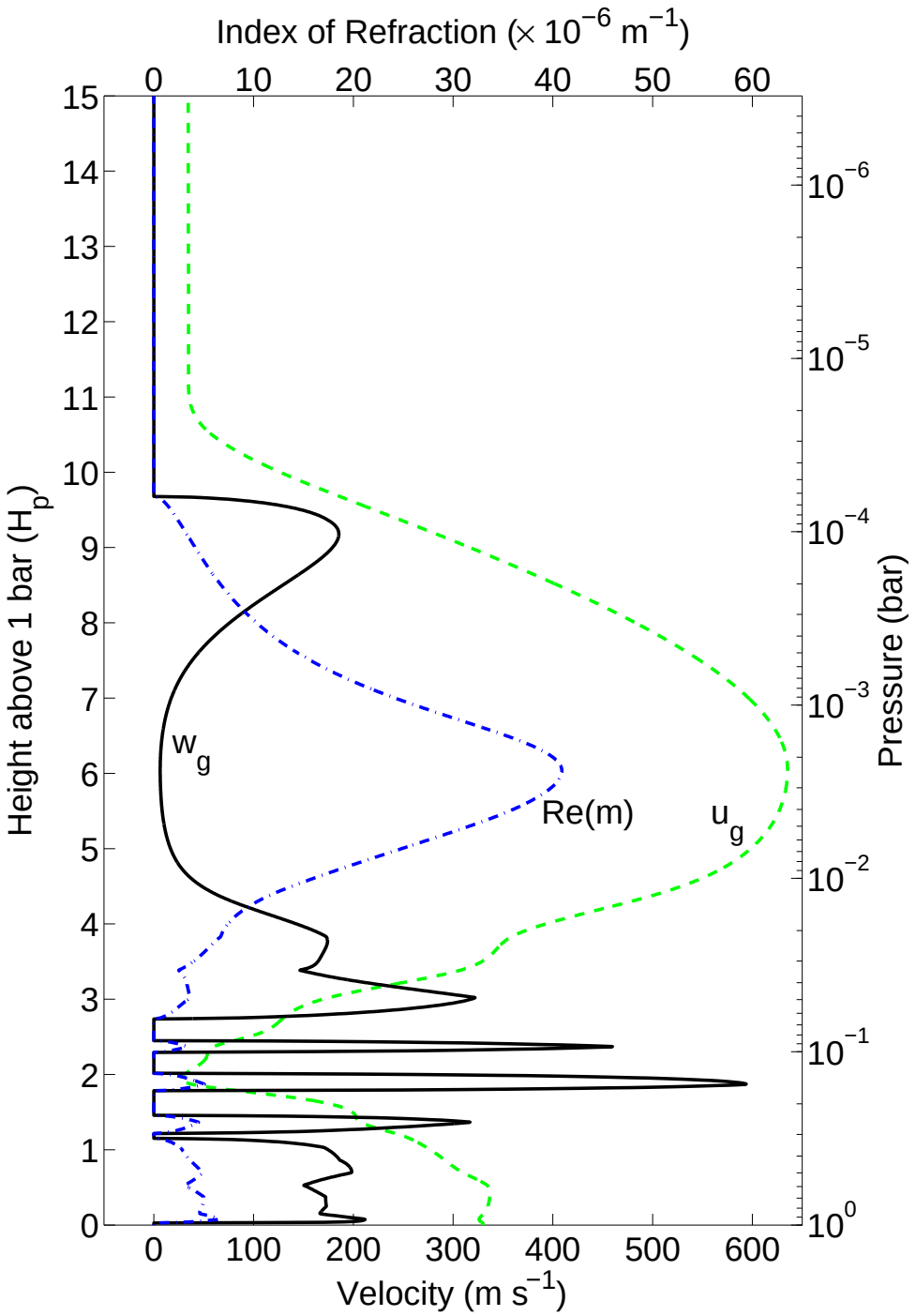

Figure 3.8 – This is the same as in Figure 3.7, but with $c = 700$ m s^{-1} and horizontal wavelength $2\pi/k = 1410$ km. The horizontal group speed u_g (- - -), vertical group speed w_g (—), and the real part of the index of refraction m (-·-) are shown. The wave (not shown) is trapped in the upper jet between $z/H_p \approx 3$ and $z/H_p \approx 9$, the region where m is real, and does not propagate vertically above this region; it is however, able to propagate along the jet as the large value of u_g within the jet shows. The wave is reflected at the boundaries of this region, providing a possibility for resonance.

relation,

$$\begin{aligned}\omega &= ku_0 + \frac{k\left(u_0' + H_\rho u_0''\right)}{2H_\rho\left(k^2+m^2+\left(1-2H_\rho'\right)/4H_\rho^2\right)} \\ &\quad \pm\frac{Nk\left[\left(k^2+m^2+\left(1-2H_\rho'\right)/4H_\rho^2\right)+\left(u_0'+H_\rho u_0''\right)^2/4N^2H_\rho^2\right]^{1/2}}{\left(k^2+m^2+\left(1-2H_\rho'\right)/4H_\rho^2\right)},\end{aligned} \tag{3.7}$$

to develop expressions for the group velocities. Unfortunately, the expressions obtained are rather large and unilluminating, obscuring the situation. However, the expressions can be simplified by assuming that $u_0^{'}$ and $u_0^{''}$ are small, which is a realistic assumption, as the shear is of the order of 10^{-3} s^{-1} and $u_0^{''}$ is of the order 10^{-8} m^{-1} s^{-1} in the model atmosphere. This is small compared with the other terms in the expressions. This then gives

$$u_g = u_0 \pm \frac{N\left[m^2+\left(1-2H_\rho'\right)/\left(4H_\rho^2\right)\right]}{\left[k^2+m^2+\left(1-2H_\rho'\right)/\left(4H_\rho^2\right)\right]^{3/2}} \tag{3.8a}$$

$$w_g = \pm\frac{Nkm}{\left[k^2+m^2+\left(1-2H_\rho'\right)/\left(4H_\rho^2\right)\right]^{3/2}} \tag{3.8b}$$

From these expressions, we can see that, group speeds in this case are the same as in the steady case in the frame moving with the flow, u_0. Therefore, in the model atmosphere, u_g follows u_0, as this is the larger term on the right-hand side of Equation (3.8a). In Figure 3.8, the values of u_g and w_g are shown. Note that in the centre of the duct w_g is very small and u_g is large, so that energy is transported along the flow. At the top and bottom of the duct the vertical group velocity increases, while the horizontal group velocity falls. Therefore, propagation here is more vertical. In Figure 3.8, w_g is shown as positive; however, this is only for upward propagation of energy, at the top of the duct the wave is reflected and the vertical component becomes negative. This keeps the wave within the jet. The ray path followed by the wave is shown in Figure 3.9.

The wave can travel large distances in this duct; but, eventually, the wave will either escape the duct or be dissipated. For example, it may be that the range of speeds in the duct changes so that a critical layer for the wave is created. The wave will then be re-absorbed into the flow. Alternatively, if the

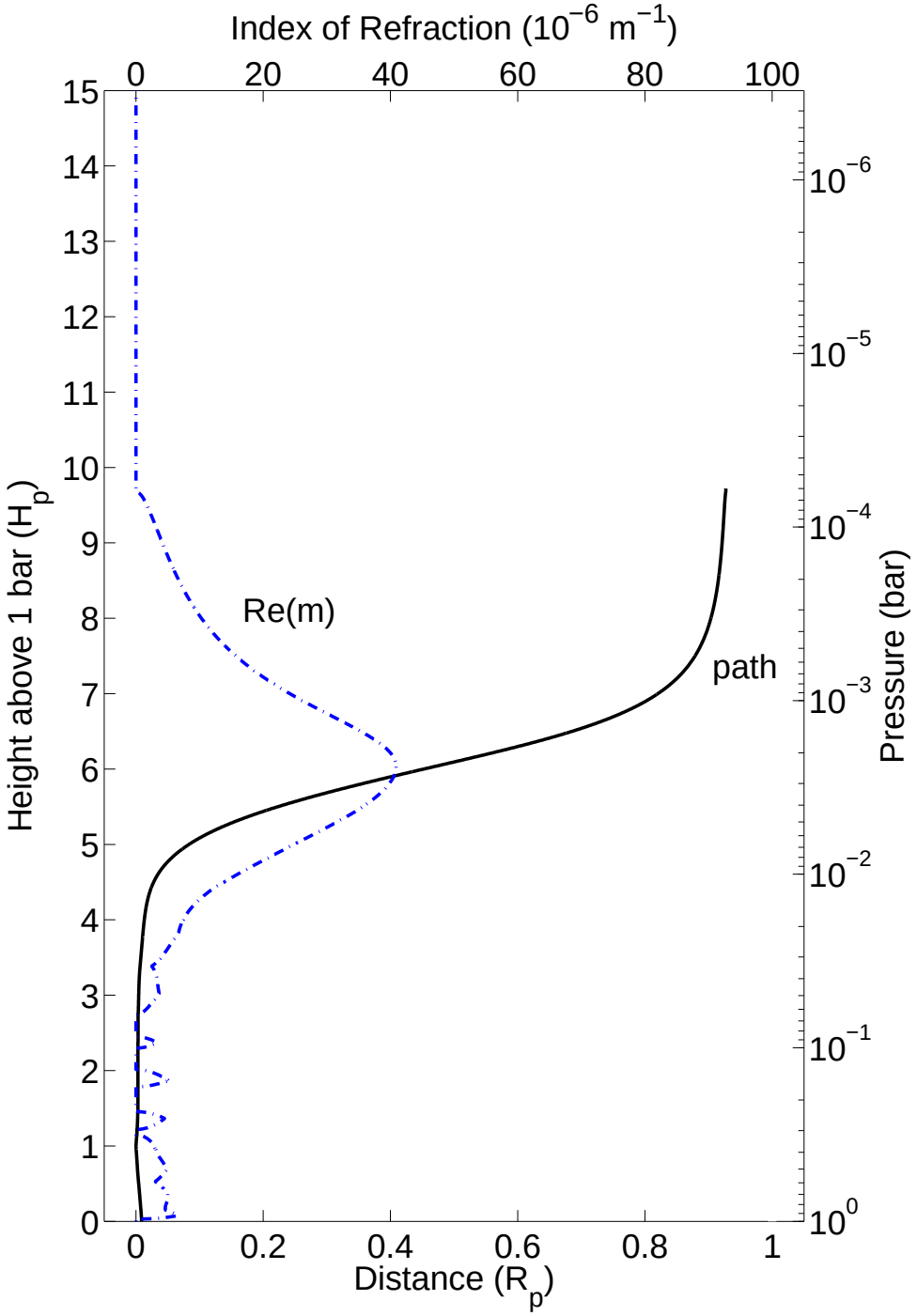

Figure 3.9 – The path of propagation of the wave in Figure 3.8 assuming that the properties of the duct do not change in the x-direction. The path shown is the first crossing of the duct. At this point the wave will reflect and then propagate downward in a mirror image of this path. Note that the wave travels nearly one planetary radius before reflection. This means with six reflections the wave will have nearly circumnavigated the planet. Of course in the real situation the properties of the duct will change and the wave will probably either leak out of the duct or dissipate before the circumnavigation is complete.

flow or Brunt–Väisälä frequency outside the jet changes so that the buoyancy term is no longer small and dominated by the non-hydrostatic term, then the reflection is no longer total and the wave will leak out of the duct. This can happen, for example, when the wave propagates into a colder region. As can be seen from Equation (3.1), a fall in temperature with a constant lapse rate will cause an increase in the Brunt–Väisälä frequency and thus an increase in the buoyancy term. This may occur very far from the original region of wave excitation. Indeed, in the example given, it is possible to envisage jets ducting waves and so transporting energy from the day-side of a tidally locked planet to the colder night-side where the waves escape the jet and propagate away from the duct before dissipating. This would make a contribution to homogenising the temperature of such a planet.

3.3 Implication for Circulation Models

The effects of gravity waves discussed in this chapter on the larger scale circulation must be parametrised in global models because the spatial resolution – both horizontal and vertical – required to model them is currently prohibitive. The waves important to the large-scale extrasolar planet atmospheric circulation have horizontal length scales ranging from approximately $\sim 10^5$ m to $\sim 10^7$ m and vertical wavelengths as small as 10^4 m. Waves with periods of a few hours can carry significant momentum and energy fluxes vertically, but the sources of these waves include processes that are not included or resolvable in current circulation models.

The difficulty with representing gravity waves in GCMs exists even for GCMs of the Earth. For example, the parametrisation for convection is not aimed at producing realistic gravity waves (Collins et al., 2004). However, not representing gravity waves can affect the accuracy of the GCMs. The lack of gravity wave drag can lead to the over-estimation of wind speeds, resulting in faster and narrower jets than observed (McLandress, 1998). Further, the waves close off the jets in the mesosphere (Hamilton, 1996). Also, gravity waves introduce turbulence with subsequent mixing and thermal transport (Fritts and Alexander, 2003). This leads to greater homogenisation of the atmosphere with a reduction in, for example, temperature gradients. Gravity waves also inter-

act with planetary waves, playing a role in important transient phenomena, such as sudden stratospheric warming. In the absence of gravity waves these phenomena are not accurately modelled (Richter, Sassi, and Garcia, 2010).

There are many parametrisation schemes currently incorporated or proposed for general circulation modelling (McLandress, 1998; Nappo, 2002). In all of the schemes, the basic components are (1) specification of the characteristics of the waves at the source level, (2) wave propagation and evolution as a function of altitude and (3) effects on and by the atmosphere. All of them are essentially linear and one-dimensional, in that waves only propagate vertically and that only vertical variation in the background influences the propagation. As seen in this chapter, linear theory still requires information such as the wave's horizontal phase speed c and wavenumber k. A more complete theory would need spatial and temporal spectral information. This is especially important on EGPs, where the sources of gravity waves move and change over short timescales, in contrast to the Earth where topography is a major generator of gravity waves. Also, on spin-orbit synchronised planets parametrisations that treat propagation as purely vertical would be inadequate as they would not take into account the zonal inhomegeneity of such planets. Intermittency is another crucial feature that would need to be taken into account. The primary differences in various schemes pertain to the treatment of non-linearity and specificity of wave dissipation mechanisms.

Currently, all global circulation models of hot-Jupiters suggest the presence of a low number of zonal jets (e.g Cho et al., 2008; Rauscher and Menou, 2010; Showman et al., 2008, 2009; Thrastarson and Cho, 2010). However, all the models do not have the resolution required to adequately resolve gravity waves and are subject to all of the limitations described above. This issue has been previously raised by Cho (2008), in which they advocate caution against quantitative interpretation of current model results. For example, without the inclusion of the wave effects discussed in this work, high speed jets and precise eastward shift of putative "hot spots" can be questioned (e.g. Knutson et al., 2007; Langton and Laughlin, 2007).

3.4 Viscosity and Thermal Diffusivity

The dissipation of the gravity waves considered so far has been either through encounters with critical layers or via wave saturation. The fluid itself has been taken to be non-dissipative. This is reasonable where eddy diffusivity dominates. However, this will not be the case throughout the whole atmosphere. All fluids have some viscosity due to the molecular properties of the fluid. This can be simply observed by the relative ease one travels through air compared to water. However, even in a relatively homogeneous fluid the viscosity will vary with density. Therefore, as a gravity wave propagates upwards and the density of the atmosphere, through which it travels, falls, it will eventually, barring dissipation from other mechanisms, encounter a region where viscosity comes to dominate. The modelling of the wave propagation in this region needs to take this into account.

In this section gravity wave propagation in the upper atmosphere of extrasolar planets, where viscosity is significant will be considered. Sample calculations show the location of these regions on a typical close-in giant planet. It considers how the waves propagate through such tenuous regions and the effects that wave dissipation has on the background. These effects are discussed and contrasted to those in Section 3.2, where dissipation was not treated as significant in general.

3.4.1 Background Structure and Viscosity

The mechanisms by which gravity waves interact with the background that have been considered, such as saturation and critical layers, depend on the mean flow having shear, that is changing with height. Even refraction, trapping and ducting depended upon the vertical wind shear. Here, where dissipation via viscosity is considered, wind shear is not included in order that its effects do not obscure the role of viscosity. This is done by treating the background flow as uniform in the z direction. The vertical profiles of temperature and zonal wind are shown in Figure 3.10. Whilst the background flow is taken as constant, the profiles for the temperature (and therefore the *Brunt–Väisälä* frequency which is not shown) are the same as that used in the non-viscous discussion above. Other relevant parameters are the same as those given in

Parameter	Value
μ_{H_2}	2.0715×10^{-7}
β_{H_2}	0.716
μ_{He}	4.3338×10^{-7}
β_{He}	0.670

Table 3.2 – Viscosity Calculation Parameters The units of $\mu_{H_2} T^{\beta_{H_2}}$ and $\mu_{He} T^{\beta_{He}}$ are kg m^{-1} s^{-1} where T is the temperature in K.

Table 3.1.

Viscosity

In addition to the temperature and flow, in order to model the situation, the vertical profile of viscosity $\mu(z)$ is required. The dynamic viscosity of a fluid depends upon its composition and the physical properties of the fluid – specifically the density, mean free path and mean molecular velocity. As the gas becomes more tenuous its density falls, but the mean free path increases. Hence, these effects have little impact; overall the viscosity changes little. The viscosity profile is produced using the model from the Jovian Ionospheric Model (Achilleos et al., 1998),

$$\mu = a_{H_2} \mu_{H_2} T^{\beta_{H_2}} + a_{He} \mu_{He} T^{\beta_{He}} , \tag{3.9}$$

where a_{H_2} and a_{He} are the number fractions of molecular Hydrogen and Helium, respectively. The parameters, μ_{H_2}, β_{H_2}, μ_{He} and β_{He}, are given in Table 3.2. This model has previously been used to model the atmospheres of extrasolar giant planets (Koskinen et al., 2007). We take $a_{H_2} = 0.83$ and $a_{He} = 0.17$ which corresponds to the specific gas constant $R = 3523$ given in Table 3.1. The resulting viscosity profile is shown in Figure 3.10. As can be seen the dynamic viscosity varies little with height – as expected.

However, it is the kinematic viscosity, $\nu = \mu/\rho$, which controls the size of the damping induced by the viscosity. As the density falls exponentially with altitude, the kinematic viscosity becomes large as shown in Figure 3.11. The effect of viscosity on the flow is included via the momentum equation.

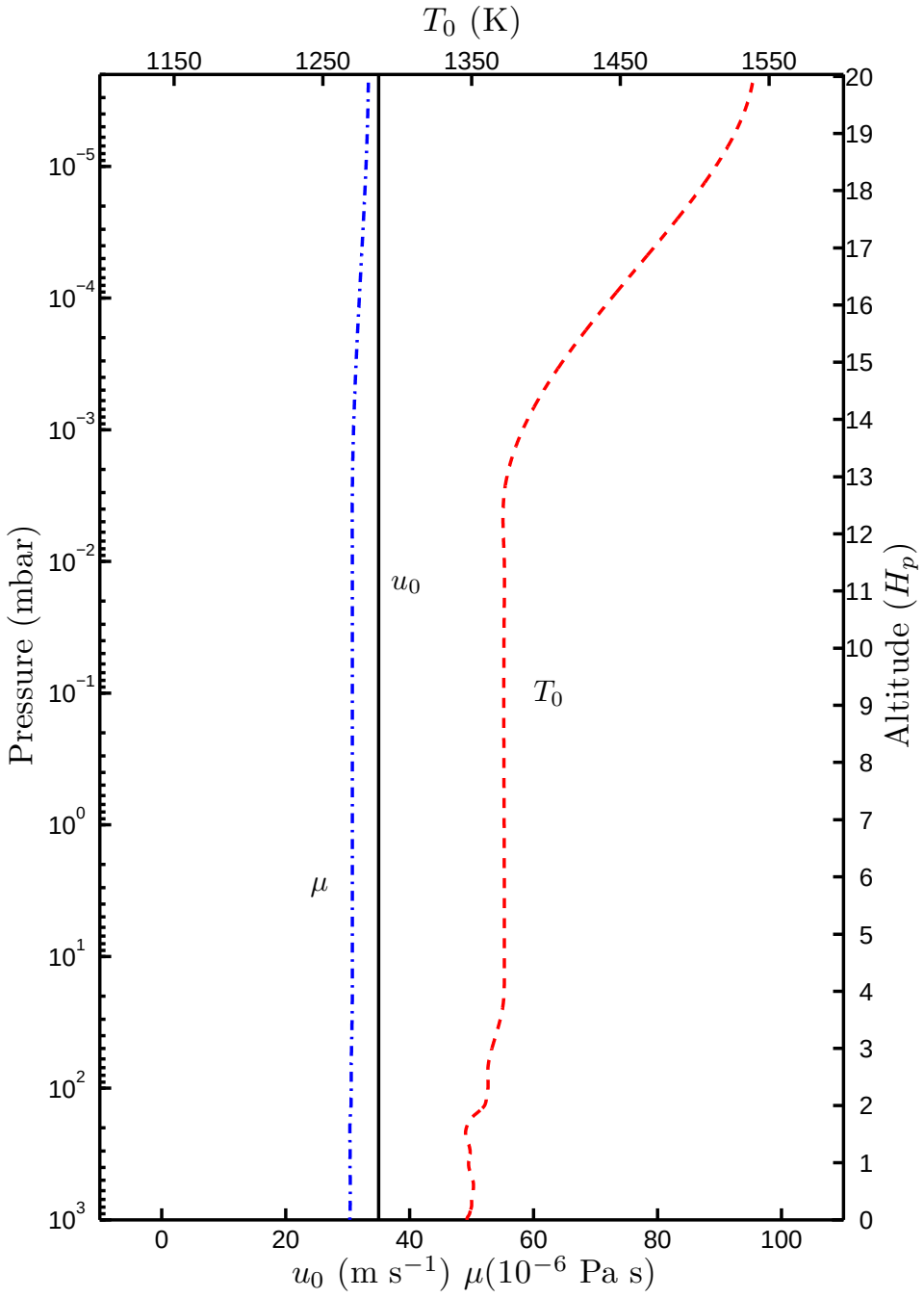

Figure 3.10 – Example atmospheric temperature T_0 (- - -), mean flow u_0 (—) and dynamic viscosity μ (-·-) profiles used in this section. As can be seen the dynamic viscosity varies little with height, the flow is taken as constant so that the effects of wind shear, discussed previously, do not obscure the effects of dissipation.

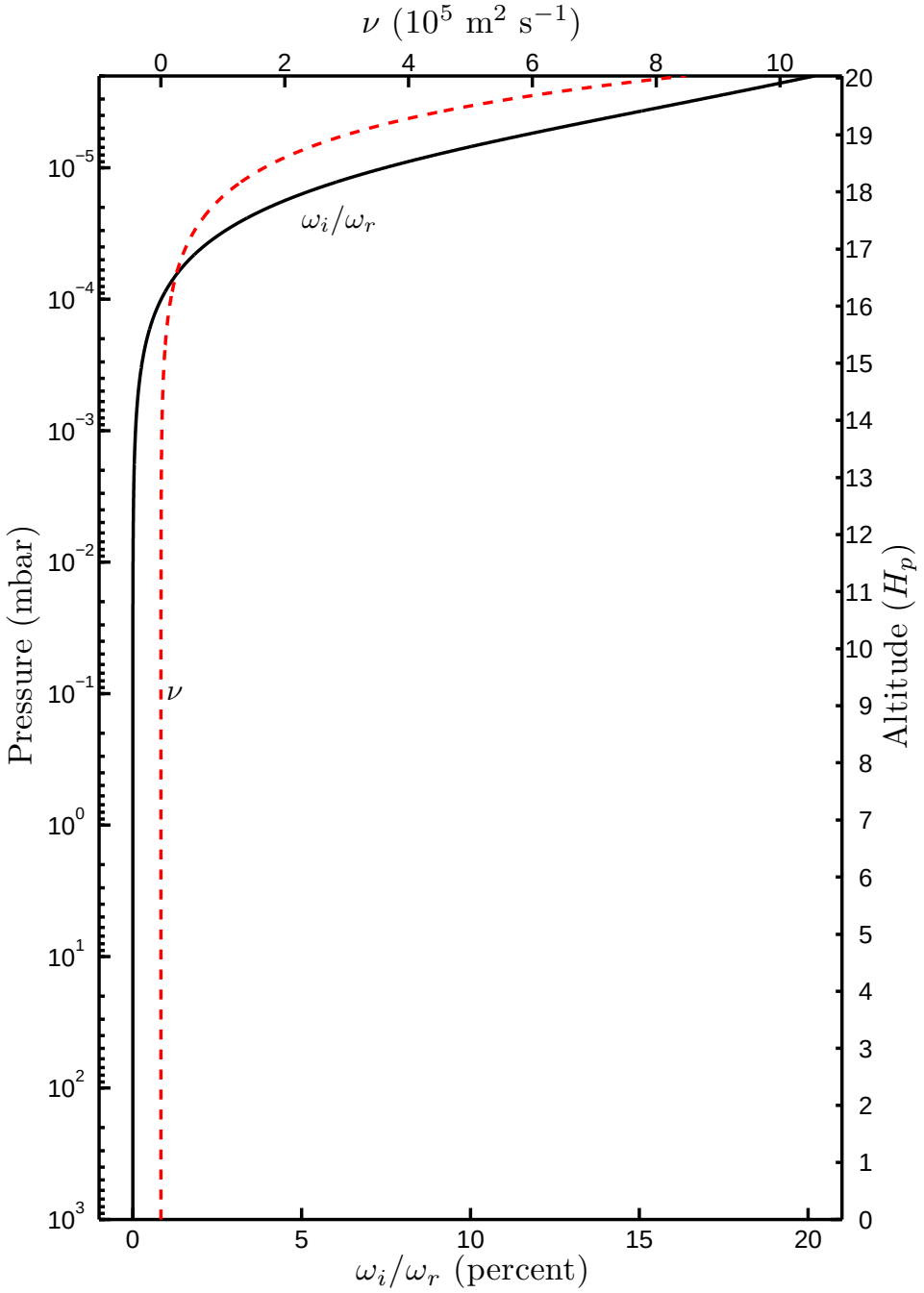

Figure 3.11 – The variation of kinematic viscosity, $\nu = \mu/\rho_0$, with height. As can be seen the kinematic viscosity remains small throughout the region of the atmosphere considered previously. The level of dissipation is indicated by the ratio of the imaginary to real parts of the intrinsic frequency of the wave. This ratio can be seen to grow from around $\sim 15\ H_p$. The effects of dissipation will begin to be noticeable at this level.

Thermal Diffusivity

As well as viscosity acting to damp the wave, through the removal of momentum, the removal of heat also acts to dissipate the wave. Heat diffuses more rapidly through materials with larger thermal diffusivity thus damping thermal perturbations more quickly. This effect is included via the energy equation. The thermal diffusivity is modelled using the Prandtl number P_r, which is the ratio of kinematic viscosity to thermal diffusivity. In principle, if the profiles of kinematic viscosity and Prandtl number are known then the thermal diffusivity profile is known. Although Prandtl numbers for Hydrogen/Helium mixtures are not available at the temperatures and pressures appropriate for the upper region of the model atmosphere Prandtl numbers for the similar region on Jupiter lie in the range 0.68-0.71 (Matcheva and Strobel, 1999). In this study the Prandtl number is taken as constant at 0.7. Variation of the number from 0.5 to 1 has been found not to qualitatively vary the findings of this section.

3.4.2 The Anelastic Equations with Dissipation

To illustrate how dissipation affects gravity waves in a typical exoplanet atmosphere we consider waves with wavelengths of 2500 km with phase speed of ± 135 m s^{-1}. For such waves $c^2k^2 < N^2$ and they can be treated as hydrostatic. Further, as discussed above in Section 2.4.1, the magnitude of the zonal flow perturbation is larger than the vertical flow perturbation so the viscosity is included in the zonal momentum equation. Also, as $m > k$ the derivatives in the vertical are larger than those in the horizontal and so dissipation is taken using the vertical derivatives of temperature and velocity. The energy equation, Equation (2.20c), can be written as (e.g., Nappo, 2002),

$$c_v \frac{\mathrm{D}T}{\mathrm{D}t} + RT\nabla \cdot \mathbf{u} = 0\,, \tag{3.10}$$

thus allowing the linearised anelastic equations, with disspation, to be written in terms of T as

$$\frac{\mathrm{D}u_1}{\mathrm{D}t} + \frac{\partial \Phi_1}{\partial x} = \frac{1}{\rho_0}\frac{\partial}{\partial z}\mu\frac{\partial u_1}{\partial z}\,, \tag{3.11a}$$

$$\frac{\partial \Phi_1}{\partial z} - g\frac{T_1}{T_0} = 0\,, \tag{3.11b}$$

$$\frac{\partial u_1}{\partial x} + \frac{\partial w_1}{\partial z} - \frac{w_1}{H_\rho} = 0\,, \tag{3.11c}$$

$$\frac{\mathrm{D}T_1}{\mathrm{D}t} + \frac{T_0 N^2}{g} w_1 = \frac{1}{\rho_0 P_r}\frac{\partial}{\partial z}\mu\frac{\partial T_1}{\partial z}\,, \tag{3.11d}$$

where μ is the molecular viscosity and P_r is the Prandtl number. Then, assuming wave-like perturbations, of the form in Equation (2.30), for all varaibles including T_1, allows the use of the substitutions given in Equation (2.31). Further, the observation that the dynamic viscosity changes slowly (see discussion in Section 3.4.1) gives the following set of differential equations,

$$-ik\left(c - u_0\right)\tilde{u} + ik\tilde{\Phi} = \frac{\mu}{\rho_0}\tilde{u}''\,, \tag{3.12a}$$

$$\tilde{\Phi}' = g\frac{\tilde{T}}{T_0}\,, \tag{3.12b}$$

$$ik\tilde{u} = -\tilde{w}' + \frac{\tilde{w}}{H_\rho}\,, \tag{3.12c}$$

$$-ik\left(c - u_0\right)\tilde{T} + \frac{T_0 N^2}{g}\tilde{w} = \frac{\mu}{\rho_0 P_r}\tilde{T}''\,, \tag{3.12d}$$

where a prime indicates differentiation with respect to z. These can then be manipulated, with the introduction of a new variable to compensate for the fall in density with altitude, using Equation 2.35, to obtain a modified form of the TGE, (see Matcheva and Strobel, 1999)

$$\hat{w}'' + m_d^2(z)\hat{w} = 0\,, \tag{3.13}$$

where m_d is the index of refraction modified to include the effects of dissipation given by

$$m_d = \left[\frac{k^2 N^2}{\hat{\omega}\left(\hat{\omega} + i\beta\right)} - \frac{1 - 2H_\rho'}{4H_\rho^2}\right]^{1/2}\,. \tag{3.14}$$

Here,

$$\hat{\omega} = \omega_r + i\omega_i\,, \tag{3.15}$$

where ω_r and ω_i are defined by

$$\omega_r = k\left(c - u_0\right) + 2\Re\left(m_d\right)\nu\left(\frac{1}{2H_\rho} - \Im\left(m_d\right)\right) \tag{3.16}$$

and

$$\omega_i = \nu\left[\Re\left(m_d\right)^2 - \left(\frac{1}{2H_\rho} - \Im\left(m_d\right)\right)^2\right] \tag{3.17}$$

and

$$\beta = \left(\frac{1 - P_r}{P_r}\right)\nu\left[\Re\left(m_d\right)^2 - \left(\frac{1}{2H_\rho} - \Im\left(m_d\right)\right)^2\right]. \tag{3.18}$$

In the absence of viscosity, $\nu = 0$, and Equation (3.13) is the same as the anelastic version of Equation (2.37) for hydrostatic waves in an atmosphere without wind shear. Equations (3.13) to (3.18) are used iteratively to obtain $m_d(z)$. This profile then gives $\mathbf{M}$, which is used to obtain a numerical solution for $\hat{w}(z)$ using Equation (2.45).

3.4.3 Regions where Dissipation is Important

In the discussion of critical layers in Section 2.5.2, it was stated that damping is manifested as an imaginary part within the intrinsic phase speed or the related intrinsic frequency. An indication of the level of damping can, therefore, be obtained by considering the ratio ω_i/ω_r. This ratio is shown in Figure 3.11. It is virtually zero throughout the stratosphere and below. It is clear that damping is not significant in the lower atmosphere. Thus, the results derived in Section 3.2 using the inviscid fluid equations are appropriate for that region but it would not be appropriate to extend the results into the thermosphere without including the effects of dissipation.

3.4.4 Waves in a Dissipative Atmosphere

The waves considered here, as those in previous sections, are thermally forced. Again, the profile of the forcing takes the form of a modified Gaussian centred at 1 scale height above the 1 bar level. As seen in Section 3.2.2, the waves – if they grow large enough – will saturate before reaching the thermosphere. This is illustrated by Table 3.3, which gives the level at which a sample wave

A (K s^{-1})	$u_0 = 35$ m s^{-1} Saturation Level	$u_0 = 350$ m s^{-1} Saturation Level
10^{-3}	$6H_p \sim 7H_p$	$9H_p \sim 10H_p$
10^{-4}	$10H_p \sim 11H_p$	$13H_p \sim 14H_p$
10^{-5}	$14H_p \sim 15H_p$	$17H_p \sim 18H_p$
10^{-6}	$19H_p \sim 20H_p$	$> 20H_p$

Table 3.3 – Height of wave saturation for a wave with $c = 140$ m s^{-1} in two non-sheared flows with $u_0 = 35$ m s^{-1} and $u_0 = 350$ m s^{-1} for various forcing amplitudes.

with $k = 2\pi/2500$ km and $c = 140$ m s^{-1} saturates in the atmosphere of Figure 3.10 (central column labelled $u_0 = 35$ m s^{-1}) and one with 10 times the flow (right hand column labelled $u_0 = 350$ m s^{-1}). The table shows that waves need to have a forcing peak amplitude of around 10^{-5} K s^{-1} or lower in order to reach the thermosphere. This is just one percent of the value used in the earlier analysis, equivalent to about 3 K per rotation of the planet. This ensures that the waves do not saturate before encountering the upper region of the model atmosphere. As before the boundary conditions select for upwardly propagating waves and are based on the WKB solution.

In Figure 3.12 the behaviour of a sample wave dissipating in the lower thermosphere is shown. The dissipation dominates the wave growth above $z/H_p \approx 16$ leading to deposition of momentum into the mean flow, which peaks at $z/H_p \approx 17$. This accelerates the flow, at the peak, by about 500 m s^{-1} per rotation. Even though the wave has a much smaller amount of forcing the magnitude of acceleration is on a par with that seen at the critical layer illustrated in Figure 3.3. This is because of the lower density at this higher region of the atmosphere.

In Figure 3.13 the behaviour of another sample wave, this time with $c = -140$ m s^{-1}, again dissipating in the thermosphere, is shown. The dissipation dominates the wave growth above $z/H_p \approx 18$, which is higher than in the previous example. Further, as in this case $c < u_0$ the deposition of momentum into the mean flow decelerates the flow. The peak deceleration is at $z/H_p \approx 19$. This peak deceleration is about 2 km s^{-1} per rotation. This is a large deceleration, the large magnitude again being due to the lower density at this higher region of the atmosphere.

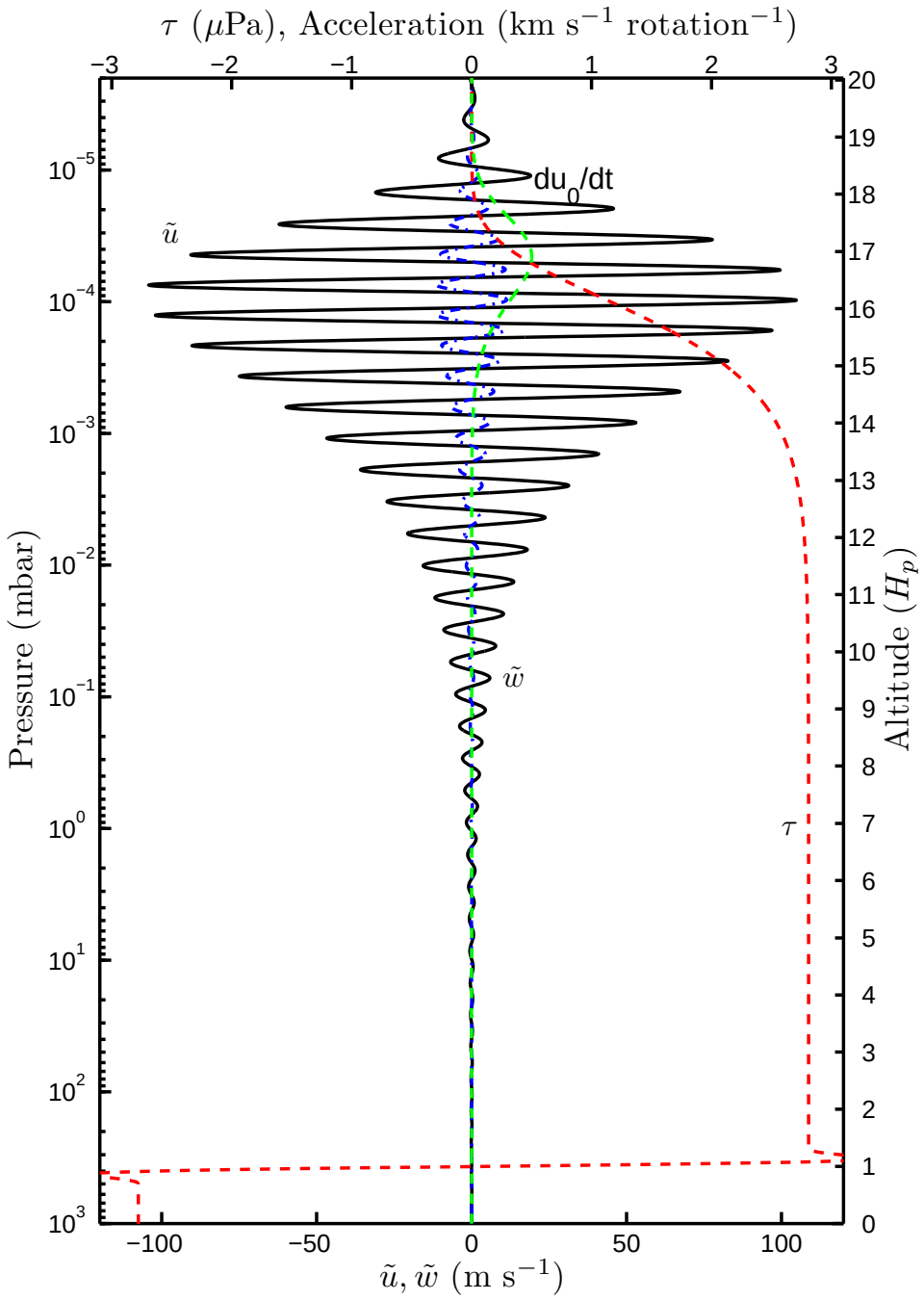

Figure 3.12 – A gravity wave propagating in the atmosphere of Figure 3.10. The horizontal phase speed of the wave c is 140 m s^{-1} and the horizontal wavelength $2\pi/k$ is 2500 km. The vertical perturbation velocity $\tilde{w}$ (-·-), horizontal perturbation velocity $\tilde{u}$ (—), wave stress τ (- - -) and mean flow acceleration $\mathrm{d}u_0/\mathrm{d}t$ (- - -) are shown. As can be seen the wave stops growing above z/H_p = 16. The wave stress starts to fall below this level, depositing momentum, causing an acceleration of the mean flow.

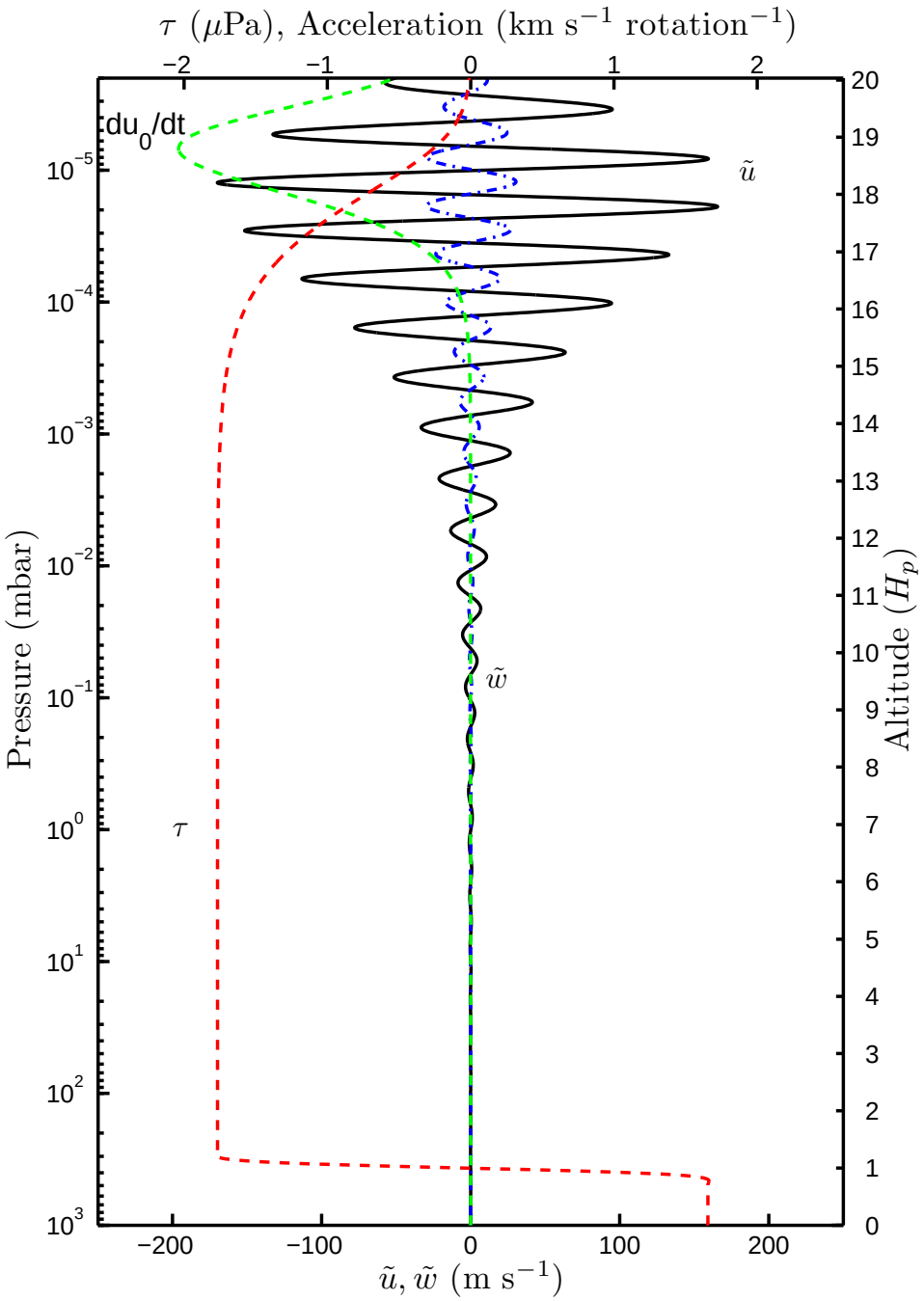

Figure 3.13 – A gravity wave propagating in the atmosphere of Figure 3.10. The horizontal phase speed of the wave c is -140 m s^{-1} (i.e. westward, thus the wave stress is negative) and the horizontal wavelength $2\pi/k$ is 2500 km. The vertical perturbation velocity $\tilde{w}$ (-·-), horizontal perturbation velocity $\tilde{u}$ (—), wave stress τ (- - -) and mean flow acceleration $\mathrm{d}u_0/\mathrm{d}t$ (- - -) are shown. As can be seen, the wave starts to dissipate above $z/H_p \approx 16$. The wave stress falls, depositing momentum, thus, causing a mean flow deceleration which peaks at $z/H_p \approx 19$.

These two examples demonstrate the large changes to the flow in the thermosphere of hot EGPs that can be caused by small, and presumably, common gravity waves. However, the net effect on the thermosphere will depend on the spectrum of waves that manage to reach that region. The types of waves filtered by the lower parts of the atmosphere will vary over time and location. As can be seen in Figure 3.2, there is a prograde equatorial jet. This will tend to filter out waves with positive phase speed. However, at the mid latitudes the flow is mainly retrograde; thus, an entirely different spectrum of waves will be filtered at these latitudes. Any parametrisation of the effects of gravity waves in EGP thermospheres would need to take this into account.

3.5 Conclusion

Gravity wave propagation and the deposition of momentum and energy are complicated by the environment in which the wave propagates. For example, spatial variability of the background winds causes the wave to be refracted, reflected, focussed and ducted. Additionally, temporal variability of the background winds causes the wave to alter its phase speed. Still further complications arise due to the waves's ability to generate turbulence, which can modify the source or serve as a secondary source, and the interaction between the wave and the vortical (rotational) mode of the atmosphere. Many of these issues are, as yet, not well understood and are areas of active research.

This chapter has emphasised only some of these issues. It has shown that gravity waves propagate and transport momentum and heat in the atmospheres of hot tidally-locked extrasolar planets and that gravity waves play an important role in those atmospheres. They modify the circulation through exerting accelerations on the mean flow whenever the wave encounters a critical level, saturates or dissipates. They also transport heat to the upper stratosphere and thermosphere, causing significant heating in these regions. Moreover, through ducting, they also provide a mechanism for transporting heat from the day-side of tidally synchronised planets.

Waves with different characteristics act at different altitudes in the atmosphere. Perhaps counter-intuitively, waves with stronger forcing have impacts in the stratosphere via critical layers and saturation, whereas waves with smaller

forcing are able to penetrate higher into the thermosphere, where they can give rise to significant accelerations and decelerations in the mean zonal flow.

Before relying on GCMs for quantitative descriptions of hot extrasolar planet atmospheric circulations, further work needs to be performed to ensure that the effects of important sub-scale phenomena, such as gravity waves, discussed here, are accurately parametrised and included in the GCMs.

Chapter 4

Gravity Waves on Jupiter

Gravity waves have been observed in the atmospheres of bodies throughout the Solar System: on giant planets, such as Saturn (e.g., Harrington, French, and Matcheva, 2010); on rocky planets, such as Mars (e.g., Creasey, Forbes, and Keating, 2006); and moons, such as Titan (e.g., Friedson, 1994). The behaviour of these waves, as has been shown previously, is controlled by interactions with the atmosphere. Thus, the properties of gravity waves allow the properties of the atmosphere to be deduced. This chapter describes a study using gravity waves observed in Jupiter's atmosphere by the Galileo probe to deduce properties, such at the vertical profile of zonal winds, of Jupiter's atmosphere at the probe entry site.

4.1 The Vertical Structure of Jupiter's Zonal Winds Using Gravity Waves

The vertical structure of Jupiter's winds is not well known—especially away from the visible cloud deck and the equatorial region. Presented in this chapter is an analysis of the properties of mesoscale gravity waves whose signature are found in the Galileo probe data, collected during the probe's descent into Jupiter's atmosphere. This analysis allows the derivation of a vertical profile of the zonal wind from the ~ 0.5 bar level (the upper troposphere) to the $\sim 0.1\,\mu$bar level (the lower thermosphere) at the probe entry site. The profile shows high speed winds of approximately $\sim 150\ \mathrm{m\,s^{-1}}$. Further the location of

the turbopause, where the power spectrum of the waves is broad presumably due to wave breakdown, is identified. The profile suggests a jet, previously identified as related to the quasi-quadrennial oscillation in the stratosphere (so called as the oscillation has a period of four Earth years), oscillates across the equator.

Jupiter's atmospheric circulation is zonal in character. That is the major winds are east-west in direction, alternating between prograde and retrograde regions. This is associated with a banded structure in the clouds on Jupiter. The motion of features in the visible cloud deck have been tracked in images of Jupiter, giving measurements of the flow speed within the bands. This has provided a detailed picture of the meridional structure of the zonal winds (e.g., Ingersoll, 1990; Vasavada and Showman, 2005). However, the vertical structure is much less well known. Measurement by the Galileo probe's Doppler Wind Experiment (DWE) provided a profile at the probe entry site between the 565 mbar and 22 bar levels (Atkinson, Pollack, and Seiff, 1998). The thermal wind balance,

$$\frac{\partial u}{\partial \ln p} = -\frac{R}{f}\left(\frac{\partial T}{\partial y}\right)_p , \tag{4.1}$$

relates the horizontal temperature gradient, $\partial T/\partial y$, to the vertical shear in the horizontal geostrophic wind, $\partial u/\partial \ln p$ (Holton, 2004). Using this balance, analyses of temperature measurements of Jupiter's atmosphere obtained by the Voyager and Cassini spacecraft have given profiles between the 500 mbar and 0.5 mbar levels (Flasar et al., 2004; Simon-Miller et al., 2006). However, the balance is not valid near the equator as f becomes small; therefore, the profiles are not available for the band within about 5° of the equator. Finally, the zonal motions of deeper regions (2 bar level) have been tracked via the hotspots, which are gaps in the main cloud deck (Li et al., 2006). However, no zonal wind speed profile for the region above 0.5 mbar (the highest layer reported in the above studies) is available.

4.1.1 The Galileo Probe's Observations

In December 1995 the Galileo probe entered Jupiter's atmosphere near the equator, at 6° N. It is, to date, the only probe to enter Jupiter's atmosphere so the data it provided are the only in-situ measurements of Jupiter's atmo-

sphere. During the probe's entry the Atmospheric Structure Instrument (ASI) on board collected the accelerations suffered by the probe. Two accelerometers, a_{z1} and a_{z2}, collected acceleration information along the direction of travel every 0.625 s. This acceleration data is shown in Figure 4.1. Note that there is a small oscillation in the acceleration data, this is most easily seen early in the profile. This oscillation is spurious and Seiff et al. (1998) apply smoothing to remove its effects in their calculations. This data is publicly available in NASA's Planetary Data System (at http://pds.nasa.gov). These accelerations were measured for about 4 minutes before the probe entered the descent phase—that is, before the probe deployed its parachute. During this time the probe traversed a layer approximately 1000 km thick between about 1 nbar and 350 mbar. A fuller description of the probe and the ASI is available in Seiff et al. (1998).

Seiff et al. (1998) describes how the temperature profile of the atmosphere traversed during the entry phase can be derived from the accelerations. Firstly, the density of the atmosphere can be recovered from the accelerations, if the aerodynamics of the probe are known, using

$$\rho = \frac{2ma_z}{C_D A V_r^2}\,, \tag{4.2}$$

where m is the mass of the probe, a_z is the acceleration measured by the accelerometers a_{z1} and a_{z2}, C_D is the probe's drag coefficient, A is the probe's cross-sectional area and V_r is the probe's velocity. Values for all these properties, as functions of time, can be obtained from Seiff et al. (1998). The density profile recovered is shown in Figure 4.2. Then assuming that the atmosphere is in hydrostatic balance and integrating,

$$\int_p^{p_{top}} \mathrm{d}p = -\int_z^{z_{top}} \rho g \mathrm{d}z\,, \tag{4.3}$$

gives the pressure

$$p = p_{top} + \int_z^{z_{top}} \rho g \mathrm{d}z\,. \tag{4.4}$$

There is a difficulty in evaluating this as the constant of integration, p_{top}, the pressure at the start of the measurement, is unknown. The range of plausible values gives a wide variation in temperatures, $\sim$ 700 K to $\sim$ 1200 K at the top of the profile. However, as shown in Seiff et al. (1998), these profiles

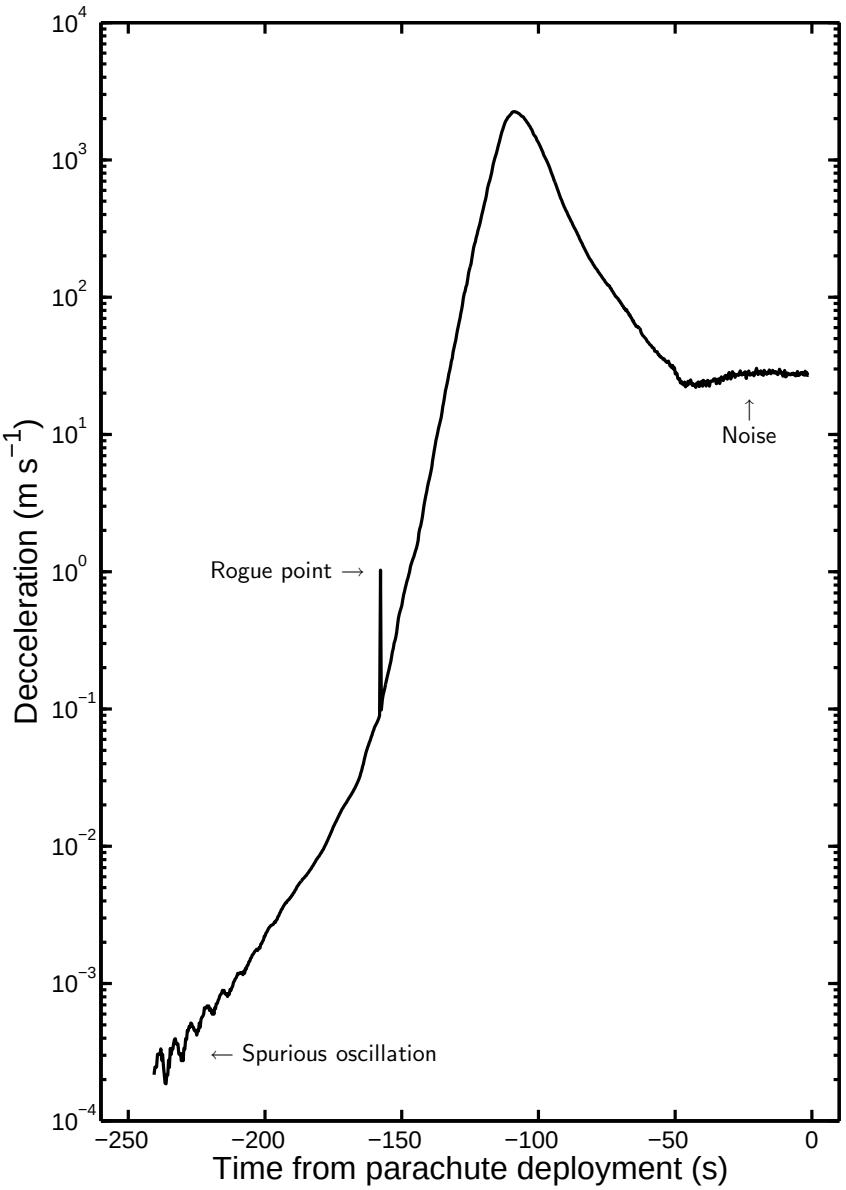

Figure 4.1 – The accelerations felt by the Galileo probe during its entry into Jupiter's atmosphere are shown in this figure. Note the spurious oscillation clearly visible in the early part of the profile. The cause of this oscillation is unknown, though currents induced by Jupiter's magnetic fields is a possibility (Seiff et al., 1998). However, these oscillations are small and soon swamped by the true signal; so, no attempt to smooth them is made in the analysis. Later in the data is a single rogue point with a spuriously large value. This was caused by a reading being taken as the same time as the accelerometer was changing measurement range. These activities were not synchronised. This point is excluded from the analysis. In the last region of the profile the probe is travelling sub-sonically, this increases unsteadiness in the wake of the probe and so in its drag coefficient leading to the noise in this part of the profile.

converge to a single profile below about 500 km above the 1 bar level. The analysis presented here is restricted to the region below this altitude, thus avoiding any difficulty due to the unknown initial value. Finally, by assuming that the atmosphere is an ideal gas the temperature can be obtained from the pressure and density profiles. Profiles for required quantities, such as the accelerations due to gravity g and the specific gas constant R, are available in Seiff et al. (1998). The calculation presented here closely follows Seiff et al. (1998). The main difference is that the spurious oscillation in the acceleration measurement is not removed through smoothing the data. This means that large oscillations appear in the upper part of the recovered temperature profile. These oscillations can be clearly seen in the upper part of Figure 4.3. However, the analysis performed in the following sections applies only to the region below 500 km where the oscillation is insignificant, so smoothing is not required. After the parachute was released the probe slowly descended for about an hour through a further 150 km of the atmosphere, down to the 22 bar level. During this phase it collected temperature and pressure data directly with sensors. The probe then stopped transmitting. The temperature profile for the region traversed by the probe is shown in Figure 4.3.

Analyses of a smoothed thermospheric temperature profile (Young et al., 1997) and of the stratospheric profile (Young et al., 2005) have identified discernible temperature perturbations, which have been interpreted as manifestations of atmospheric gravity waves. Such observations are not unique to the temperature profile gathered by Galileo. Vertical temperature profiles for Jupiter's atmosphere have also been obtained from studies of occulted stars and spacecraft. Stellar occultation studies have a long history going back to the study by Baum and Code (1953). The attenuation of the starlight as the planetary atmosphere occults the star is mainly caused by refraction rather than molecular scattering. The index of refraction depends on the atmospheric density so the photometry of the occultation can provide a vertical temperature profile (see Elliot and Olkin, 1996, for a review of the technique). A number of these profiles contain temperature oscillations that have also been characterised as manifestations of vertically propagating gravity waves (French and Gierasch, 1974; Hubbard et al., 1995; Lindal, 1992; Raynaud et al., 2003; Raynaud et al., 2004).

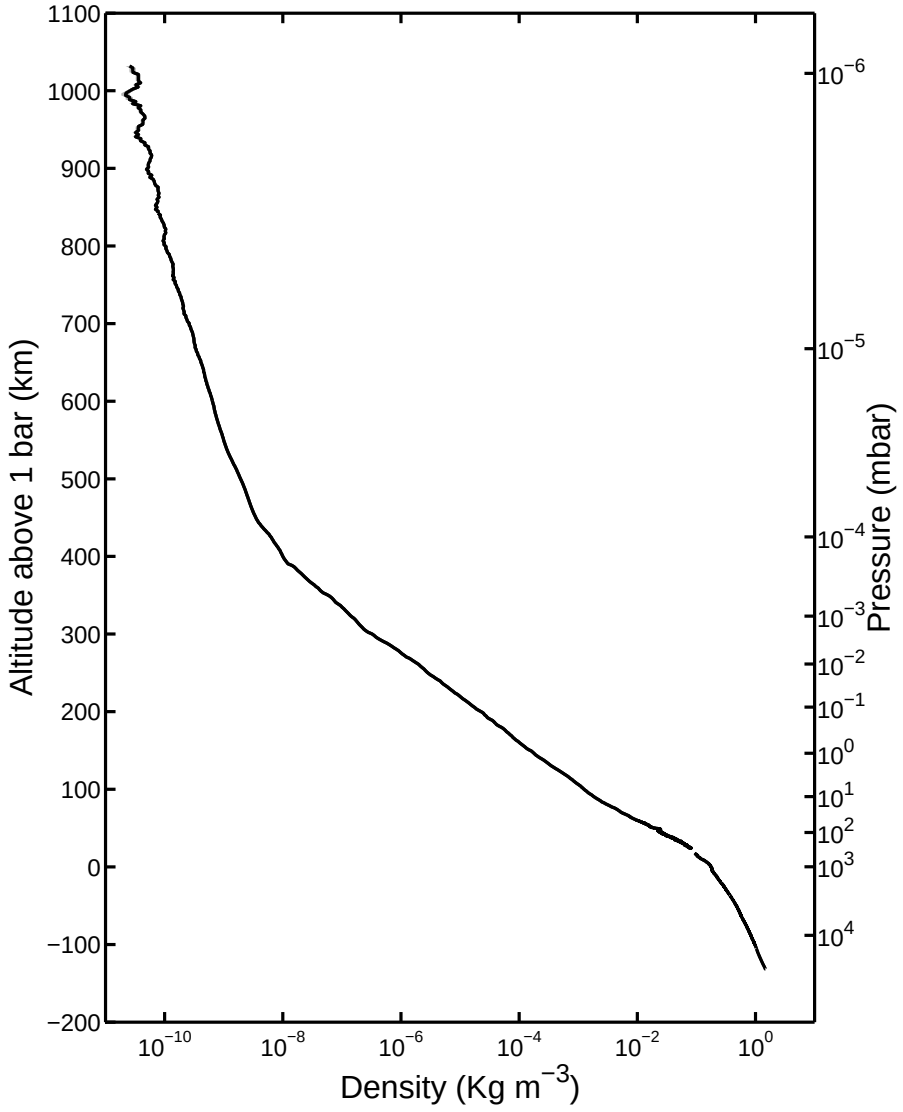

Figure 4.2 – The figure shows the density of Jupiter's atmosphere, recovered from the Galileo probe's ASI acceleration data using Equation (4.2), as described in Seiff et al. (1998). The shaded area, which is hardly wider than the line itself, shows the uncertainty in the value due to the resolution of the sensors. At the top of the profile there are fluctuations in the density. These arise from the spurious oscillation in the acceleration data as shown in Figure 4.1. The break in the profile just above the 1 bar level is where the probe's parachute was deployed.

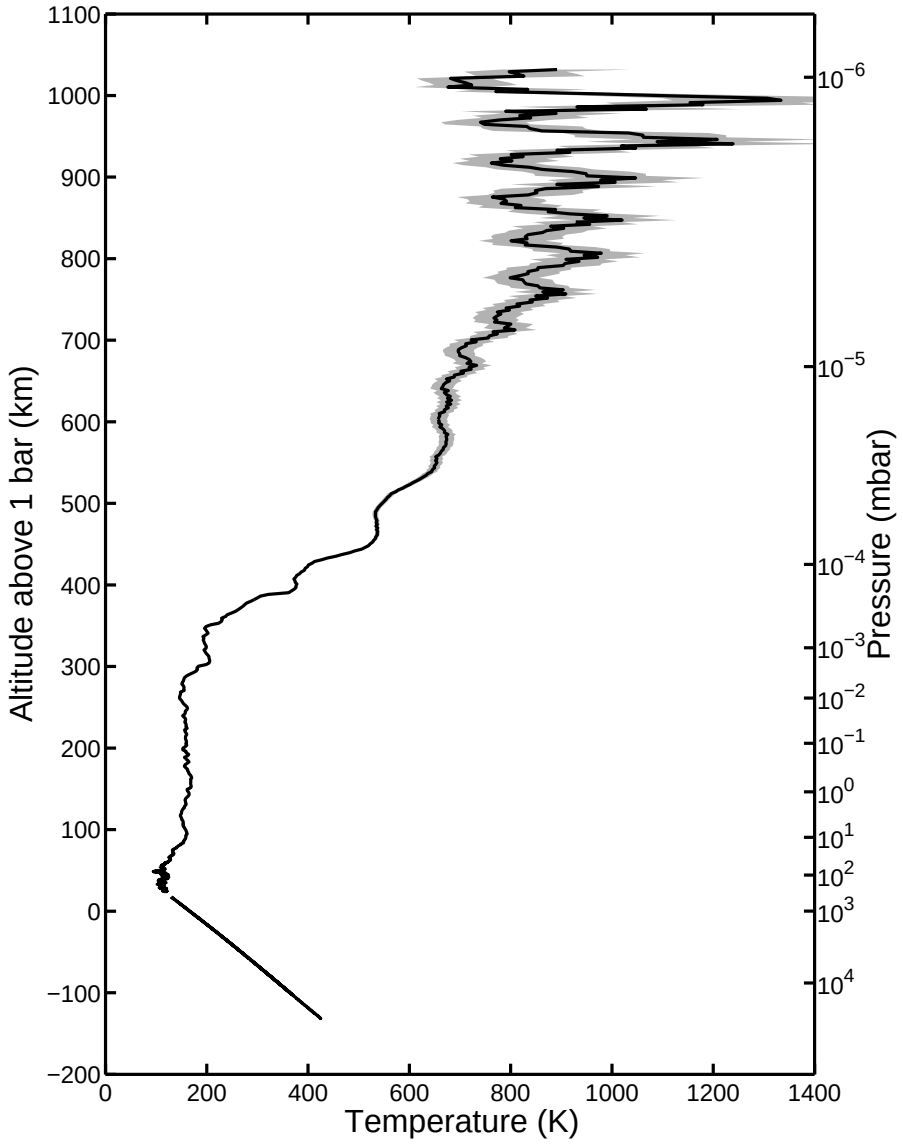

Figure 4.3 – The figure shows the temperature of Jupiter's atmosphere, recovered from the Galileo probe's ASI acceleration data via Equations (4.2), (4.4) and (2.2), as described in Seiff et al. (1998). The shaded area shows the uncertainty in the value due to the resolution of the sensors. Note that this uncertainty is plotted for all altitudes but is so small as to not be visible for altitudes below about 500 km. At the top of the profile there are large fluctuations in the temperature. These are not real but arise from the spurious oscillation in the acceleration data as shown in Figure 4.1. Note that these oscillations become insignificant below 500 km. To avoid these problems and the issue of an unknown initial pressure value, as discussed in the main text, the analysis of the temperature data is restricted to the 500km thick layer above the 1 bar level. The break in the profile just above the 1 bar level is where the probe deployed its parachute.

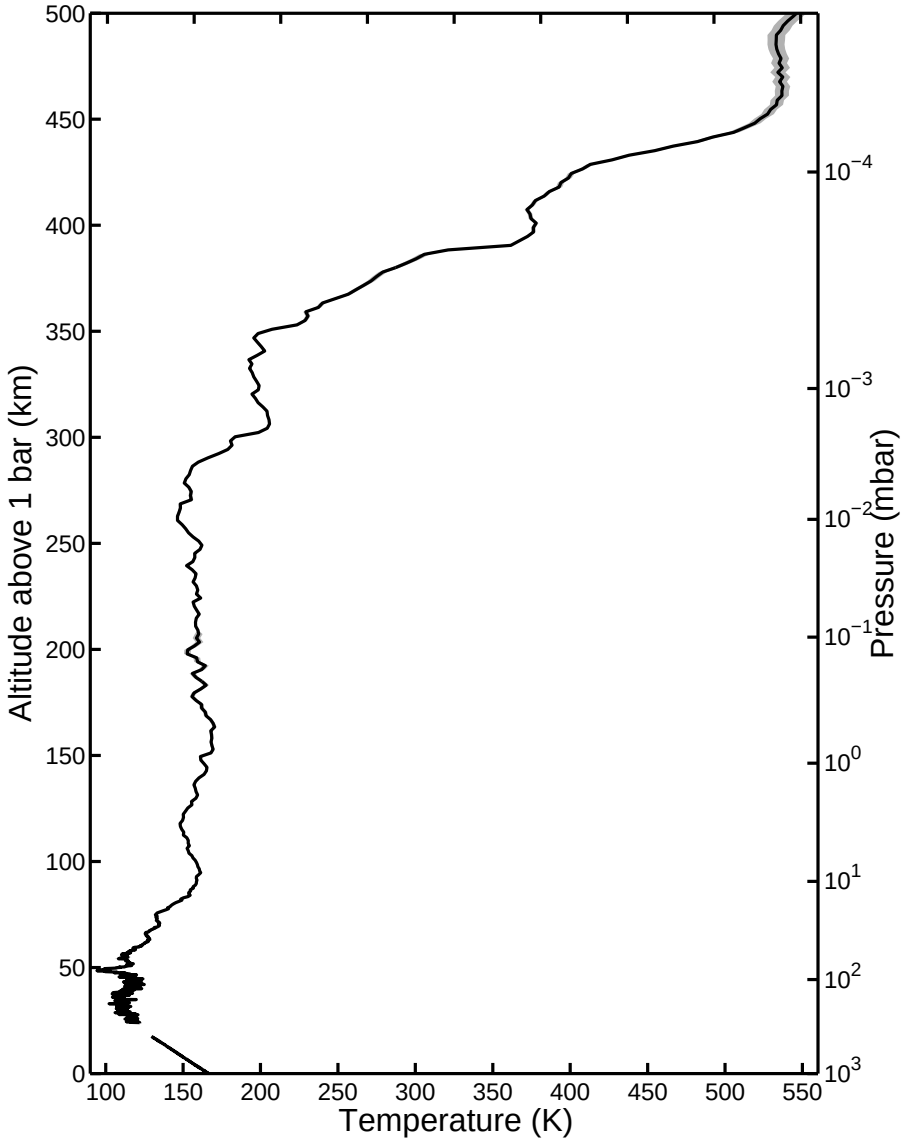

Figure 4.4 – The figure shows the temperature of Jupiter's atmosphere, at the Galileo probe entry site, that is considered in this analysis. The region shown covers the upper troposphere (where the temperature decreases with altitude), stratosphere (which is roughly isothermal) and the lower thermosphere (where the temperature increases with height). Within these three regions wave-like structures with vertical wavelengths of a few tens of kilometres can be seen, especially in the stratosphere. Note the the very small wavelength oscillations in the region from 2 km to 50 km above 1 bar are due to the noise in the data caused by the subsonic travel of the probe during this part of its entry phase, as shown in Figure 4.1.

4.1.2 Gravity Waves in Jupiter's Atmosphere

As discussed in Chapter 2 gravity waves are oscillations of fluid parcels about their altitudes of neutral buoyancy and are a common feature of stably stratified atmospheres. They have been captured in images of Jupiter's clouds as a collection of lines (presumably phase lines) imposed on the background cloud layer. Figure 4.5 shows an example. Flasar and Gierasch (1986) surveyed dozens of waves captured in images taken by the Voyager spacecraft during their flybys of Jupiter in 1979. This allowed general features of these waves to be derived. They found that the waves predominantly occur in the equatorial region and that the majority ($\sim 80\%$) of waves have wavefronts aligned within 10° of north-south. Typically the waves have wavelengths of 300 km. Gravity waves have also been identified in the images from the Galileo orbiter (Arregi et al., 2009). A sequence of images from the New Horizons spacecraft taken during its flyby of Jupiter in 2007 has allowed wave and cloud features to be tracked giving a value for the wave phase speed relative to wind speed, the wave's intrinsic phase speed. The wave phase travels about 100 m s^{-1} faster than the clouds. (Reuter et al., 2007).

As discussed in Section 2.2.1 the effects of rotation can be neglected when the inertial terms dominate the Coriolis terms. In this case, that is when the horizontal scale of the waves is less than U/f, where U is the characteristic flow speed taken as ~ 100 m s^{-1} for the probe entry site and $f = 2\Omega sin\varphi = 3.68 \times 10^{-5}$ s^{-1}. Thus for waves with horizontal wavelengths less than ~ 2720 km rotation can be ignored. As shown above typical horizontal wavelengths are an order of magnitude smaller than this so rotation can be safely neglected in this study. Therefore, the dynamics of these gravity waves is described by the Taylor–Goldstein equation,

$$\frac{\mathrm{d}^2 w}{\mathrm{d}z^2} + m^2(z)\, w \;=\; F(z)\,. \tag{4.5}$$

Here w is the perturbation in the vertical velocity, adjusted for the amplitude growth and assumed to be oscillatory in the horizontal direction and time; F is a forcing function, which represents the source of waves; and, m is the vertical wavenumber, which depends on the physical properties of the medium

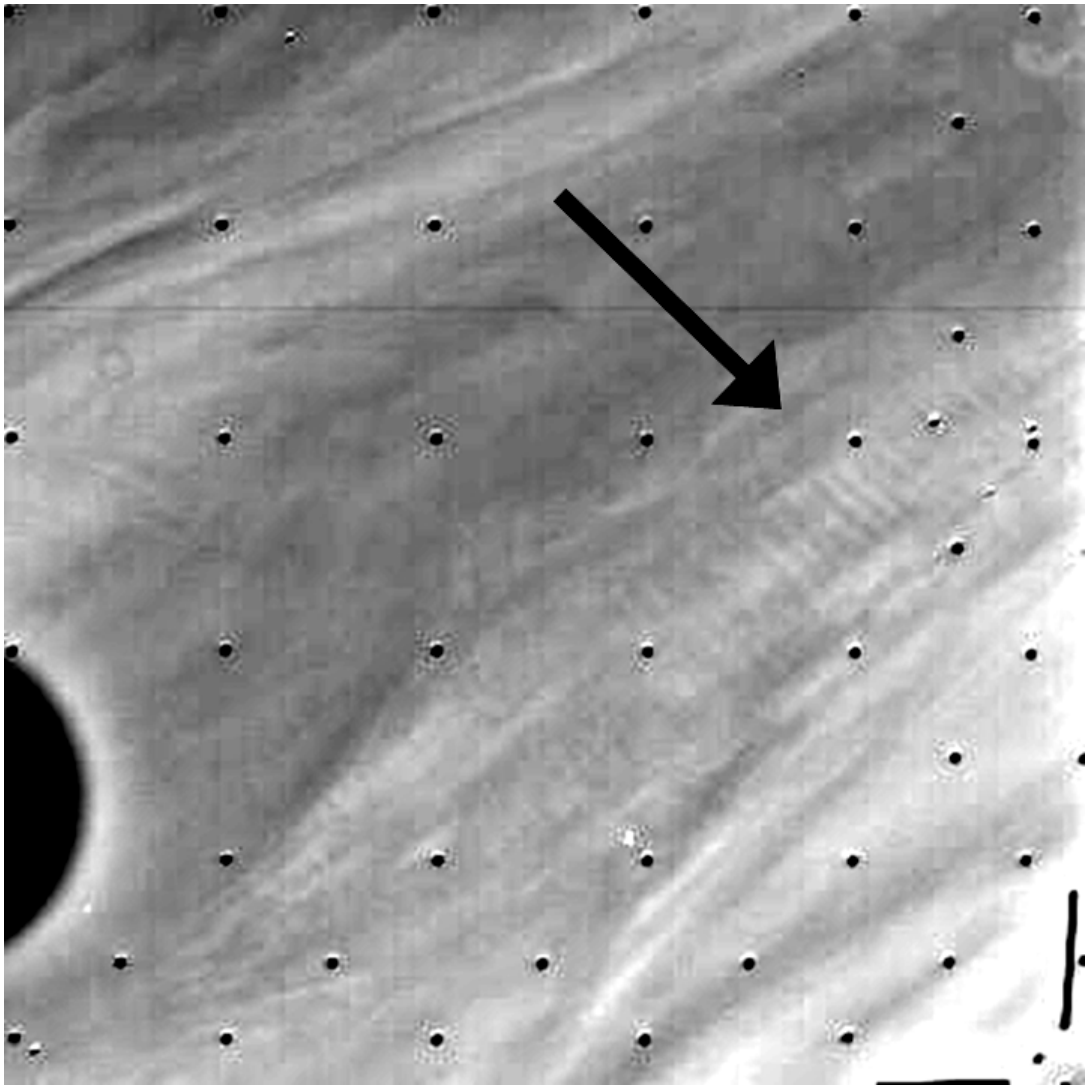

Figure 4.5 – The image shows a gravity wave in Jupiter's atmosphere in an extract from Voyager image 16316.34. The wave's location is indicated by the arrow. The wave fronts can be see as an alternating series of darker and lighter lines in cloud deck. This wave is propagating horizontally in the troposphere. Many such waves are captured in the Voyager images (Flasar and Gierasch, 1986). Here, the image contrast has been enhanced to improve the visibility of the wave. The wave is located just south (1.4°) of the equator and has a wave length of 323 km. The dark segment of a circle in the bottom left is part of the shadow of one of Jupiter's moons. Image courtesy NASA/JPL-Caltech.

Parameter	Symbol	Value
Specific gas constant	R	$4000 \sim 3600$ J kg^{-1} K^{-1}
Ratio of specific heats	$\gamma = c_p/c_v$	$1.4 \sim 1.5$
Acceleration due to gravity	g	~ 23 m s^{-1}
Rotation rate	Ω	1.76×10^{-4} s^{-1}
Probe entry location		$(6°N, 5°E)$

Table 4.1 – Parameters for the Galileo Probe Entry Site

in which the waves propagate. We use the anelastic TGE so,

$$m(z) \;=\; \left[\, \frac{N^2}{I^2} - \frac{1}{I}\frac{\mathrm{d}^2 I}{\mathrm{d}z^2} - \frac{1}{H_\rho I}\frac{\mathrm{d}I}{\mathrm{d}z} - \frac{1}{4H_\rho^2}\left(1 - 2\frac{\mathrm{d}H_\rho}{\mathrm{d}z}\right) - k^2 \,\right]^{1/2}, \qquad (4.6)$$

where N is the Brunt–Väisälä (buoyancy) frequency; I is the intrinsic phase speed, $c - u_0$; H_ρ is the density scale height; and, k is the horizontal wavenumber. In general, all of the variables depend on altitude z. Crucially, the zonal wind profile $u_0(z)$ can be obtained by solving for $I = I(H, k, N, m)$ in (4.6), which leads to the non-linear second order differential equation,

$$I\frac{\mathrm{d}^2 I}{\mathrm{d}z^2} + \frac{I}{H_\rho}\frac{\mathrm{d}I}{\mathrm{d}z} + \left[\frac{1}{4H_\rho^2}\left(1 - 2\frac{\mathrm{d}H_\rho}{\mathrm{d}z}\right) + k^2 + m^2\right] I^2 - N^2 = 0\,. \qquad (4.7)$$

This inversion this allows a profile for the zonal wind to be derived that spans a much larger range of altitude above the 1 bar level ($\sim$500 km) than the past analyses described above.

$H_\rho(z)$ is computed from the density profile derived using Equation (4.2) and the definition of the density scale height (2.15). The horizontal wavenumber is taken from the analysis of Flasar and Gierasch (1986); that is $k = 2\pi/300\,\mathrm{km}^{-1}$ using the average wavelength they obtained.

To obtain N a background profile for the potential temperature, $\bar{\theta}$, is required. This potential temperature profile, θ, is calculated using the definition of potential temperature, Equation (2.3), the pressure profile derived from the density profile and the temperature profile shown in Figure 4.4. The reference pressure is set as $p_{\mathrm{ref}} = 1$ bar. The profile of $\kappa = R/c_p$, with R the specific gas constant and c_p the specific heat at constant pressure, can be derived from data supplied in Seiff et al. (1998). The vertical profile of θ is shown in Figure 4.6A.

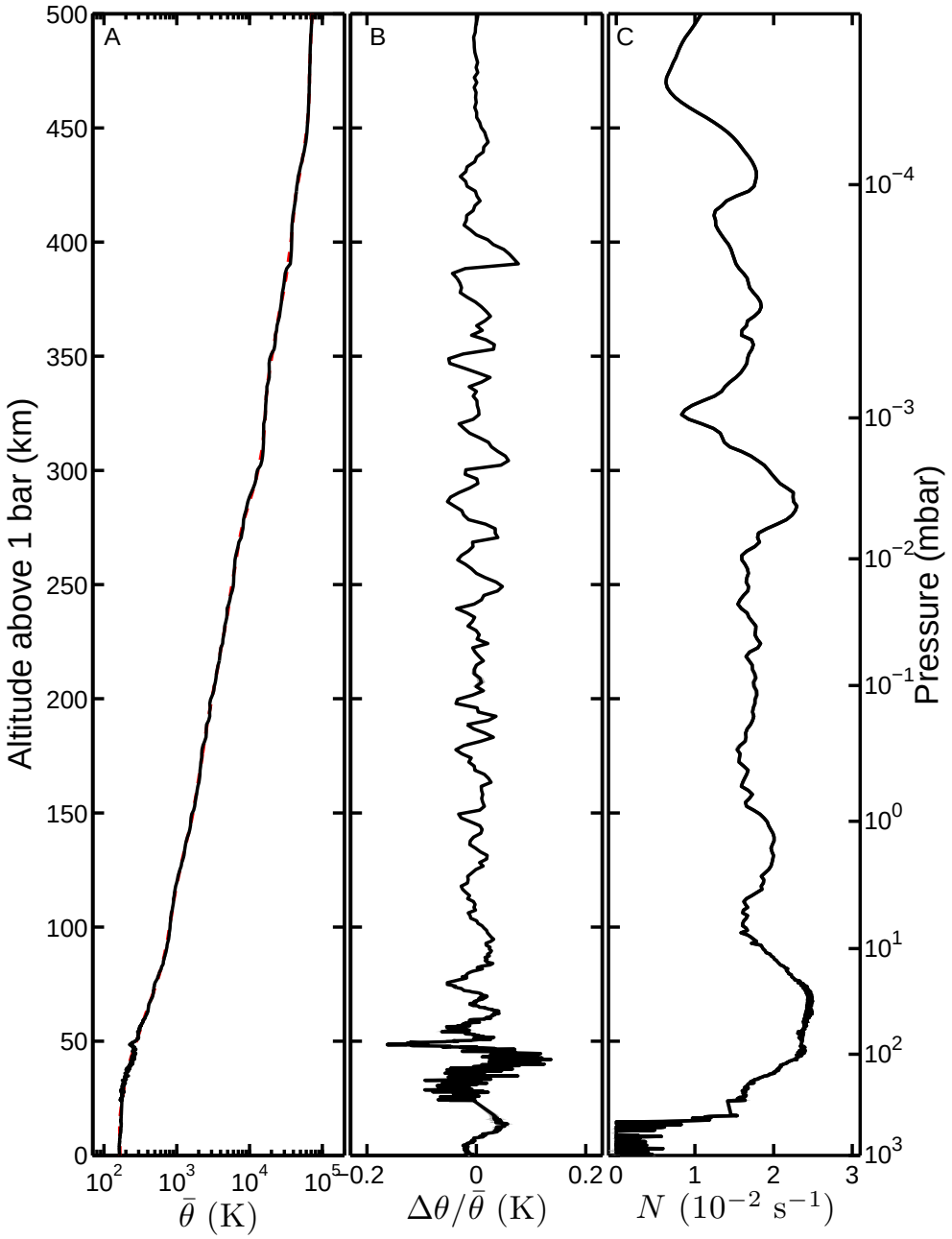

Figure 4.6 – The figure shows potential temperature, relative potential temperature perturbation and Brunt–Väisälä (buoyancy) frequency profiles for Jupiter's atmosphere at the probe entry site. All altitudes are relative to the 1 bar pressure level. **A)** The vertical profile of potential temperature, θ, is shown as a solid line (—). Also shown is the background potential temperature, $\bar{\theta}$ shown as a dashed line (- - -). **B)** The vertical profile of potential temperature perturbations, $\Delta\theta$, scaled by the background value, $\bar{\theta}$. The perturbations show wavelike oscillations throughout the stratosphere and lower thermosphere. Note that the short wavelength oscillations in the layer between 25 km and 50 km are due to accelerations caused by buffeting of the probe as its velocity became subsonic. **C)** The vertical profile of the Brunt–Väisälä frequency, which shows the stability of the atmosphere against convective stability.

The profile for θ is decomposed into a mean background $\bar{\theta}$ profile and a small perturbation $\Delta\theta$ profile taken about the mean. This perturbation is presumed to be due to the mesoscale gravity waves whose properties are to be studied. Such a decomposition of temperature is standard in gravity wave studies (Lindzen, 1990; Nappo, 2002; Young et al., 1997) and is reasonable here given that the spatial scales of the background and waves are well separated. Further, the horizontal distance travelled by the probe in the region studied, 3300 km, is small compared to Jupiter's circumference; hence, zonal (east-west) variation in the background over this distance is not expected to be significant.

The background value for each point is identified by fitting a cubic to the potential temperature data in a smoothing window centred on the point. A cubic, having two turning points, can fit up to 1 wavelength of fluctuation in the field. Thus fluctuations with wavelengths of the order of the smoothing window and larger can be fitted to the cubic and identified as a change in the background. The background value is taken to be the value of the cubic at the centre of the window. This is illustrated in Figure 4.7. Smaller scale fluctuations cannot be fitted to the cubic and so are not smoothed, they are identified as the mesoscale fluctuations required for the analysis. This acts as a low-wavenumber-pass filter, thus giving a profile of the background as the background varies on large scales compared to the mesoscale waves. The exact profile obtained varies a little with the size of smoothing window used. To allow for this the complete analysis was repeated for several windows varying in size from 55 km to 85 km. This technique for obtaining a background temperature profile has been used in a previous study of data obtained via the Galileo probe investigating the stability of Jupiter's troposphere (Magalhães, Seiff, and Young, 2002). The vertical profile of $\bar{\theta}$, using a 75 km-deep moving window is shown in Figure 4.6A as a dashed line. The perturbation is recovered using,

$$\Delta\theta = \theta - \bar{\theta}\,. \tag{4.8}$$

This analysis works with the relative perturbation $\Delta\theta/\bar{\theta}$ as this directly related to the perturbation in the vertical velocity, w, as shown by polarization relation (2.50c). This profile is presented in Figure 4.6B.

The *Brunt–Väisälä* frequency is derived from $\bar{\theta}$ using Equation (2.10). This is shown in Figure 4.6C. Note that N is much smaller in the region below $\sim$20 km

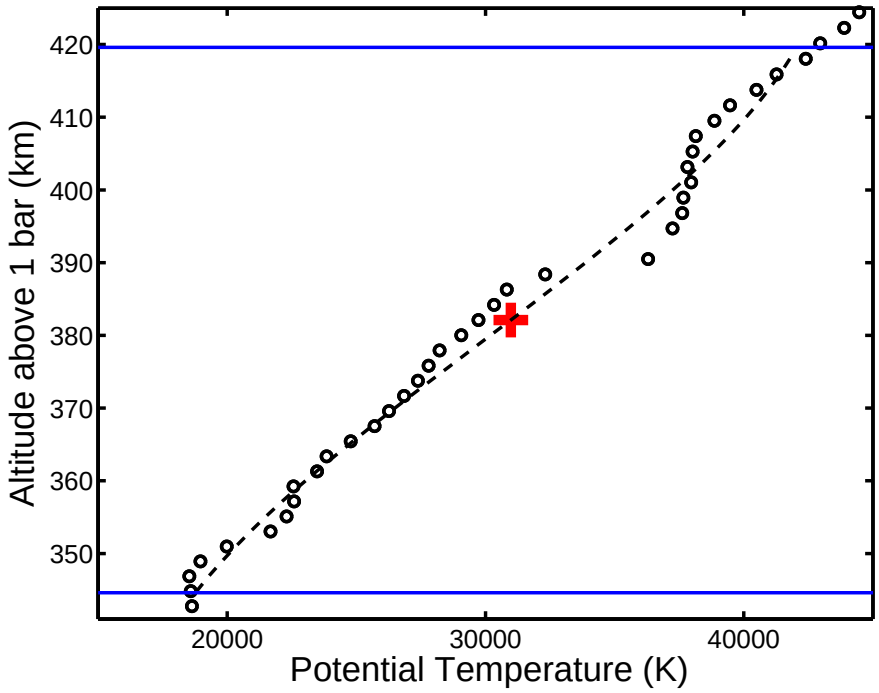

Figure 4.7 – The background profile is obtained by smoothing the profile. The smoothed value for a given point is the value of a cubic, fitted to the data in a given window, as illustrated in the figure. Here the point at $z = 382$ km is being smoothed. The data points are shown as circles, the upper and lower limits of the 75 km window are shown as solid lines (—) and the fitted cubic as a dashed line (**- - -**). The smoothed value for the point is the value of the cubic at 382 km and is indicated by the red cross.

than that above, in the stratosphere. This represents a possible ducting region, a source for the waves in the probe data. Such a region was hypothesised by Flasar and Gierasch (1986) as the location of the mesoscale waves observed in the Voyager images such as the one shown in Figure 4.5.

Although w information was not collected by the probe, as mentioned above from the polarisation relations it is clear that w and $\Delta\theta/\bar{\theta}$ are directly related, that is waves in the two quantities have the same wavenumbers. As can be seen in Figure 4.6B there are wave-like oscillations in the potential temperature perturbation. Therefore, $m(z)$ can be obtained by identifying the wavenumbers of these features.

To identify the profile of the wavenumbers a series of Lomb-Scargle periodograms (Scargle, 1982) of the $\Delta\theta/\bar{\theta}$ data were generated. The original readings by the probe were uniformly spaced in time; so, as the probe's velocity changed during its entry, the data are non-uniformly spaced in z. This non-uniform spacing renders analysis by standard fast Fourier or wavelet transforms unsuitable. However, the Lomb-Scargle periodogram provides the means for simply analysing unevenly spaced data. In a process analogous to the short-term Fourier transform a periodogram at each z is generated using the data points in a given window. Figure 4.8 shows an example of this process where the window is 60 km in extent and centred on the point at $z = 298$ km. This gives the spectral energy density as a function of wavenumber for the chosen altitude. We have also verified that the obtained result varies little between different sized periodogram windows. All the periodograms are subsequently combined to produce a two-dimensional map of the spectral energy density as a function of wavenumber and altitude, $\mathcal{E} = \mathcal{E}(m^*, z)$, shown in Figure 4.9; here m^* is the vertical wavenumber m prior to an adjustment for wave propagation geometry.

Three features which are apparent in the $\mathcal{E}$ map. First, regions with higher values of spectral energy density (shown in the figure as red and yellow) are common, especially below about 400 km, indicating that gravity waves are a common feature of this region of the atmosphere. Gravity waves that have been identified previously (Young et al., 2005) are recovered (labelled as W1 and W2 in the map). This agreement gives confidence in the procedure used to identify the properties of the gravity waves in the data. However, in addition to those waves, several new comparable gravity waves are identified in the analysed

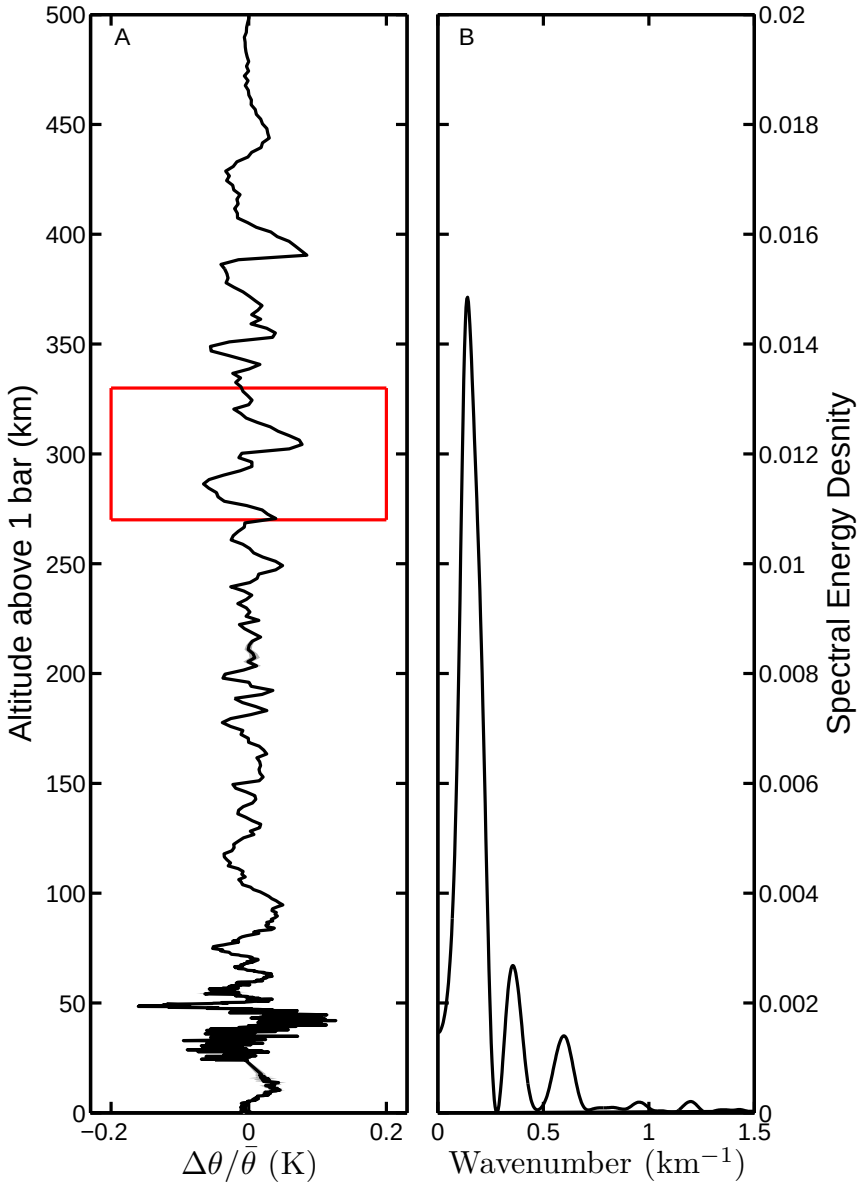

Figure 4.8 – An example of the Lomb-Scargle periodogram. **A)** The variation of $\Delta\theta/\bar{\theta}$ with z as shown in Figure 4.6B with a 60 km periodogram window indicated in red centred on the point at $z = 298$ km. **B)** Shown here is the Lomb-Scargle periodogram for the points in the window shown in A. This shows a peak at a wavenumber of about 0.13 km^{-1}. This process is repeated for each point and the resulting periodograms combined to create a map like the one in Figure 4.9.

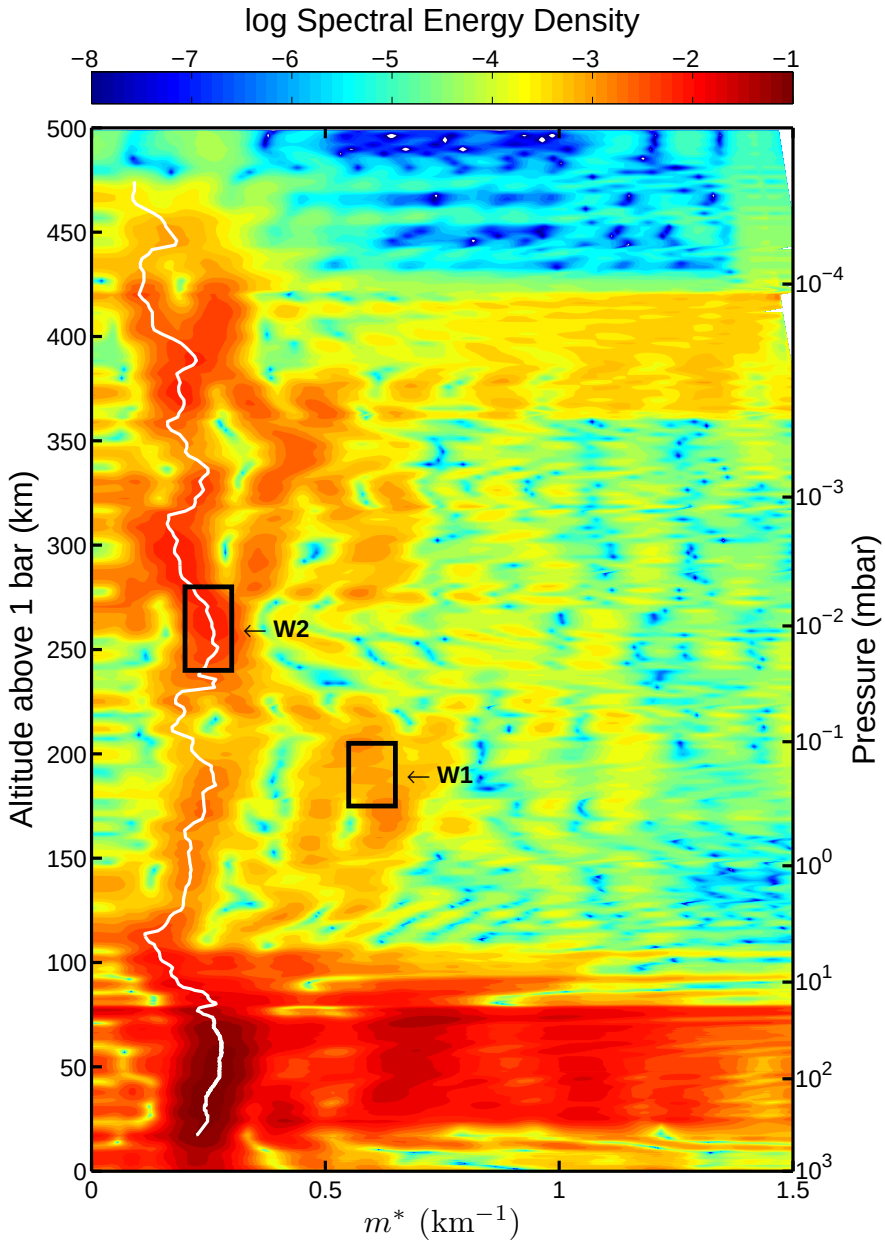

Figure 4.9 – Shown here is a moving Lomb-Scargle periodogram of the potential temperature perturbation from Figure 4.6B. Regions of high spectral energy are in red and low energy is in blue. The variation of the observed vertical wavenumber m^* is shown (white line). The line is produced by identifying local energy maxima and constructing a line joining them, avoiding local minima. Note that there are other waves that can be identified within the periodogram. One such wave, the region of high energy at $m^* \approx 0.61$ km^{-1} between 180 km and 210 km altitude (labelled W1) has been previously identified as a saturating gravity wave (Young et al., 2005). Another region (labelled W2) has also been previously identified (Young et al., 2005). The region at an altitude of around 400 km shows a broadening of the range of wavenumbers with increased spectral energy. This is indicative of the turbopause, the region where waves break and the atmosphere begins to become heterogeneous.

domain. In particular, note the high energy density (dark red) regions near the 50 km, 300 km and 400 km altitudes.

Second, the analysis identifies a region consistent with a turbopause centred at $\sim$400 km altitude. This is the region where the width of the sub-spectrum containing significant energy increases markedly. In this region, molecular diffusion becomes comparable to eddy diffusion and gravity waves, growing in amplitude, as they propagate upward break, transferring energy into higher wavenumbers. Above this region, energy is lower across the entire spectrum and the spectrum itself is much steeper than that for the turbopause region. Above the turbopause region, the atmosphere becomes inhomogeneous, separating out into layers of different molecular species. Knowing the level at which Jupiter's atmosphere becomes inhomogeneous is important, for example, in the interpretation of stellar occultations as the change of composition leads to changes in the index of refraction of the atmosphere. Past studies, based on observations, have placed Jupiter's turbopause at the $\sim$ 5 μbar (Festou et al., 1981) and $\sim$ 0.5 μbar (Yelle et al., 1996) levels. This analysis supports the latter location.

Third, as mentioned previously, in the lower part of the analysed domain there appears to be a ducting region, a region with a sharp jump in N. Such a region can serve as a source of gravity waves. Horizontally propagating gravity waves in this region have previously been observed (see, e.g., Figure 4.5), which have been suggested as waves trapped in a "leaky" duct. The ducted wave travels horizontally by undergoing internal reflections at the boundaries; however, part of the wave escapes the duct to propagate vertically. Because the wavenumber with maximum energy in the $\mathcal{E}$ map can be traced down to the ducting region, it is likely that the waves have come from there. Note that above this region the number of local peaks in the spectrum generally reduces with altitude. Also, the magnitude of the peak energy in the low wavenumber (white line in Figure 4.9) is high at first ,below about 125 km, then decreases, and then increases again,above about 225 km, along the white line, until the topside of the turbopause region at $\sim$ 425 km above the 1 bar level. This is indicative of wave saturation (or encounters with a critical layer, where $I = 0$ locally) for this wave as it propagated upward. There are regions where there are multiple peaks in the energy density at $\sim$ 200 km and $\sim$ 300 km above the 1 bar level, these multiple peaks may be due to wave breaking and secondary

wave generation from breaking layers.

4.1.3 The Zonal Wind Profile

As alluded to earlier, m^* differs from the required wavenumber m. The latter is the wavenumber that would be observed by a probe travelling in a vertical direction. However, throughout most of its entry phase, the probe had a shallow angle of attack ($\sim 6^\circ$ below the horizontal), which changes the wavenumber observed by the probe during its passage in the upper part of the analyzed domain. The situation is sketched in Figure 4.10. The geometry of the probe's path is used to obtain the true vertical wavenumber,

$$m = \left(\frac{\tan\gamma \, \tan\beta}{1 - \tan\gamma \, \tan\beta} \right) m^*, \tag{4.9}$$

where γ is the angle of attack and β is the angle the wavevector makes with the horizontal. We make no correction for the relative motion of the probe with respect to the wave since the probe's velocity is supersonic (indeed, hypersonic, with up to Mach 51) for much of the entry phase. Gravity wave phase speeds are subsonic.

Although γ is known from the probe's trajectory (Seiff et al., 1998), β is not. To estimate this quantity, it is assumed that the probe's trajectory is vertical in the period just before parachute deployment. This is not far from the actual situation since the probe's angle of attack was 83° just before the parachute was deployed (Seiff et al., 1998). In this region, $m^* \approx m$; and, since

$$\beta = \arccos\left(\frac{k}{\sqrt{k^2 + m^2}} \right), \tag{4.10}$$

we have $\beta \approx 85^\circ$. Now, all the parameters required to recover I have been obtained, and a vertical profile for I can be estimated by solving (4.6). The equation is solved using two numerical techniques; a variable order Adams-Bashforth-Moulton predictor-corrector solver and a 7th order Runge-Kutta solver. No difference was seen between the two solutions.

Finally, to obtain u_0 from I, a value for the horizontal phase speed c is required. Unfortunately, this is unknown for the wave encountered by the probe. However, as described previously equatorial gravity waves with a phase speed of

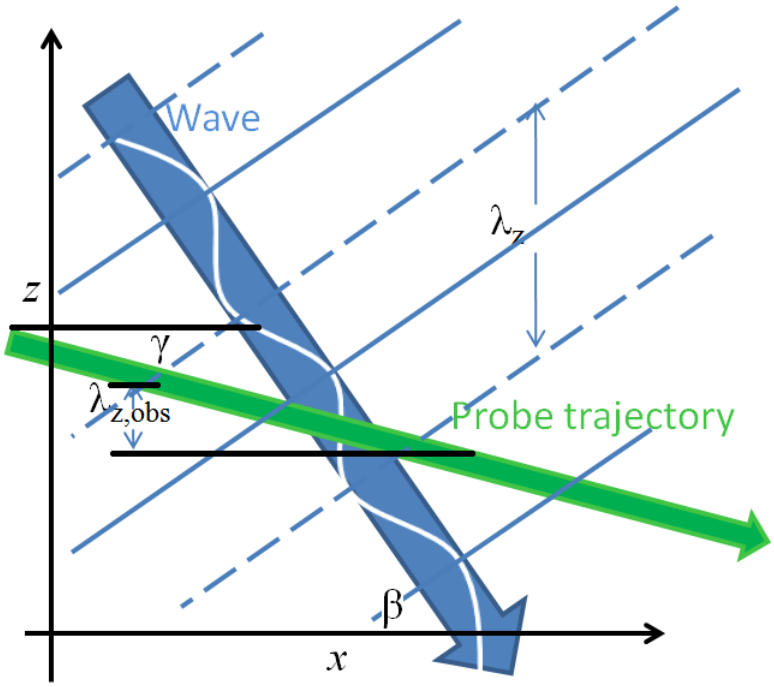

Figure 4.10 – A sketch of the geometry of the wave and probe. As discussed in the main text the waves are assumed to be propagating upwards from the ducting region—that is, the energy flux is positive, $F_z > 0$. We take the wave phase speed to be greater than the wind speed, $I > 0$, as has been observed in equatorial gravity waves on Jupiter (Reuter et al., 2007). So, the wave fronts (shown as solid and broken thin blue lines) move downward, as indicated by the wave vector, the thick blue arrow (Nappo, 2002). The angle made by the wave vector with the horizontal is β. The probe's trajectory, at an angle γ to the horizontal, is shown as the green arrow. It can be seen that the vertical wavelength observed by the probe, $\lambda_{z,obs}$, is different to the actual value λ_z.

about 100 m s^{-1} greater than the winds have been seen in images of Jupiter's clouds returned by New Horizons (Reuter et al., 2007). This value is taken as a typical value and therefore $c = 180$ m s^{-1}. This is consistent with the hypothesis that the waves are driven by convective overshoot in the region below the clouds. In this region the zonal winds have been measured by the DWE on board the probe to be near this speed, ~ 170 m s^{-1} (Atkinson, Pollack, and Seiff, 1998), so a phase speed of this size is plausible. Any variation of c with altitude would be expected to be small, increasing the uncertainty to some degree but not fundamentally changing the profile. This gives the profile for $u_0(z)$ shown in Figure 4.11. The standard deviation shown indicates the variation in the profile given by the various smoothing window sizes considered in constructing $\mathcal{E}$.

The upper part of the DWE profile is shown in red in Figure 4.11. The wind speed at the bottom of the profile derived from the properties of the gravity waves agrees well with that at the top of the DWE profile. The profile shows increasing zonal wind speed with altitude (up to ~ 100 km above the 1 bar level). This implies that the wind speed is a minimum near the cloud-top level. This is similar to what has been observed from studies using the thermal wind equation (Flasar et al., 2004; Simon-Miller et al., 2006). However, in this profile, the high speed wind is not a jet as the zonal wind velocity remains near this level throughout the stratosphere. There are some fluctuations of the order of 20 m s^{-1} in the wind speed in the thermosphere. The Richardson number, given by (2.56), is greater than 1/4 for the entire profile which indicates the flow is stable with respect to the Kelvin-Helmholtz instability.

4.1.4 Implications

Temporal variations in the temperature profile of Jupiter's equatorial stratosphere have been observed to have a period of 4 to 5 years and are therefore known as the quasi-quadrennial oscillation (QQO) (Friedson, 1999; Leovy, Friedson, and Orton, 1991). These oscillations have been linked to variations in the zonal wind observed via cloud-tracking on Jupiter (Simon-Miller et al., 2007). Further, a jet derived using the thermal wind equation applied to data gathered by the Cassini spacecraft in December 2000 and January 2001 and located just north of the equator has also been linked to the QQO (Flasar

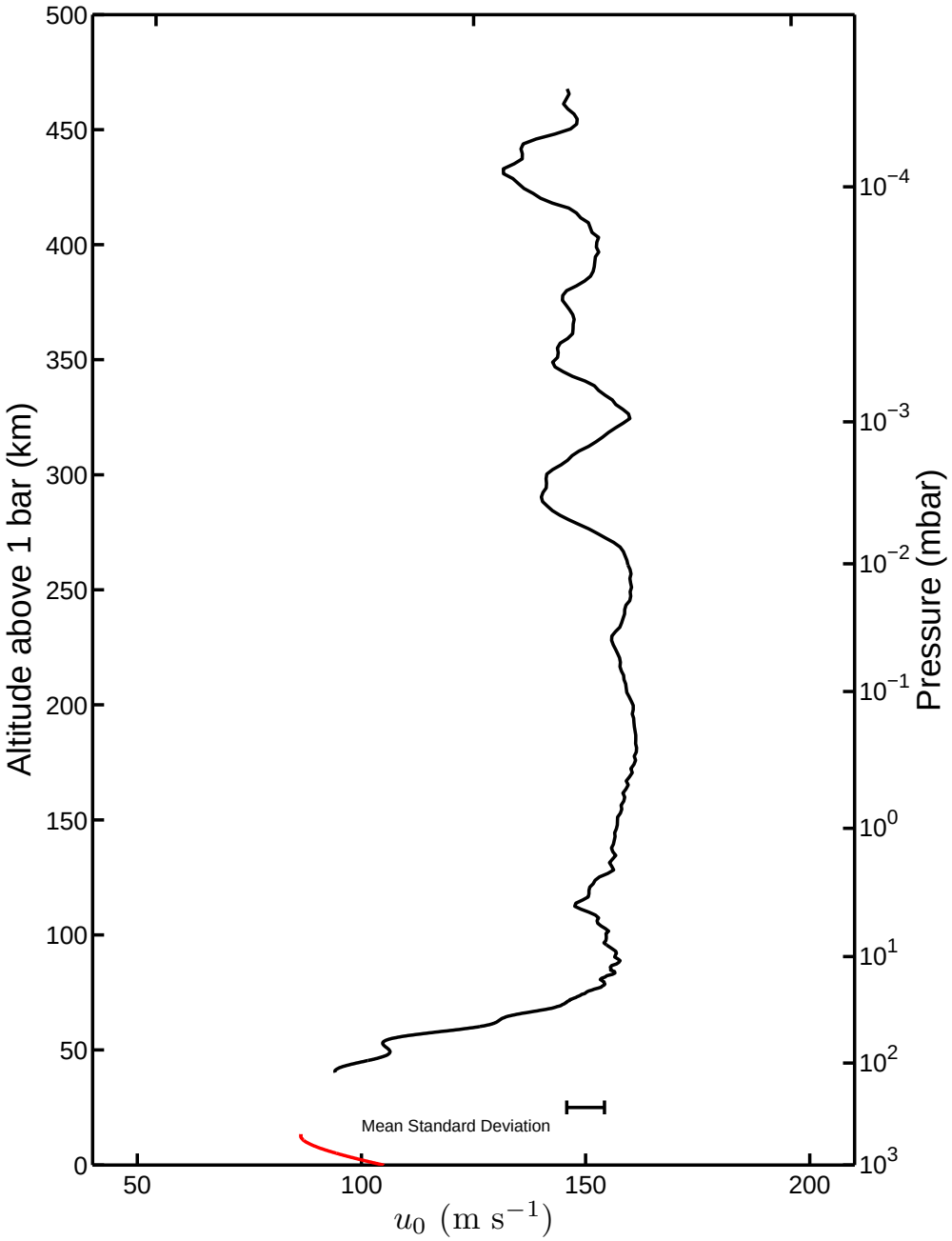

Figure 4.11 – The vertical profile of the background zonal wind speed u_0. The zonal wind is shown (—) with the average standard deviation of the variation across smoothing and periodogram windows indicated. The zonal speed profile found by the Doppler Wind Experiment is shown at the bottom (—) for comparison.

et al., 2004). No such jet is present in the profile presented here. However, a jet of similar magnitude, just south of the equator, has been observed in observations gathered in 1979 (Simon-Miller et al., 2006), suggesting this jet may be oscillating about the equator. The lack of a jet in the profile presented in Figure 4.11 is consistent with such an oscillation, as the jet would be located south of the equator at the time the Galileo probe entered the atmosphere.

The circulation of Jupiter's stratosphere is important for understanding the planet's circulation as a whole. The location of the turbopause is essential for understanding the coupling between Jupiter's upper atmosphere and the circulation in the lower atmosphere. The Juno mission will explore the troposphere of Jupiter to depths of 100 bar or more. This will provide better insight to the source and behaviour of gravity waves in the troposphere, possibly allowing better limits to be derived for the wave-vector angle β in our analysis and the mechanisms for gravity wave generation. The planned Jupiter Icy Moon Explorer (JUICE) mission (Dougherty et al., 2011) will study gravity wave activity and zonal winds in the stratosphere of Jupiter providing a context for these results. These measurements will be taken over an extended period enabling the evolution of this profile to be observed, in addition to improving our understanding of the overall circulation and specific features (e.g., the QQO and any oscillation of its associated jet about the equator).

Chapter 5

Further Work and Conclusion

The study of extrasolar planets has rapidly grown into a mainstream research area over the last decade and a half, since the discovery of 51 Pegasi b. There are many topics within the discipline with thriving communities of researchers. The study of the atmospheric dynamics of these planets is just one of these topics. It is, however, of crucial importance to the discipline as a whole, as the atmospheric dynamics influences the radiation emitted by these planets and are, therefore, crucial to the interpretation of the observations. This thesis has investigated one aspect of these dynamics – internal atmospheric gravity waves. The results of this investigation are summarised below along with an overview of future work to build and extend the results that have been presented in this thesis.

Gravity waves are also a feature of planetary atmospheres within the Solar System. These waves provide a probe to explore the atmospheres within which they propagate, an example of which is described in this thesis. There are other opportunities for similar techniques to be applied, and these are discussed below.

But first some preliminary work on modelling gravitational tides on Jupiter is presented. Planet-scale gravity waves, atmospheric tides, can also affect the circulation of a planet or moon, for example atmospheric tides raised on Titan by Saturn are thought to have a major effect on the moon's tropospheric and stratospheric circulation (Tokano and Neubauer, 2002). In the following section a brief summary of gravitational atmospheric tides on Jupiter is

presented. Also presented is a short review of the performance of the GCM, MITgcm which has been used to simulate the atmospheric tide. It is important to understand the performance of GCMs that have been developed to model conditions found in the Solar System when used to model the very different conditions found on hot EGPs. Without such an understanding it is possible that phenomena that are purely artefacts of the GCM may be presented as physical. A brief discussion of how the modelling of atmospheric tides could be extended to extrasolar planets is included in the review of future work.

5.1 Gravitational Tides on Jupiter

Gravity waves that are of a planetary scale and periodically excited – for example, by the gravitational pull of a satellite – are known as atmospheric tides. In addition to gravitational tides, there are tides that are excited thermally by heating from the parent star. Both mechanisms are present on the Earth, with the solar thermal tide dominating. The effect of the solar tide can be seen in regular variations of the surface atmospheric pressure, especially in the tropics (Chapman and Lindzen, 1970).

The Solar System's giant planets are much further from the Sun than the Earth. Jupiter has a semi-major axis of roughly 5.2 AU, and so thermal forcing plays a much smaller role in generating tides. However, as discussed below, the gravitational potential due to the main satellites of these planets is many times larger than that of the Moon and so gravitational tides may have a significant effect.

In this section we survey the classical (linear) tidal theory, as applied to Jupiter and its satellite Io. The aim of this section is to simulate the tides using a three dimensional GCM. The model used, MITgcm, is described along with a brief summary of the behaviour of MITgcm when simulating test cases from a comparison of GCMs. This work is due to be published in the near future (Polichtchouk et al., in preparation). Finally, the effects of the tides as shown by the simulations are given and possible implications for Jupiter's circulation discussed.

5.1.1 The Classical Theory of Atmospheric Tides Applied to Jupiter

As tides are planetary-scale phenomena the fluid equations used in Chapter 2 to derive the TGE need modification. Specifically, Equations (2.20) are extended to three dimensions and to take account of the rotation of the planet. To simplify the equations obtained, a number of approximations are used, which vary depending on the application. For example, in the terrestrial case the atmosphere is assumed to be thin and the atmosphere is taken to be in hydrostatic balance (Chapman and Lindzen, 1970). However, since Jupiter is a gas planet with no solid surface, these assumptions are not made when developing the tidal equations for the Jupiter–Io system (Ioannou and Lindzen, 1993a). The traditional approximation, which neglects certain Coriolis and metric terms is used. Ioannou and Lindzen (1993b) argue that this is reasonable as the tidal action is largely in the outer part of the planet. Further, the linearisation approximates the atmosphere as static. This is not unreasonable as the tide travels around the planet's equator at approximately 9.6 km s^{-1}, far in excess of Jupiter's maximum wind speed. Indeed, this is hypersonic as the speed of sound in Jupiter's atmosphere is just 0.8 km s^{-1}.

This gives the relevant linearised equations as,

$$\frac{\partial v_1}{\partial t} + 2\omega u_1 \sin\varphi + \frac{1}{r}\frac{\partial P_1}{\partial \varphi} = 0\,, \tag{5.1a}$$

$$\frac{\partial u_1}{\partial t} - 2\omega v_1 \sin\varphi + \frac{1}{r\cos\varphi}\frac{\partial P_1}{\partial \vartheta} = 0\,, \tag{5.1b}$$

$$\rho_0\frac{\partial w_1}{\partial t} + \frac{\partial p_1}{\partial r} + \rho_0\frac{\partial \Omega}{\partial r} - g_0\rho_1 = 0\,, \tag{5.1c}$$

$$\frac{\partial \rho_1}{\partial t} + w_1\frac{\mathrm{d}\rho_0}{\mathrm{d}r} + \rho_0\chi = 0\,, \tag{5.1d}$$

$$\frac{\partial p_1}{\partial t} - c^2\frac{\partial \rho_1}{\partial t} + \rho_0\frac{c^2}{g_0}N^2 w_1 = 0\,, \tag{5.1e}$$

where φ is the latitude; ϑ is the longitude; r is the radial distance; u_1, v_1 and w_1 are the perturbation velocities in the zonal, meridional and radial directions respectively; $P_1 = (p_1/\rho_0)+\Omega$ is the reduced pressure and Ω is the gravitational potential due to Io, given below; $\chi = \nabla\cdot\mathbf{v}$ is the velocity divergence which in

this coordinate system is

$$\chi = \frac{1}{r\cos\varphi}\frac{\partial u_1}{\partial \vartheta} + \frac{1}{r\cos\varphi}\frac{\partial}{\partial\varphi}\left(v_1\cos\varphi\right) + \frac{1}{r^2}\frac{\partial(r^2 w_1)}{\partial r}\,; \tag{5.2}$$

and $c^2 = \gamma p_0/\rho_0$ is the speed of sound.

These equations can be combined, eliminating the horizontal velocities, to give,

$$\chi = \frac{1}{r^2}\frac{\partial(r^2 w)}{\partial r} + \frac{i\sigma}{4\omega^2 r^2}F\left(P_1\right)\,, \tag{5.3}$$

where F is the Laplace tidal operator,

$$F \equiv \frac{1}{\cos\varphi}\frac{\partial}{\partial\varphi}\left(\frac{\cos\varphi}{f^2-\sin^2\varphi}\frac{\partial}{\partial\varphi}\right) - \frac{1}{f^2-\sin^2\varphi}\left(\frac{s}{f}\frac{f^2+\sin^2\varphi}{f^2-\sin^2\varphi} + \frac{s^2}{\cos^2\varphi}\right)\,, \tag{5.4}$$

where s is the zonal wavenumber and $f = \sigma/(2\omega)$, where ω is the rotational angular velocity of Jupiter and σ is the tidal angular velocity given by $2(\omega - \omega_{Io})$, where ω_{Io} is the orbital angular velocity of Io; the orbital angular velocity of Jupiter is neglected as it is small (Ioannou and Lindzen, 1993a). This equation is separable, giving an equation for the meridional structure. This is the eigenproblem,

$$F\left(\Theta_n\right) = \frac{4r^2\omega^2}{gh_n}\Theta_n \tag{5.5}$$

where the eigenfunctions Θ_n are Hough modes and h_n is known as the equivalent depth. Hough modes are sums of associated Legendre polynomials $P_{m,s}$,

$$\Theta_n = \sum_{m=s}^{\infty} C_{n,m}P_{m,s}\left(\cos\varphi\right)\,, \tag{5.6}$$

where the coefficients $C_{n,m}$ are obtained from recurrence relations derived by substituting Equation 5.6 into Equation 5.5 (see Chapman and Lindzen, 1970, for details). Selected Hough modes for the Jupiter–Io system are given in Figure 5.1. It is clear from Figure 5.1 that the latitude of 50° has a special role in the Hough modes of this system. This is the critical latitude, the latitude where the period of the forcing is equal to the inertial period. It is given by the angle $\arcsin f$. Note that modes with negative equivalent depth contribute poleward of the critical latitude and modes with positive equivalent depth contribute equatorward of the critical latitude.

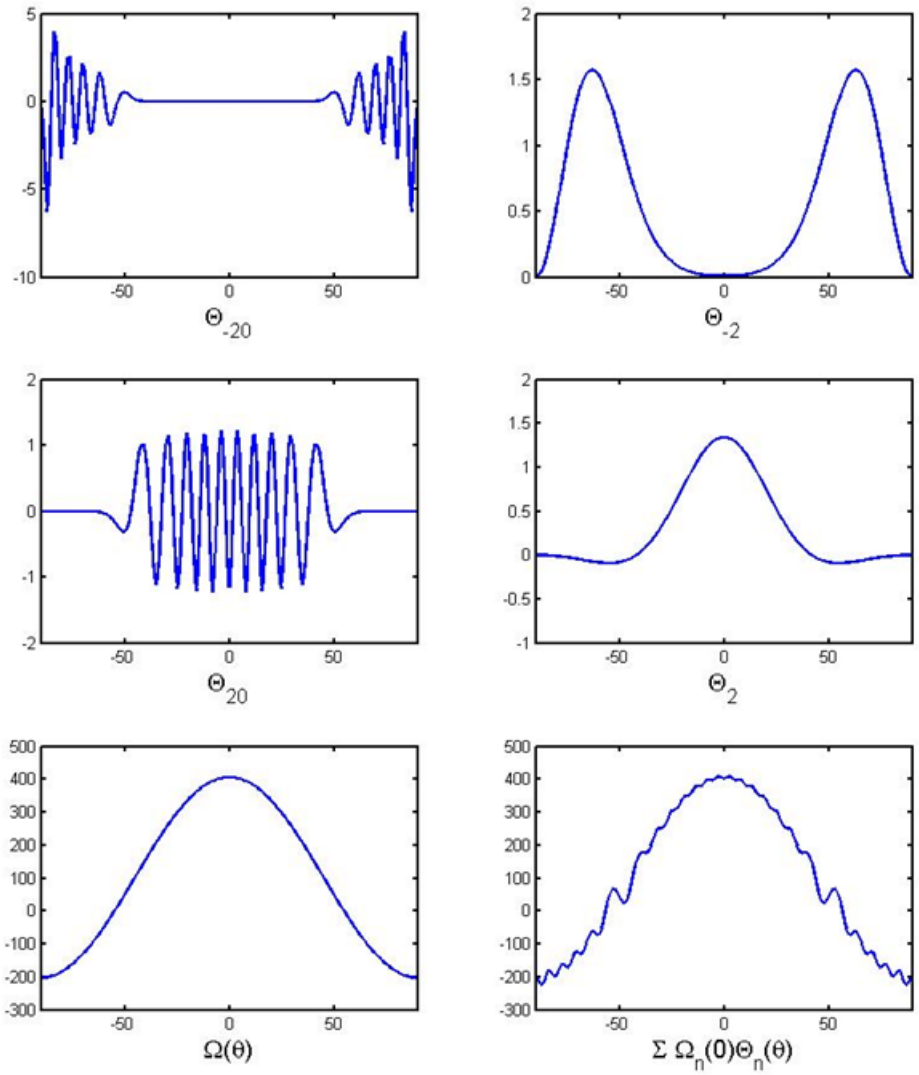

Figure 5.1 – Example Hough modes from the Jupiter–Io system. Note that Hough modes with negative indices – i.e., those with negative equivalent depths, are evanescent equatorward of the critical latitude of 49.9°, whereas those with positive equivalent depths are evanescent poleward of the critical latitude. The potential as given by equation (5.7) with $r = a$ and $\lambda = 0$ is shown in the bottom left subfigure; and, for comparison, in the bottom right subfigure is the potential obtained by summing Hough modes with indices from -20 to 28.

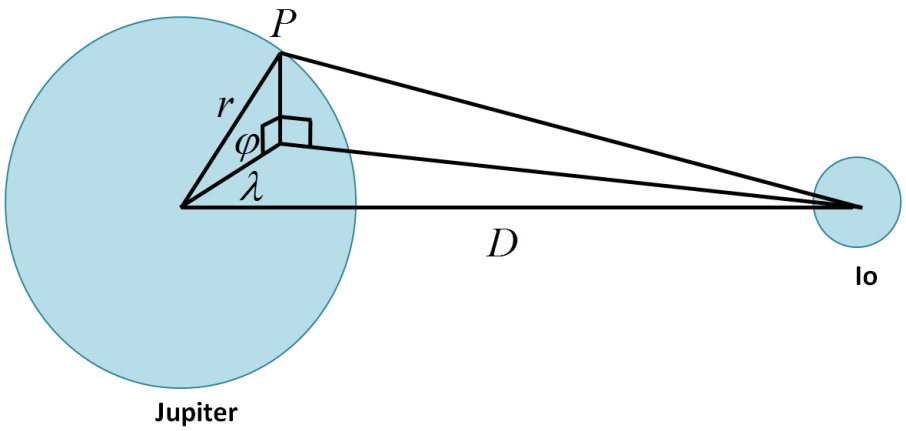

Figure 5.2 – A sketch of the geometry of the Jupiter and Io system. The tidal potential at point P can be calculated using 5.7. Here D is the distance between the centres of Io and Jupiter, r is the radial distance of P, λ is the difference between the longitude of P and the longitude of the sub-Io point and φ is the latitude of P.

The geometry of the Jupiter–Io system ($f = 0.766$) is sketched in Figure 5.2. Here it is assumed that the orbit of Io lies in the plane of Jupiter's equator. This is a very good approximation, as Io's inclination is just 0.05°. It is also assumed that Jupiter is a spherical planet, which is not as good an approximation, as Jupiter is an oblate spheroid with a flattening of approximately 0.06. This geometry gives the potential as,

$$\Omega\left(\lambda, \varphi, r\right) = -\frac{3}{2}\frac{GM_{Io}r^2}{D^3}\left(\frac{1}{3} - \cos^2\lambda\cos^2\varphi\right) , \tag{5.7}$$

where λ is the difference between the longitude of the sub-Io point and the longitude of P, G is the gravitational constant, M_{Io} is the mass of Io and r is the radial distance of P from the centre of the planet. The potential $\Omega(0, \varphi, a)$ is shown in the bottom left subfigure of Figure 5.1. However, in order to use the potential with the vertical structure equation, described below, it has to be decomposed into its components given by,

$$\Omega\left(0, \varphi, r\right) = \frac{r^2}{a^2}\sum_{-\infty}^{\infty}\Omega_n\Theta_n\,. \tag{5.8}$$

This sum for $-20 \leq n \leq 28$ (the same as used in Ioannou and Lindzen (1993a) for ease of comparison) with $r = a$ is shown in the bottom right subfigure of Figure 5.1. The values of Ω_n are based on Ioannou and Lindzen (1993a), but note that the values given there are a factor of 2 too small. The calculations given here have corrected for that. The potential at the surface of Jupiter is shown in Figure 5.3. The semidiurnal nature of the potential and, thus, the tide can be seen. The potential gives rise to forcing that drives the tide as can be seen in the vertical structure equation,

$$\xi_n = \frac{1}{\sigma^2 - N^2}\left(\frac{\mathrm{d}P_n}{\mathrm{d}r} - \frac{N^2}{g_0}P_n + \frac{N^2 r^2}{g_0 a^2}\Omega_n\right), \tag{5.9a}$$

$$\frac{1}{r^2}\frac{\mathrm{d}}{\mathrm{d}r}\left(r^2\xi_n\right) + \left(\frac{1}{c^2} - \frac{a^2}{g h_n r^2}\right)P_n - \frac{g_0}{c^2}\xi_n = \frac{r^2}{c^2 a^2}\Omega_n\,, \tag{5.9b}$$

where $\xi_n = w_n/i\sigma$ is the radial displacement. Solving the vertical structure equation gives the variation of radial displacement with radial distance and latitude. As with small scale gravity waves the stratification of the fluid is important in determining the behaviour of the tide. Stratification is required for Hough modes with positive equivalent depth to propagate. So, we see in Figure 5.4, where the fluid is modelled as neutrally buoyant (i.e., $N = 0$), the radial displacement due to the tide is generally small. However, in models where the *Brunt–Väisälä* frequency is positive, such as that shown in Figure 5.5, the tide propagates causing large radial displacements. But, as can be clearly seen in these figures, stratification is not the only factor affecting the behaviour of the tide. In the outer shell of the planet, where $N > \sigma$, the tide only propagates equatorward of the critical latitude. Conversely, in the inner region where $N < \sigma$ the tide propagates poleward of the critical latitude.

5.1.2 MITgcm

The tidal simulation was implemented using MITgcm. This GCM is described in Adcroft et al. (2011), but a brief summary is given here. The GCM uses a finite-volume approach to solve the primitive equations. It is a very flexible model allowing the relaxation of many of the usual assumptions (such as a thin atmosphere and hydrostatic balance). It also allows horizontal discretisations beyond the usual geographical (latitude/longitude) grid. Specifically it allows

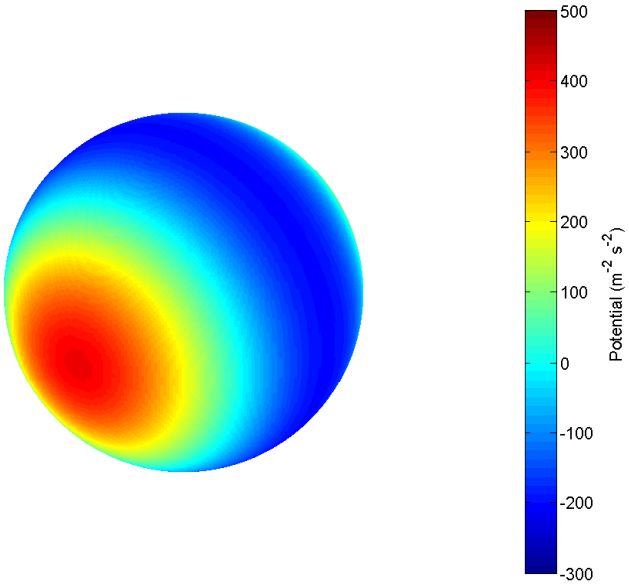

Figure 5.3 – The gravitational tidal potential due to Io at Jupiter's cloud layer. Note that the potential is symmetric, with identical structure on the hemisphere toward Io and the hemisphere facing away. This leads to the tides being semidiurnal.

the use of a cubed-sphere grid as shown in Figure 5.6. There is can be seen that the grid consists of a cube, where each face has been gridded, conformally mapped onto a sphere. The advantages this brings includes the elimination of the problem of meridians, and therefore grid-points, becoming physically close in the high latitudes near the pole; thus a polar filter is not required. Also fewer grid points are required to cover the sphere for a given resolution than is required by a geographical grid.

However, the corners do introduce some issues. This has been demonstrated in the findings of a recent GCM comparison study (Polichtchouk et al., in preparation). The exercise ran three idealised test cases with parameters relevant to a close-in tidally locked giant planet; a balanced mid-latitude jet, the same jet but with a small temperature perturbation and an initially at rest atmosphere forced with a Newtonian thermal relaxation. A cross-section of the initial conditions of the mid-latitude jet case, based on a similar test case using terrestrial parameters described in Polvani, Scott, and Thomas (2004), is shown in Figure 5.7. Detailed analysis of these cases and cross-GCM comparisons were carried out using norms described in Jablonowski and Williamson

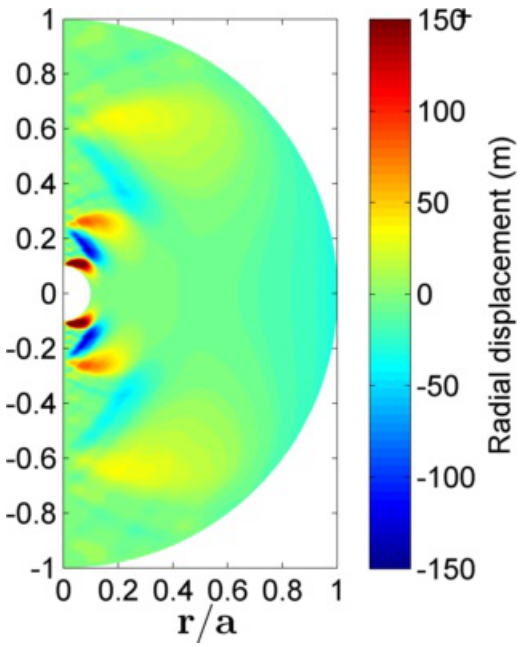

Figure 5.4 – This shows the tides on a Jupiter where the interior is neutral – i.e, the *Brunt–Väisälä* frequency is zero. The colour shows the amount of radial displacement due to the tide. The amplitude of the tide is generally much smaller than that for the case, where the interior is stratified, shown in Figure 5.5. Note that the waves that can be seen poleward of the critical latitude are inertial waves. However, as the calculation uses the traditional approximation, which neglects part of the Coriolis force, these waves are unphysical.

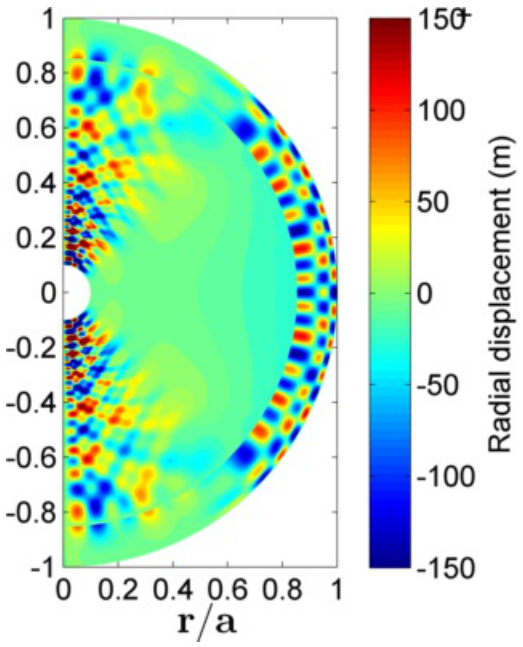

Figure 5.5 – This shows the tides on a Jupiter where the interior is stratified – i.e., the *Brunt–Väisälä* frequency is greater than zero but decreases as r, the radial distance, decreases. The profile is based on Ioannou and Lindzen (1993b) and illustrates the structure of the tide on a giant planet with stratified interior. The colour shows the amount of radial displacement due to the tide. Note that the amplitude of the tide is generally much larger than that for the case where the interior is neutral, as shown in Figure 5.4. Further, the tide has six zones. There is an outer region, where $r/a \gtrsim 0.85$. Here the *Brunt–Väisälä* frequency is greater than the forcing frequency σ. This region is further divided into the two areas poleward of the critical latitude (where the tide is minimal) and the equatorward region (where the tide propagates). Interestingly, in the interior region, where $r/a \lesssim 0.85$, the reverse occurs with the tide propagating in the two poleward regions but evanescent in the equatorward region.

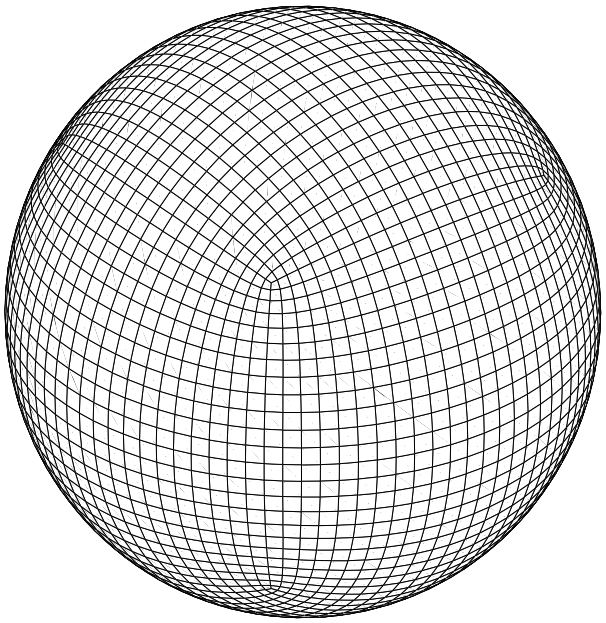

Figure 5.6 – This is an example cubed sphere grid for use with MITgcm. It improves upon the more standard latitude longitude grid in not requiring a polar filter to counteract the effect of meridians becoming physically closer near to the poles, it also uses less grid point to cover the grid for a roughly equivalent resolution. However, as discussed in the text the sphere's "corners" do introduce artefacts that make this grid unsuitable for some work. See Figure 5.8 for an example.

(2006).

However, to illustrate the issues with the cubed-sphere grid, it is only necessary to view the output of the first two simulations. These are shown in Figure 5.8, which shows the temperature field at the 975 mb level for the northern hemisphere. The unperturbed balanced jet should remain unchanged as it is a solution of the fluid equations. To test the GCM the unperturbed balanced jet simulation is undertaken without dissipation and the deviation from the initial condition that developed over time measured. Little or no change would be expected. This can be seen in Figures 5.8 (a) and (b) which are the outputs from a simulation using a geographical grid.

However, the jet is an unstable solution of the equations and a small perturbation will trigger the baroclinic instability, leading to a wave in the temperature field. When using the cubed-sphere grid, as shown in Figures 5.8 (c) and (d), this wave appears with wavenumber four. This demonstrates that the cubed-sphere grid introduces perturbations. The output is noisy due to the lack of dissipation in the test case.

Where the initial set-up includes a small perturbation in the temperature field, a baroclinic wave is excited which can be seen in the temperature field. This can be seen when using the geographical grid as shown in Figures 5.8 (e) and (f). When using the cubed-sphere grid, the baroclinic wave is still excited, it is superimposed on the wavenumber four disturbance coming from the corners. This is shown in Figures 5.8 (g) and (h). The figure here is much less noisy as dissipation is included in this test-case.

5.1.3 Jupiter's Circulation

As discussed in Chapter 4 the circulation on Jupiter is broadly zonal. There is a series of retrograde and prograde jets that is associated with Jupiter's cloud deck and its banded appearance. The origin of this character is an area of active academic debate. There are two categories of proposed mechanisms. The first set of mechanisms can be characterised as "deep" models (Busse, 1976; Heimpel, Aurnou, and Wicht, 2005, e.g.,). These depend on the Taylor-Proudman effect (e.g., Vallis, 2006), which states that in a fast rotating barotropic fluid the flow is constant in cylinders centred on the axis of rotation. Simply put,

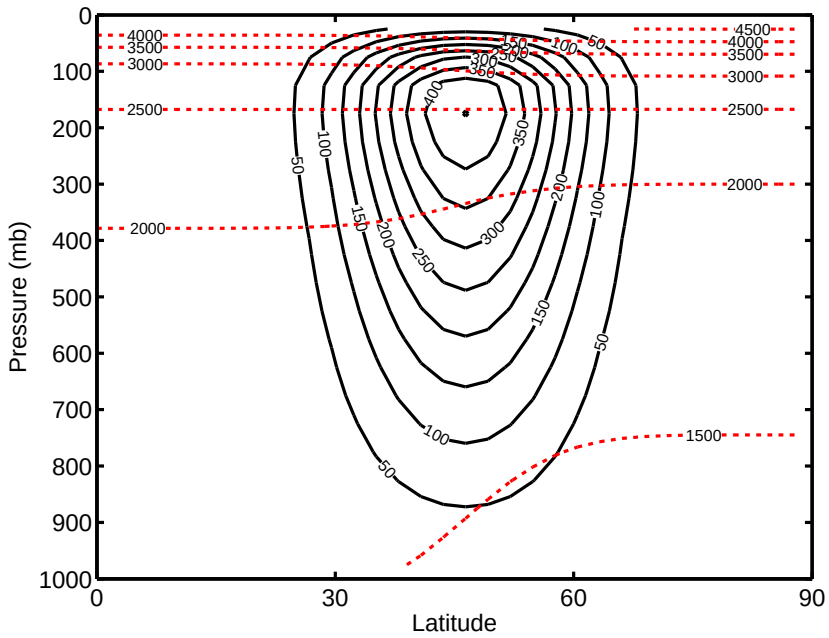

Figure 5.7 – The figure shows the initial conditions for the balanced mid-latitude jet test case. The solid black lines (—) shows the zonal wind. The dashed red line (- - -) shows the potential temperature.

these theories hold that Jupiter consists of a series of rotating cylinders and the jets are the manifestation of these cylinders at the planet's surface. These models generally give a broad prograde jet at the equator but a smaller number of jets than observed. The other category of models are "shallow". Here, the jets form in the weather layer. An initially turbulent layer modelled using the shallow-water equations will evolve into a series of jets (Cho and Polvani, 1996a,b). However, "shallow" models have failed to produce a prograde jet at the equator. A more recent "shallow" model has demonstrated the ability to produce a prograde equatorial jet, by including radiative relaxation in the model (Scott and Polvani, 2008).

A third approach has been proposed where the tides, excited by the satellites, break in the atmosphere depositing momentum into the flow (Ioannou and Lindzen, 1993a, 1994). The meridional pattern of this deposition at the cloud level is somewhat suggestive of the banded structure of Jupiter's clouds, with alternating regions of prograde and retrograde momentum deposition. However, the largest accelerations are produced away from the equator at latitudes of approximately 15°, 25° and 40°. This, perhaps, would mean no jet at the equator via this method. A further issue is that for the tides to have this

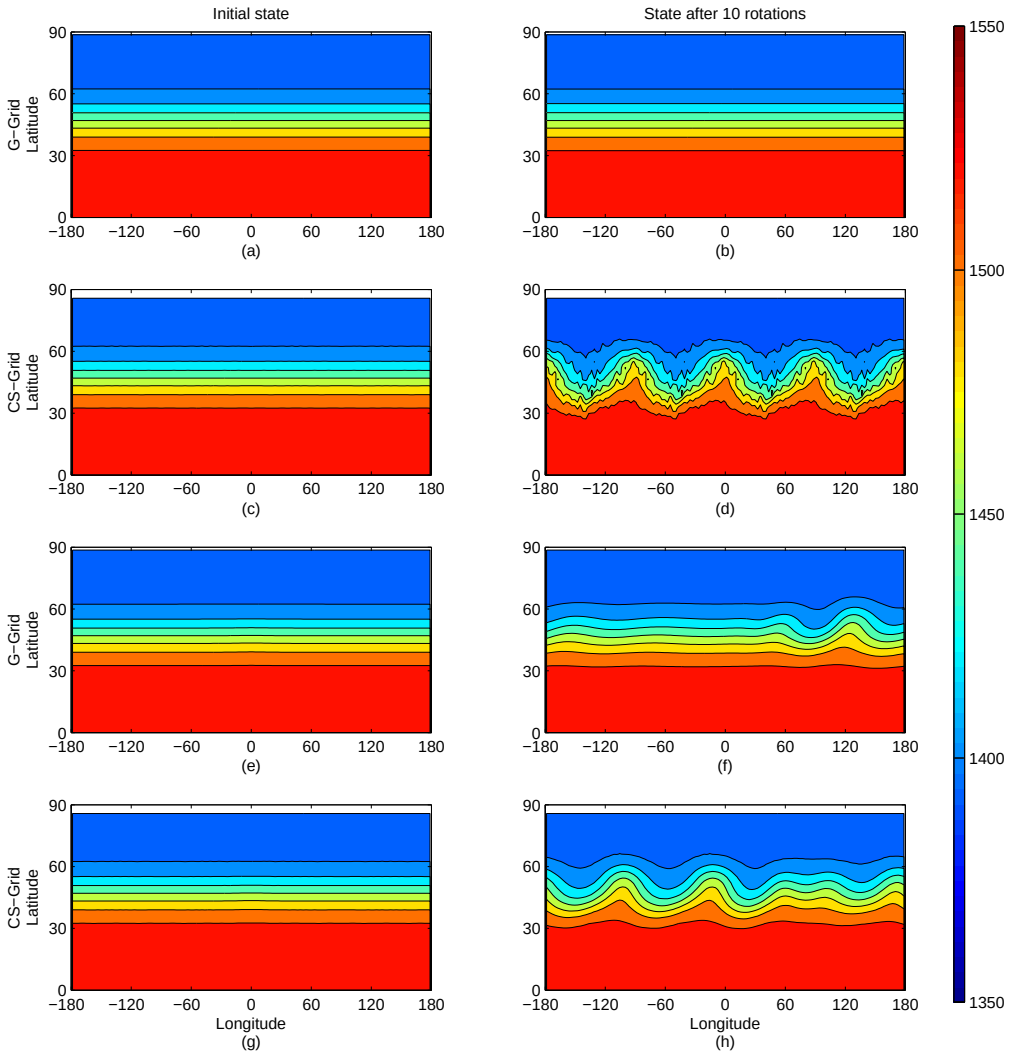

Figure 5.8 – Comparison of balanced jet test case simulations using both the geographical grid (G-grid) and cubed-sphere grid (CS-grid) available in MITgcm. Each subfigure shows the temperature field at 975 mb. The left column shows the initial state, the right column shows the situation after 10 rotations of the planet. In the lower four subfigures a small perturbation in the temperature field has been used to trigger a baroclinic instability. In subfigures (a) and (b) there is no visible change, as expected. However, in subfigures (c) and (d) the field does evolve with a wavenumber 4 pattern. This shows how perturbations from the CS-grid corners have driven the setup away from balance triggering the instability. The figure is noisy as the setup for this text case specifies that no dissipation should be used. In sub-figures (e) and (f) a small perturbation in the temperature field at the prime meridian has triggered a wave via the baroclinic instability. Sub-figures (g) and (h) show how the instability grows when using the CS-grid. While this evolution is clearly different to that in subfigure (d) there are still spurious features with a wavenumber of 4.

effect the interior of Jupiter would need to be stratified. Whilst some evidence for regions of stratification exists in the region explored by the *Galileo* probe (Magalhães, Seiff, and Young, 2002) this is is still very shallow compared to the depths that stratification is assumed in Ioannou and Lindzen (1993a).

5.1.4 Simulation of Atmospheric Tides on Jupiter

In preparation for future simulation of gravitational tides on close-in giant planets, discussed in more detail in Chapter 5, a simulation using MITgcm of gravitational tides in Jupiter's atmosphere was undertaken. MITgcm was used as it has built in to the code the ability to solve the fluid equations without assuming hydrostatic balance or assume that the fluid is of negligible thickness compared with the radius of the planet. However, as this simulation is of tides in Jupiter's atmosphere, the simulation discussed here does not relax these approximations.

The tide is simulated taking the gradient of the potential in the longitudinal and latitudinal directions and using these accelerations to force the zonal and meridional momentum equations. The fluid is discretised into 5 layers above the 1 bar level. A zonal filter is used poleward of 45° to compensate for the reduction in separation of the meridians that occurs there. Further, an order 16 Shapiro filter (Shapiro, 1970) is used to remove grid scale noise. The fluid begins at rest. The timestep used is 67 s and the simulation runs for 2000 semidiurnal tides – that is, 1000 times the period it takes for Io to return to the same position in Jupiter's sky; a total of 46632000 s (approximately 1300 rotations of Jupiter).

Figure 5.9 shows the zonal velocity field after 1000 and 2000 tides. The semidiurnal character of the tide can be seen. The pattern of the flow is seen to be the same at both times showing that the simulation has converged. Instantaneous zonal flows of less than 1 m s^{-1} are excited by the tide. Figure 5.10 shows the zonally averaged zonal wind after 2000 tides (i.e., the zonal average of the tide shown in Figure 5.9 (b). Figure 5.11 shows the average acceleration of the flow over the period between Figure 5.9 (a) and Figure 5.9 (b). The flow generated is slow at just 0.03 m s^{-1}, and the accelerations are very small at just a few microns per second per rotation, it is unlikely that these will have any effect on Jupiter's circulation.

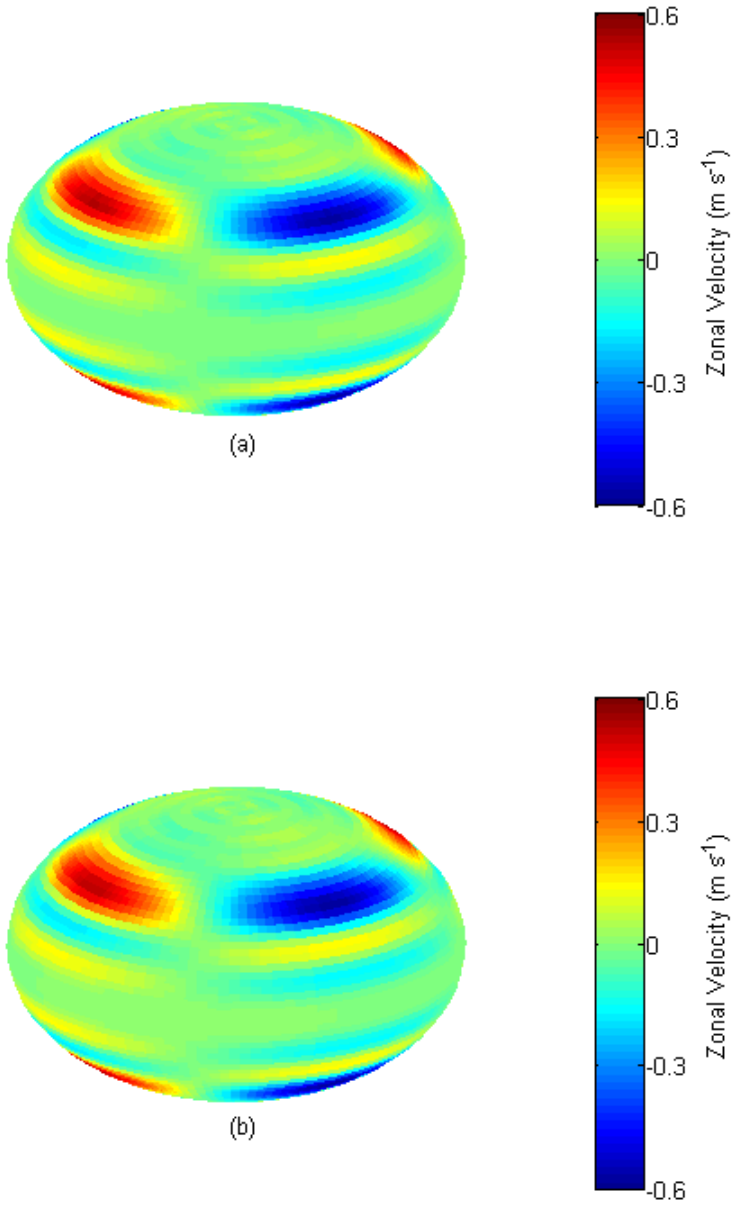

Figure 5.9 – The zonal velocity field after (a) 1000 tides and (b) 2000 tides. The similarity of the two fields shows that the solution has converged.

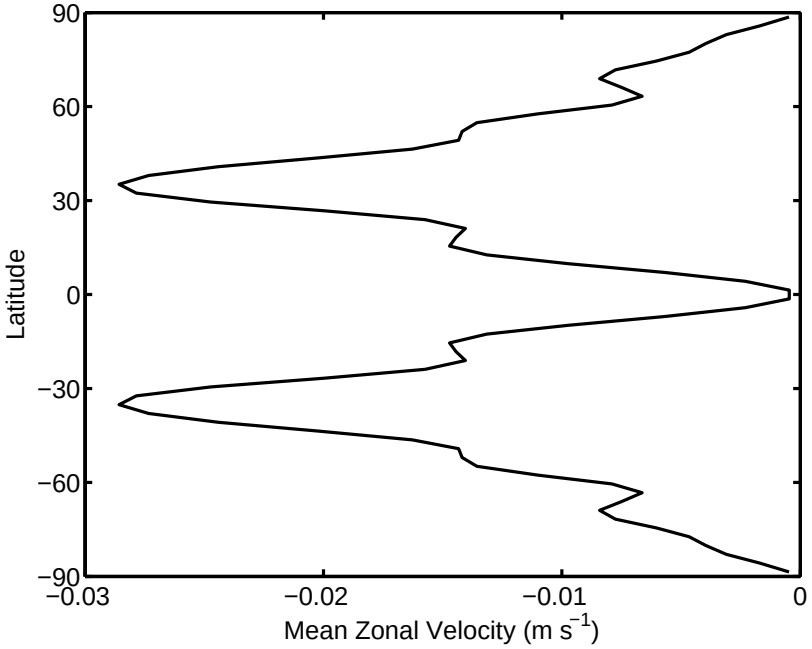

Figure 5.10 – The mean zonal velocity at the 500 mb level after 2000 tides. As can be seen, the effect of the tide is to cause a mean retrograde flow in the mid-latitudes.

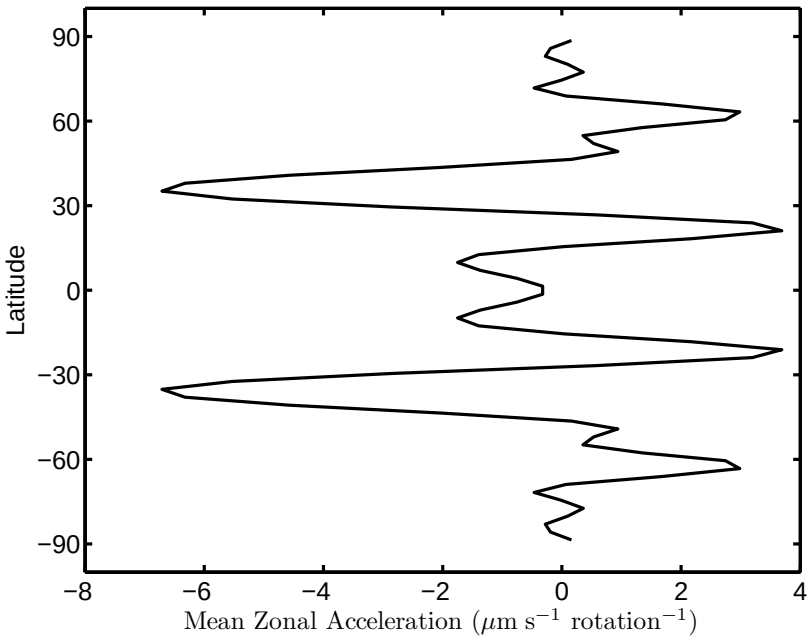

Figure 5.11 – The mean zonal acceleration at the 500 mb level. As can be seen, the accelerations are very small, a change in the flow velocity of just a few microns per second per rotation. Such accelerations are insignificant compared to accelerations from other sources.

5.2 Summary

Although the details of the atmospheric circulation on EGPs are still much debated, some basic features (such as a low number of jets) are becoming accepted. The work here, whilst using atmospheric profiles based on what is believed to be a typical EGP circulation, does not depend on a knowledge of the exact circulation. For example, should future observations identify planets with strong retrograde equatorial jets, the results regarding ducting in a jet would still be applicable.

In Chapter 3 it was demonstrated that gravity waves with relatively modest forcing, for a close-in highly irradiated planet, can have major effects on the mean flow in the lower to middle atmosphere. In the presence of a jet waves with a phase speed that is less than the maximum flow speed of the jet will eventually encounter a critical layer. The wave will dissipate at such an encounter leading to momentum and heat being deposited into the flow. This can lead to an acceleration of the flow such that, over the period of a rotation, the flow speed can be significantly changed.

Even in the absence of critical layers waves still deposit momentum and heat via saturation. Here the wave grows so large that locally the wave becomes convectively unstable and thus deposits momentum into the flow. Again, large accelerations and heating can result from this. The waves grow with altitude, due to the decreasing density. The stratified region of the atmosphere on hot EGPs is expected to be deeper than those seen on giant planets in the Solar System. Thus, waves can be excited deeper within the atmosphere allowing them to grow large and saturate at quite modest altitudes. Thus, significant gravity wave induced accelerations and heating can occur at quite high pressures.

These processes, however, act as a filter ensuring that such waves do not reach the thermosphere or higher regions of the atmosphere. For waves excited at 1-scale height above the 1 bar level, only waves with smaller forcing – equivalent to terrestrial heating rates – can penetrate high into the atmosphere. Here, rather than saturating they are dissipated by viscosity, which becomes important in the thermosphere. Again, this leads to significant accelerations in the flow.

Via this vertical propagation, gravity waves provide a mechanism for coupling vertically separated layers of the atmosphere. However, in addition to this, gravity waves provide a means for the horizontal coupling of regions. This is an important function on tidally locked EGPs, as they are not zonally symmetric. Thus, any means of reducing the inhomogeneity between the day and night sides may play a significant role in the atmospheric dynamics. Parametrisations of gravity wave effects generally assume vertical propagation. Therefore, new parametrisations need to be developed for use in GCM simulations of close-in EGPs.

In Chapter 4 the theory of gravity waves is used to interpret data obtained by the Galileo probe during its entry and descent into Jupiter's atmosphere. The data gathered provided temperature profiles from Jupiter's thermosphere, through the stratosphere and into the troposphere. The profiles, through wave-like perturbations superimposed on a more slowly changing background, indicate that gravity waves, of many different wavelengths, propagate through the atmosphere, especially through the stratosphere. The energy density map, derived from these perturbations, recovers waves that have been previously identified and identifies further waves in the region analysed. However, the energy density in shorter wave-length waves grows in the lower thermosphere and then falls to a low level. This indicates the existence of a turbopause at around 400 km above the 1-bar level.

The number and energy density of the longer wavelength waves varies with height, indicating that the waves are suffering dissipation and regrowth as they propagate upwards. This is evidence of saturation, even perhaps of encounters with critical layers. Crucially, it is possible to identify the variation of vertical wavenumber with altitude. As the vertical wavenumber variation depends upon the properties of the atmosphere, especially the *Brunt–Väisälä* frequency and intrinsic phase speed, knowing the properties of the atmosphere it is possible to deduce the vertical profile of the zonal wind.

The analysis presented here shows that the zonal flow throughout the stratosphere is fast, at about 150 m s^{-1}, at the probe entry site. There is a minimum of about 100 m s^{-1} below the 50 km level. The Jupiter Icy Moon Explorer (JUICE) mission was recently selected by ESA to be part of of its Cosmic Vision programme and will launch in 2022. Despite its name the mission will, alongside Jupiter's moons, study Jupiter's atmosphere providing conformation

of these fast equatorial stratospheric winds.

5.3 Future Work

The exploration of the behaviour of gravity waves on hot EGPs presented here is not complete. The mechanisms for dissipation need to be extended to include, for example, ion drag. High energy irradiation of EGPs by extreme ultraviolet from the planet's star can peak at around the 10^{-6}mbar level and be quite extensive stretching across around 15 H_p. This may be even lower for stars that radiate X-rays strongly (Koskinen et al., 2010). In these regions ionisation will be important and its effects on the flow, via ion-drag, need to be included.

The mechanisms via which gravity waves are excited also need to be explored further. As discussed above, this thesis has assumed thermal forcing; but, this is not the only mechanism that can be reasonably imagined. Convective overshoot from the interior of the planet can be continually agitating the bottom of the radiative envelope, causing waves to be produced. In order to model this an understanding of the likely behaviour of the planet's interior is required. As this is still a topic of debate for Jupiter it is likely to be some time before a consensus is reached.

In Chapter 4 gravity waves identified in archived data were used to analyse the atmosphere of Jupiter. A similar analysis of the temperature data the Huygens probe gathered while it descended through Titan's atmosphere may well provide extra insight and supplement the wind profile obtained through the probe's DWE.

Atmospheric tides on EGPs will also prove to be a fertile research area. For unsynchronised planets thermal and gravitational tides will be present. Thermal tides have been explored (Gu and Ogilvie, 2009). A similar exploration of gravitational tides would be useful. Such studies of tides should be extended by including the mean flow of the planet's atmosphere. In the classical theory the mean flow is assumed to be negligible; but, on extrasolar planets, some studies have found very fast flows. Therefore, this assumption may not be appropriate. Such tides can be explored using a GCM. However, due to the large depth of the radiative envelope on such planets, the GCM will need

to be capable of solving equations that do not assume hydrostasy or a thin atmosphere.

Appendices

Appendix A

Abbreviations and Acronyms

ASI Atmospheric Structure Instrument

DWE Doppler Wind Experiment

EGP extrasolar giant planet

GCM general circulation model

QBO quasi-biennial oscillation

QQO quasi-quadrennial oscillation

TGE Taylor-Goldstein equation

WKB Wentzel–Kramers–Brillouin

Bibliography

Achilleos, N., S. Miller, J. Tennyson, A. D. Aylward, I. Mueller-Wodarg, and D. Rees (1998), "JIM: A time-dependent, three-dimensional model of Jupiter's thermosphere and ionosphere", *Journal of Geophysical Research* 103, pp. 20089–20112.

Adcroft, A., S. Dutkiewicz, D. Ferreira, P. Heimbach, O. Jahn, G. Maze, D. Menemenlis, and A. Molod (2011), "MITgcm User Manual".

Andrews, D. L. T., J. R. Holton, and C. B. Leovy (1987), *Middle Atmosphere Dynamics*, Academic Press.

Arregi, J., J. F. Rojas, R. Hueso, and A. Sánchez-Lavega (2009), "Gravity waves in Jupiter's equatorial clouds observed by the Galileo orbiter", *Icarus* 202, pp. 358–360.

Atkinson, D. H., J. B. Pollack, and A. Seiff (1998), "The Galileo Probe Doppler Wind Experiment: Measurement of the deep zonal winds on Jupiter", *Journal of Geophysical Research* 103, pp. 22911–22928.

Baldwin, M. P. et al. (2001), "The Quasi-Biennial Oscillation", *Reviews of Geophysics* 39, pp. 179–229.

Batchelor, G. (1967), *An Introduction to Fluid Dynamics*, Cambridge University Press.

Baum, W. A. and A. D. Code (1953), "A Photometric Observation of the occultation of σ Arietis by Jupiter", *The Astronomical Journal* 58, pp. 108–112.

Bender, C. M. and S. A. Orszag (1999), *Advanced Mathematical Methods for Scientists and Engineers. I: Asymptotic Methods and Perturbation Theory*, Springer-Verlag.

Bond, I . A. et al. (2004), "OGLE 2003-BLG-235/MOA 2003-BLG-53: A Planetary Microlensing Event", *The Astrophysical Journal* 606, pp. L155–L158.

Booker, J. R. and F. P. Bretherton (1967), "The Critical Layer for Internal Gravity Waves in a Shear Flow", *Journal of Fluid Mechanics* 27, pp. 513–539.

Burrows, A., J. Budaj, and I. Hubeny (2008), "Theoretical Spectra and Light Curves of Close-in Extrasolar Giant Planets and Comparison with Data", *The Astrophysical Journal* 678, pp. 1436–1457.

Busse, F.H. (1976), "A Simple Model of Convection in the Jovian atmosphere", *Icarus* 29, pp. 255–260.

Chapman, S. and R. S. Lindzen (1970), *Atmospheric Tides Thermal and Gravitational*.

Charbonneau, D., T. M. Brown, R. W. Noyes, and R. L. Gilliland (2002), "Detection of an Extrasolar Planet Atmosphere", *The Astrophysical Journal* 568, pp. 377–384.

Cho, J. Y-K. (2008), "Atmospheric Dynamics of Tidally Synchronized Extrasolar Planets.", *Philosophical Transactions. Series A, Mathematical, Physical, and Engineering Sciences* 366, pp. 4477–4488.

Cho, J. Y-K. and L. M. Polvani (1996a), "The emergence of jets and vortices in freely evolving, shallow-water turbulence on a sphere", *Physics of Fluids* 8, pp. 1531–1552.

Cho, J. Y-K. and L. M. Polvani (1996b), "The Morphogenesis of Bands and Zonal Winds in the Atmospheres on the Giant Outer Planets", *Science* 273, pp. 335–337.

Cho, J. Y-K., K. Menou, B. M. S. Hansen, and S. Seager (2003), "The Changing Face of the Extrasolar Giant Planet HD 209458b", *The Astrophysical Journal* 587, pp. L117–L120.

Cho, J. Y-K., K. Menou, B. M. S. Hansen, and S. Seager (2008), "Atmospheric Circulation of Close-in Extrasolar Giant Planets. I. Global, Barotropic, Adiabatic Simulations", *The Astrophysical Journal* 675, pp. 817–845.

Collins, W. D. et al. (2004), "Description of the NCAR Community Atmosphere Model (CAM 3.0)", Boulder, Colorado, USA.

Cooper, C. S. and A. P. Showman (2005), "Dynamic Meteorology at the Photosphere of HD 209458b", *The Astrophysical Journal* 629, pp. L45–L48.

Creasey, J. E., J. M. Forbes, and G. M. Keating (2006), "Density variability at scales typical of gravity waves observed in Mars' thermosphere by the MGS accelerometer", *Geophysical Research Letters* 33, pp. 1–5.

Crossfield, I. J. M., B. M. S. Hansen, J. Harrington, J. Y-K. Cho, D. Deming, K. Menou, and S. Seager (2010), "A New 24 μm Phase Curve for υ Andromedae b", *The Astrophysical Journal* 723, pp. 1436–1446.

Dobbs-Dixon, I., A. Cumming, and D. N. C. Lin (2010), "Radiative Hydrodynamic Simulations of HD209458b: Temporal Variability", *The Astrophysical Journal* 710, pp. 1395–1407.

Dougherty, M. et al. (2011), "JUICE: Exploring the emergence of habitable worlds around gas giants".

Durran, D. R. (1989), "Improving the Anelastic Approximation", *Journal of the Atmospheric Sciences* 46, pp. 1453–1461.

Durran, D. R. (1998), *Numerical Methods for Wave Equations in Geophysical Fluid Dynamics*, Springer-Verlag.

Eliassen, A. and E. Palm (1960), "On the Transfer of Energy in Stationary Mountain Waves.", *Geofysiske Publikasjoner* 22, pp. 1–23.

Elliot, J. L. and C. B. Olkin (1996), "Probing Planetary Atmospheres with Stellar Occultations", *Annual Review of Earth and Planetary Sciences* 24, pp. 89–123.

Festou, M. C., S. K. Atreya, T. M. Donahue, B. R. Sandel, D. E. Shemansky, and A. L. Broadfoot (1981), "Composition and Thermal Profiles of the Jovian Upper Atmosphere Determined by the Voyager Ultraviolet Stellar Occultation Experiment", *Journal of Geophysical Research* 86, pp. 5715–5725.

Flasar, F. M. and P. J. Gierasch (1986), "Mesoscale Waves as a Probe of Jupiter's Deep Atmosphere", *Journal of the Atmospheric Sciences* 43, pp. 2683–2707.

Flasar, F. M. et al. (2004), "An Intense Stratospheric Jet on Jupiter", *Nature* 427, pp. 132–135.

French, R. G. and P. J. Gierasch (1974), "Waves in the Jovian Upper Atmosphere", *Journal of the Atmospheric Sciences* 31, pp. 1707–1712.

Friedson, A. J. (1994), "Gravity Waves in Titan's Atmosphere", *Icarus* 107, pp. 40–57.

Friedson, A. J. (1999), "New Observations and Modelling of a QBO-Like Oscillation in Jupiter's Stratosphere", *Icarus* 137, pp. 34–55.

Fritts, D. C. (1984), "Gravity Wave Saturation in the Middle Atmosphere: A Review of Theory and Observations", *Reviews of Geophysics and Space Physics* 22, pp. 275–308.

Fritts, D. C. and M. J. Alexander (2003), "Gravity Wave Dynamics and Effects in the Middle Atmosphere", *Reviews of Geophysics* 41, pp. 1–64.

Garaud, P. and D. N. C. Lin (2004), "On the Evolution and Stability of a Protoplanetary Disk Dust Layer", *The Astrophysical Journal* 608, pp. 1050–1075.

Gill, A. E. (1982), *Atmosphere-Ocean Dynamics*, San Diego: Academic Press.

Goldreich, P. and P. Soter (1966), "Q in the Solar System", *Icarus* 389, pp. 375–389.

Goldstein, S. (1931), "On the Stability of Superposed Streams of Fluids of Different Densities", *Proceedings of the Royal Society of London. Series A.* 132, pp. 524–548.

Gossard, E. E. (1962), "Vertical Flux of Energy into the Lower Ionosphere from Internal Gravity Waves Generated in the Troposphere", *Journal of Geophysical Research* 67, pp. 745–757.

Gossard, E. E. and W. H. Hooke (1975), *Waves in the Atmosphere*, Elsevier.

Gu, P-G. and G. I. Ogilvie (2009), "Diurnal Thermal Tides in a Non-synchronized Hot Jupiter", *Monthly Notices of the Royal Astronomical Society* 395, pp. 422–435.

Hamilton, Kevin (1996), "Comprehensive meteorological modelling of the middle atmosphere: a tutorial review", *Journal of Atmospheric and Terrestrial Physics* 58, pp. 1591–1627.

Harrington, J., R. G. French, and K. I. Matcheva (2010), "The 1998 November 14 Occultation of GSC 0622-00345 By Saturn. II. Stratospheric Thermal Profile, Power Spectrum, and Gravity Waves", *The Astrophysical Journal* 716, pp. 404–416, arXiv: `arXiv:1005.3570v1`.

Heimpel, M., J. Aurnou, and J. Wicht (2005), "Simulation of Equatorial and High-latitude Jets on Jupiter in a Deep Convection Model.", *Nature* 438, pp. 193–196.

Heng, K., K. Menou, and P. J. Phillipps (2011), "Atmospheric Circulation of Tidally Locked Exoplanets: A Suite of Benchmark Tests for Dynamical Solvers", *Monthly Notices of the Royal Astronomical Society* 413, pp. 2380–2402.

Heng, K. and S. S. Vogt (2011), "Gliese 581g as a Scaled-up Version of Earth: Atmospheric Circulation Simulations", *Monthly Notices of the Royal Astronomical Society* 415, pp. 2145–2157.

Hickey, M. P., R. L. Walterscheid, and G. Schubert (2000), "Gravity Wave Heating and Cooling in Jupiter's Thermosphere", *Icarus* 148, pp. 266–281.

Hines, C. O. (1960), "Internal Atmospheric Gravity Waves at Ionospheric Heights", *Canadian Journal of Physics* 38, pp. 1441–1481.

Holton, J. R. (1982), "The Role of Gravity Wave Induced Drag and Diffusion in the Momentum Budget of the Mesosphere", *Journal of the Atmospheric Sciences* 39, pp. 791–799.

Holton, J. R. (2004), *An Introduction to Dynamic Meteorology*, 4th ed., San Diego: Elsevier Academic Press, pp. i–xii,1–535.

Hubbard, W. B., A. Burrows, and J. I. Lunine (2002), "Theory of Giant Planets", *Annual Review of Astronomy and Astrophysics* 40, pp. 103–136.

Hubbard, W. B., V. Haemmerle, C. C. Porco, G. H. Rieke, and M. J. Reike (1995), "The Occultation of SAO 78505 by Jupiter", *Icarus* 113, pp. 103–109.

Ingersoll, A. P. (1990), "Atmospheric Dynamics of the Outer Planets", *Science* 248, pp. 308–315.

Ioannou, P. J. and R. S. Lindzen (1993a), "Gravitational tides in the outer planets. I - Implications of classical tidal theory.", *The Astrophysical Journal* 406, pp. 252–265.

Ioannou, P. J. and R. S. Lindzen (1993b), "Gravitational tides in the outer planets. II. Interior calculations and estimation of the tidal dissipation factor", *The Astrophysical Journal* 406, pp. 266–278.

Ioannou, P. J. and R. S. Lindzen (1994), "Gravitational tides on Jupiter. III: Atmospheric response and mean flow acceleration", *The Astrophysical Journal* 424, pp. 1005–1013.

Jablonowski, C. and D. L. Williamson (2006), "A baroclinic instability test case for atmospheric model dynamical cores", *Quarterly Journal of the Royal Meteorological Society* 132, pp. 2943–2975.

Knutson, H. A., D. Charbonneau, L. E. Allen, J. J. Fortney, E. Agol, N. B. Cowan, A. P. Showman, C. S. Cooper, and S. T. Megeath (2007), "A Map of the Day-Night Contrast of the Extrasolar Planet HD 189733b.", *Nature* 447, pp. 183–186.

Knutson, H. A., D. Charbonneau, L.E. Allen, A. Burrows, and S. T. Megeath (2008), "The 3.68.0 μm Broadband Emission Spectrum of HD 209458b: Evidence for an Atmospheric Temperature Inversion", *The Astrophysical Journal* 673, pp. 526–531.

Knutson, H. A., D. Charbonneau, A. Burrows, F. T. O'Donovan, and G. Mandushev (2009), "Detection of a Temperature Inversion in the Broadband Infrared Emission Spectrum of TrES-4", *The Astrophysical Journal* 691, pp. 866–874.

Koskinen, T. T., A. D. Aylward, C. G. A. Smith, and S. Miller (2007), "A Thermospheric Circulation Model for Extrasolar Giant Planets", *The Astrophysical Journal* 661, pp. 515–526.

Koskinen, T. T., J. Y-K. Cho, N. Achilleos, and A. D. Aylward (2010), "Ionization of Extrasolar Giant Planet Atmospheres", *The Astrophysical Journal* 722, pp. 178–187.

Langton, J. and G. Laughlin (2007), "Observational Consequences of Hydrodynamic Flows on Hot Jupiters", *The Astrophysical Journal* 657, pp. L113–L116.

Leovy, C. B., A. J. Friedson, and G. S. Orton (1991), "The Quasiquadrennial Oscillation of Jupiter's Equatorial Stratosphere", *Nature* 354, pp. 380–382.

Li, L., A. P. Ingersoll, A. R. Vasavada, A. A. Simon-Miller, A. D. Del Genio, S. P. Ewald, C. C. Porco, and R. A. West (2006), "Vertical Wind Shear on Jupiter from Cassini images", *Journal of Geophysical Research* 111, pp. 1–11.

Lindal, G. F. (1992), "The Atmosphere of Neptune: An Analysis of Radio Occultation Data Acquired with Voyager 2", *The Astronomical Journal* 103, pp. 967–982.

Lindzen, R. S. (1990), *Dynamics in Atmospheric Physics*, Cambridge: Cambridge University Press.

Lindzen, R. S. and H-L. Kuo (1969), "A Reliable Method for the Numerical Integration of a Large Class of Ordinary and partial Differential Equations", *Monthly Weather Review* 97, pp. 732–734.

Lipps, F. B. and R. S. Hemler (1982), "A Scale Analysis of Deep Moist Convection and Some Related Numerical Calculations", *Journal of the Atmospheric Sciences* 39, pp. 2192–2210.

Magalhães, J. A., A. Seiff, and R. E. Young (2002), "The Stratification of Jupiter's Troposphere at the Galileo Probe Entry Site", *Icarus* 158, pp. 410–433.

Marois, C., B. Macintosh, T. Barman, B. Zuckerman, I. Song, J. Patience, D. Lafrenière, and R. Doyon (2008), "Direct Imaging of Multiple Planets Orbiting the Star HR 8799.", *Science* 322, pp. 1348–1352.

Matcheva, K. and D. F. Strobel (1999), "Heating of Jupiter's Thermosphere by Dissipation of Gravity Waves Due to Molecular Viscosity and Heat Conduction", *Icarus* 140, pp. 328–340.

Mayor, M. and D. Queloz (1995), "A Jupiter-mass Companion to a Solar-type Star", *Nature* 378, pp. 355–359.

McLandress, C. (1998), "On the Importance of Gravity Waves in the Middle Atmosphere and their Parameterization in General Circulation Models", *Journal of Atmospheric and Solar-Terrestrial Physics* 60, pp. 1357–1383.

McLaughlin, D. B (1924), "Some Results of a Spectrographic Study of the Algol System", *The Astrophysical Journal* 60, pp. 22–31.

Nappo, C. J. (2002), *An Introduction to Atmospheric Gravity Waves*, Elsevier Academic Press.

Ogura, Y. and N. A. Phillips (1962), "Scale Analysis of Deep and Shallow Convection in the Atmosphere", *Journal of the Atmospheric Sciences* 19, pp. 173–179.

Polichtchouk, I., J. Y-K. Cho, C. Watkins, H. Th. Thrastarson, O. M. Umurhan, and M. de la Torre-Juarez (2012), "Intercomparison of General Circulation Models for Hot Extrasolar Planets", *In Preparation.*

Polvani, L. M., R. K. Scott, and S. J. Thomas (2004), "Numerically Converged Solutions of the Global Primitive Equations for Testing the Dynamical Core of Atmospheric GCMs", *Monthly Weather Review* 132, pp. 335–337.

Rauscher, E. and K. Menou (2010), "Three-Dimensional Modeling of Hot Jupiter Atmospheric Flows", *The Astrophysical Journal* 714, pp. 1334–1342.

Raynaud, E et al. (2003), "The 10 October 1999 HIP 9369 Occultation by the Northern Polar Region of Jupiter: Ingress and Egress Lightcurves Analysis", *Icarus* 162, pp. 344–361.

Raynaud, E., K. Matcheva, P. Drossart, F. Roques, and B. Sicardy (2004), "A Re-analysis of the 1971 Beta Scorpii Occultation by Jupiter: Study of Temperature Fluctuations and Detection of Wave Activity", *Icarus* 168, pp. 324–335.

Reuter, D. C. et al. (2007), "Jupiter Cloud Composition, Stratification, Convection, and Wave Motion: A View from New Horizons", *Science (New York, N.Y.)* 318, pp. 223–225.

Richter, J. H., F. Sassi, and R. R. Garcia (2010), "Toward a Physically Based Gravity Wave Source Parameterization in a General Circulation Model", *Journal of the Atmospheric Sciences* 67, pp. 136–156.

Rogers, J. H. (1995), *The Giant Planet Jupiter*, Cambridge Univeristy Press.

Rossiter, R. A. (1924), "On the Detection of an Effect of Rotation during Eclipse in the Velocity of the Brighter Component of Beta Lyrae, and on the Constancy of Velocity of this System", *The Astrophysical Journal* 60, pp. 15–21.

Scargle, J. D. (1982), "Studies in Astronomical Time Series Analysis. II. Statistical Aspects of Spectral Analysis of Unevenly Spaced Data", *The Astrophysical Journal* 263, pp. 835–853.

Scott, R. K. and L. M. Polvani (2008), "Equatorial Superrotation in Shallow Atmospheres", *Geophysical Research Letters* 35, pp. 1–5.

Seager, S., ed. (2010), *Exoplanets*, The University of Arizona Press.

Seiff, A., D. B. Kirk, T. C. D. Knight, R. E. Young, J. D. Mihalov, L. A. Young, F. S. Milos, G. Schubert, R. C. Blanchard, and D. Atkinson (1998), "Thermal Structure of Jupiter's Atmosphere Near the Edge of a 5-μm Hot Spot in the North Equatorial Belt", *Journal of Geophysical Research* 103, pp. 22857–22889.

Shapiro, R. (1970), "Smoothing, filtering, and boundary effects", *Reviews of Geophysics* 8, pp. 359–387.

Showman, A. P., C. S. Cooper, J. J. Fortney, and M. S Marley (2008), "Atmospheric Circulation of Hot Jupiters: Three-Dimensional Circulation Models of HD 209458b and HD 189733b with Simplified Forcing", *The Astrophysical Journal* 682, pp. 559–576.

Showman, A. P., J. J. Fortney, Y. Lian, M. S. Marley, R. S. Freedman, H. A. Knutson, and D. Charbonneau (2009), "Atmospheric Circulation of Hot Jupiters: Coupled Radiative-Dynamical General Circulation Model Simulations of HD 189733b and HD 209458b", *The Astrophysical Journal* 699, pp. 564–584.

Simon-Miller, A. A., B. J. Conrath, P. J. Gierasch, G. S. Orton, R. K. Achterberg, F. M. Flasar, and B. M. Fisher (2006), "Jupiter's Atmospheric Temperatures: From Voyager IRIS to Cassini CIRS", *Icarus* 180, pp. 98–112.

Simon-Miller, A. A., B. W. Poston, G. S. Orton, and B. Fisher (2007), "Wind Variations in Jupiter's Equatorial Atmosphere: A QQO Counterpart?", *Icarus* 186, pp. 192–203.

Snellen, I. A. G., R. J. de Kok, E. J. W. de Mooij, and S. Albrecht (2010), "The Orbital Motion, Absolute Mass and High-altitude Winds of Exoplanet HD 209458b", *Nature* 465, pp. 1049–1051.

Spiegel, E. A. and G. Veronis (1960), "On the Boussinesq Approximation for a Compressible Fluid.", *The Astrophysical Journal* 131, pp. 442–447.

Sutherland, Bruce R. (2010), *Internal Gravity Waves*, Cambridge: Cambridge University Press, pp. i–xvi, 1–377.

Swain, M. R et al. (2010), "A Ground-based Near-infrared Emission Spectrum of the Exoplanet HD 189733b.", *Nature* 463, pp. 637–639.

Taylor, G. I. (1931), "Effect of Variation in Density on the Stability of Superposed Streams of Fluid", *Proceedings of the Royal Society A: Mathematical, Physical and Engineering Sciences* 132, pp. 499–523.

Thompson, M. J. (2006), *An Introduction to Astrophysical Fluid Dynamics*, London: Imperial College Press.

Thrastarson, H. Th. and J. Y-K. Cho (2010), "Effects of Initial Flow on Close-in Planet Atmospheric Circulation", *The Astrophysical Journal* 716, pp. 144–153.

Thrastarson, H. Th. and J. Y-K. Cho (2011), "Relaxation Time and Dissipation Interaction in Hot Planet Atmospheric Flow Simulations", *The Astrophysical Journal* 729, pp. 117–127.

Tinetti, G. et al. (2007), "Water Vapour in the Atmosphere of a Transiting Extrasolar Planet", *Nature* 448, pp. 169–171.

Tokano, Tetsuya and Fritz M. Neubauer (2002), "Tidal Winds on Titan Caused by Saturn", *Icarus* 158, pp. 499–515.

Umurhan, O. M. and E. Heifetz (2007), "Holmboe Modes Revisited", *Physics of Fluids* 19, pp. 064102–1–064102–15.

Vallis, G. K. (2006), *Atmospheric and Oceanic Fluid Dynamics*, Cambridge University Press.

Vasavada, A. R. and A. P. Showman (2005), "Jovian Atmospheric Dynamics: An Update after Galileo and Cassini", *Reports on Progress in Physics* 68, pp. 1935–1996.

Vidal-Madjar, A., A. Lecavelier des Etangs, J. M. Désert, G. E. Ballester, R. Ferlet, G. Hébrard, and M. Mayor (2003), "An Extended Upper Atmosphere around the Extrasolar Planet HD209458b.", *Nature* 422, pp. 143–146.

Wallace, J. M. and P. V. Hobbs (2006), *Atmospheric Science: An Introductory Survey*, Elsevier Academic Press.

Wilhelmson, R. and Y. Ogura (1972), "The Pressure Perturbation and the Numerical Modeling of a Cloud", *Journal of the Atmospheric Sciences* 29, pp. 1295–1307.

Wolszczan, A. and D. A. Frail (1992), "A Planetary System around the Millisecond Pulsar PSR1257+12", *Nature* 355, pp. 145–147.

Yelle, R. V., L. A. Young, R. J. Vervack, R. Young, L. Pfister, and W. R. Sandel (1996), "Structure of Jupiter's Upper Atmosphere: Predictions for Galileo", *Journal of Geophysical Research* 101, pp. 2149–2161.

Young, L. A., R. V. Yelle, R. Young, A. Sieff, and D. B. Kirk (1997), "Gravity Waves in Jupiter's Thermosphere", *Science* 276, pp. 108–111.

Young, L. A., R. V. Yelle, R. Young, A. Seiff, and D. B. Kirk (2005), "Gravity Waves in Jupiter's Stratosphere as Measured by the Galileo ASI Experiment", *Icarus* 173, pp. 185–199.